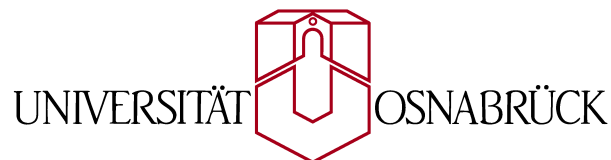

Recombination dynamics of optically generated small polarons and self-trapped excitons in lithium niobate

**Kumulative Dissertation
zur Erlangung des Grades
eines Doktors der Naturwissenschaften**

von

Simon Messerschmidt

genehmigt vom Fachbereich Physik der



Osnabrück, im Mai 2019

Erstgutachter: Prof. Dr. Mirco Imlau
Zweitgutachter: Prof. Dr. Simone Sanna

Tag der Einreichung: 14. Mai 2019

Contents

1	Introduction	5
2	Fundamentals	7
2.1	Polarons and self-trapped excitons	7
2.2	Lithium niobate	9
3	Hopping transport of small polarons in lithium niobate	11
3.1	The elusive role of Nb_{Li} bound polaron energy in hopping charge transport in $\text{Fe}:\text{LiNbO}_3$	11
3.2	Small Polaron Hopping in $\text{Fe}:\text{LiNbO}_3$ as Function of Temperature and Composition	12
4	Formation and recombination dynamics of small polarons and self-trapped excitons	13
4.1	Picosecond near-to-mid-infrared absorption of pulse-injected small polarons in magnesium doped lithium niobate	13
4.2	The role of self-trapped excitons in polaronic recombination processes in lithium niobate	14
4.3	Pulse-induced transient blue absorption related with long-lived excitonic states in iron-doped lithium niobate	15
5	Review of the absorption cross-sections of quasi-particles in lithium niobate	16
5.1	$\text{Fe}_{\text{Li}}^{2+}$ and $\text{Fe}_{\text{Li}}^{3+}$	17
5.2	$\text{Nb}_{\text{Li}}^{4+}$ bound polaron	18
5.3	$\text{O}^- - \text{V}_{\text{Li}}$ hole polaron	21
5.4	$\text{Nb}_{\text{Li}}^{4+}:\text{Nb}_{\text{Nb}}^{4+}$ bipolaron	23
5.5	Overview of the absorption cross-sections	26
6	Summary	28
	Bibliography	33
A	Publications	34
A.1	The elusive role of Nb_{Li} bound polaron energy in hopping charge transport in $\text{Fe}:\text{LiNbO}_3$	34
A.2	Small Polaron Hopping in $\text{Fe}:\text{LiNbO}_3$ as Function of Temperature and Composition	51

Contents

A.3	Picosecond near-to-mid-infrared absorption of pulse-injected small polarons in magnesium doped lithium niobate	65
A.4	The role of self-trapped excitons in polaronic recombination processes in lithium niobate	76
A.5	Pulse-induced transient blue absorption related with long-lived excitonic states in iron-doped lithium niobate	90

1 Introduction

L. D. Landau introduced his groundbreaking concept of charge carrier self-trapping in a deformable lattice already in the year 1933 [1], but to this day the topic of self-trapped excitons (STEs) and polarons receives great attention. The reason for this is that such quasi-particles play a key role in many effects, e.g., laser-induced defect formation in bulk materials [2–4], damping of frequency conversion processes [5–8], photoconductivity/photovoltaics [9–12], photoluminescence [2, 13, 14], etc. Perovskites like lithium niobate (LiNbO_3 , LN) have been investigated in particular because of the widespread use of the material in industrial applications such as optical parametric oscillators/amplifiers, Pockels-cells, or for the production of optical waveguides [15–17]. Even though these quasi-particles have been studied in LN for a long time, there are still unexplained light-induced phenomena whose explanation has been insufficient so far. For example, this includes an unexpected blue absorption after light exposure [7], room-temperature emission after femtosecond illumination [18, 19], or the stretched-exponential decay of the light-induced absorption, i.e., the temperature and spectral dependence of the stretching factor β [20, 21].

The aim of this work is a detailed analysis and understanding of these unexplained phenomena so that the resulting knowledge can be used in the future for an optimized adaption of LN or further polar perovskites for the respective application. In a first step, this includes the investigation of how lattice defects, e.g., the $\text{Nb}_{\text{Li}}^{5+}$ antisite defect, influence the transport process of quasi-particles in LN. Although general transport process models exist, mainly developed by Holstein and Emin even for the complete temperature range [22–25], these theories have in common that they assume defect-free materials and therefore cannot directly be applied to LN. Thus, a combination of Monte Carlo simulation and light-induced absorption is utilized for the investigation of the polaron recombination process in the present work. The relaxation dynamics can be modeled as a mixture of different types of polaron hops among regular or defective lattice sites characterized by individual activation energies. Then, the changing decay dynamics with altered temperature or stoichiometry may be understood in terms of the varying abundance of the different types of hops that the polarons perform.

Based on this detailed knowledge of polaron decay dynamics in lithium niobate, it is shown in a second step that neither in the mid-infrared nor in the blue/UV spectral range all observed absorption phenomena can be described only by small polarons. By comparing luminescence resulting from intrinsic self-trapped excitons with transient absorption in a broad range of temperatures and different doped crystals, a formation and recombination model is developed which is able to describe the observed dynamics. A striking feature of the proposed model is the consideration of a self-trapped exciton

1 Introduction

formation/recombination branch in addition to the well-known polaron branch. The STE branch includes scenarios in which the STEs have the possibility of pinning at intrinsic and/or extrinsic defects leading to an extraordinarily long lifetime, visible in the transient absorption.

The extension and reinterpretation of the formation and recombination model by including STEs inevitably leads to possible misinterpretation of previously determined polaron absorption cross-sections. Therefore, in a last third step, a review of the absorption shapes and cross-sections of small polarons and STEs in lithium niobate is performed. The revision becomes necessary because earlier assumptions only relied on the polaron contribution to the transient absorption. For this purpose, a ns-pump supercontinuum-probe setup is designed and applied to lithium niobate for the first time. One striking result is the comprehensive determination of the absorption shapes and cross-sections under the same experimental conditions such as temperature and probe polarization.

The results presented in this work are not only limited to lithium niobate and its applications since the hopping transport of quasi-particles and the concept of (pinned) STEs might be fundamental processes. In particular, a thorough understanding of these processes opens up the possibility of their exploitation in various materials.

2 Fundamentals

2.1 Polarons and self-trapped excitons

In general, two types of self-trapped quasi-particles can be formed in crystals: a polaron and a self-trapped exciton (STE).

If an electronic charge carrier moves slowly through a lattice, it changes the local structure by altering the equilibrium position of the surrounding atoms [1, 24]. In the case of sufficiently strong interaction, the charge carrier forms its own potential well where it is self-trapped. The combination of the additional charge carrier together with the lattice distortion is then called *polaron*. Figure 2.1 (left) schematically depicts a separated electron and hole polaron, respectively. According to Emin [24], polarons can be classified in different groups: weak-coupling polarons and strong-coupling polarons, i.e., they differ in whether the total binding energy is smaller or larger than the lattice vibrational energy. In case of strong coupling, a polaron can be further described by its induced lattice distortion. If the lattice distortion exceeds the lattice constant, the polaron will be called *large*, otherwise *small*. Every group of polaron exhibits different typical properties during its lifetime, such as a special optical absorption shape due to optical transitions to its next neighbors, temperature-dependent mobility, or sometimes luminescence during their recombination [13, 24, 26].

Another common quasi-particle in crystals is an exciton [4, 27]. An exciton is a neutral quasi-particle since it is a pair consisting of a negative electron and a positive hole. A free exciton lowers its total energy by the mutual Coulomb attraction of its constituents. Again, an exciton can couple to the crystal lattice mainly via short-range forces which induce a redistribution of the atoms in the close vicinity (Figure 2.1 (right)) and thereby a lowered potential well for the exciton [28–30]. In this case, the exciton is called *self-trapped exciton* (STE). Common other names of the STE are *excitonic polaron* [31, 32] or *molecular polaron* [33]. During the lifetime of the STE, it exhibits several broad absorption bands which resemble the transitions of the hole and/or electron to higher states within the STE or the ionization of the STE [4, 34, 35]. Another typical feature is the broadband luminescence during the recombination of the self-trapped electron-hole pair [2, 4]. However, as discussed by Toyozawa [30], there might exist a small group of self-trapped excitons which do not show luminescence during the recombination due to a considerable large coupling to the lattice.

Since both polarons and self-trapped excitons can exhibit broadband transient absorption during their lifetime and light emission during their recombination, a clear separation between STEs and polarons solely based on their optical properties is dif-

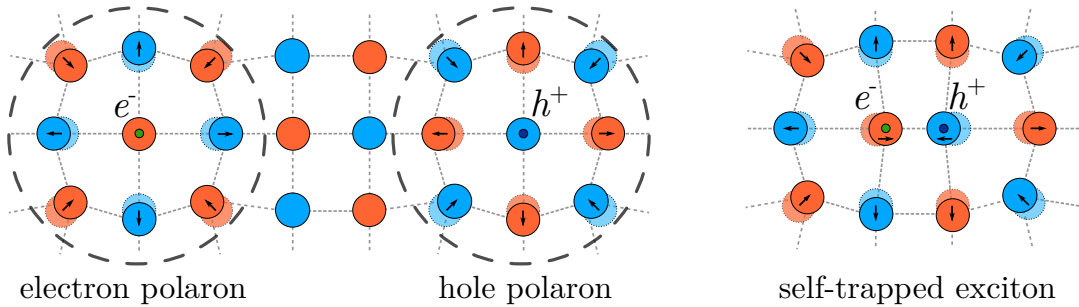


Figure 2.1 – Lattice distortions induced by charge carriers following ref. [13]. **Left:** Illustration of a small electron and hole polaron. Due to an additional charge at one atom, the neighbor atoms are shifted in their equilibrium positions and form a lattice distortion where the charge carrier is self-trapped. **Right:** Illustration of a self-trapped exciton. The electron-hole pair can form a lattice distortion and create its own potential well where it is self-trapped.

ficult. From a microscopic point of view, polarons and excitons can be distinguished from each other via the distance between the oppositely charged carriers. According to Emin [13, 24], the total energy of two oppositely charged small polarons, which consists of the Coulomb attraction and the polaron binding energy (induced lattice distortion), versus their separation reveals two minima (Figure 2.2). If both charge carriers are separated from each other, the total energy is mainly lowered by the polaron binding energy and the system forms small polarons (SP). If both charge carriers are close to each other, the total energy is lowered by the Coulomb attraction and the system forms a free exciton (FE). In addition, as explained before, the free exciton can induce a lattice distortion as well, and thereby form a self-trapped exciton (STE).

It is assumed that small polarons and STEs can move through the lattice via a hopping transport [24, 29, 36]. In general, such a hop between two neighbors consists of a three-stage process [24, 36]: (i) the lattice atoms are pushed away from their equilibrium position by phonons or tunnel effects at the position of the polaron/STE and the neighbor sites until both potentials are in coincidence, (ii) in the case of coincidence, the self-trapped charge carrier can change the lattice position, and (iii) the local lattice deformation can relax back to its equilibrium position. At high temperatures T , the hopping rate R can be assumed semiclassically and follows an Arrhenius law [24, 25]:

$$R = \nu \cdot \exp(-E_A/k_B T), \quad (2.1)$$

where k_B is the Boltzmann constant, E_A the minimum energy required to deform the lattice to a coincidence event, and ν the characteristic atomic vibrational frequency. Another option to induce a hop is the absorption of a photon. Using Holstein's one-dimensional Molecular-Crystal Model (MCM) under the assumption that the initial and final lattice site are equal [22, 23], the activation energy can be connected with the polaron binding energy $E_B \approx 2E_A$ and the maximum optical absorption $E_{\text{opt}} \approx 4E_A$.

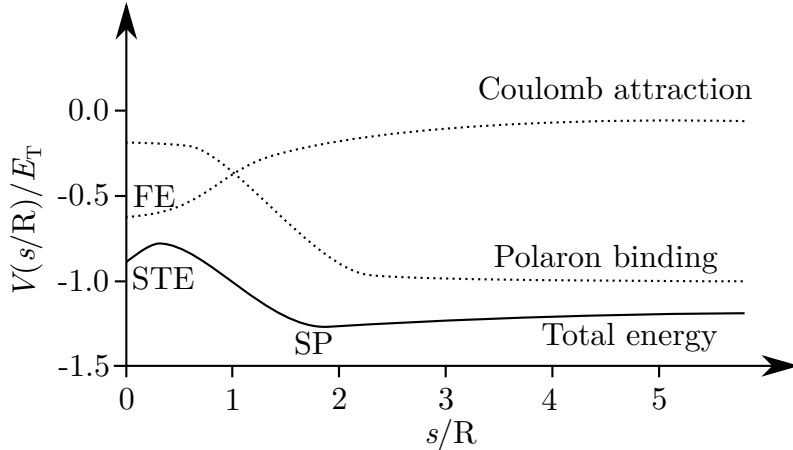


Figure 2.2 – Total energy of two oppositely charged small polarons $V(s/R)$ in units of their net binding energy E_T versus their separation s in units of the small-polaron radius R following references [13,24]. The total energy consists of the Coulomb attraction as well as the polaron binding energy and reveals two minima: the self-trapped exciton (STE) and the small polaron (SP). The minimum of the Coulomb attraction is assigned to the free exciton (FE).

2.2 Lithium niobate

All studies presented henceforth were performed in the material lithium niobate (LiNbO_3 , LN). Detailed crystallographic properties of lithium niobate can be found in the references [37, 38]. In the following, only the important points for this thesis are shortly summarized mainly based on aforementioned references.

The crystal structure can be described along the polar c -axis as a chain of oxygen octahedra forming the valence band. One third of all octahedra are filled with lithium (Li^+), one third with niobium (Nb^{5+}) forming the conduction band, and one third are empty. However, if lithium niobate is grown from a congruent melt, the ratio of $[\text{Li}]/[\text{Nb}]$ will be at about 0.94 in the crystal [38, 39]. The crystal reacts on the missing lithium with lithium vacancies (V_{Li}) and antisite-defects (Nb_{Li}). The optical absorption edge slightly depends on the stoichiometry of the crystal and is in the range of (3.8 – 4.1) eV at room temperature [40].

The optical properties of the sample can be tuned by adding different doping atoms in the melt during the growth process, e.g., Fe or Cu, to increase the photorefractive effect [38, 41]. These atoms are mainly included in the crystal on the lithium lattice position [38, 42] and can act as an electron acceptor in the oxidized state ($\text{Fe}_{\text{Li}}^{3+}/\text{Cu}_{\text{Li}}^{2+}$) and as an electron donor in the reduced state ($\text{Fe}_{\text{Li}}^{2+}/\text{Cu}_{\text{Li}}^+$) within the band gap [43, 44]. A second type of doping atoms, e.g., Mg or Zn, can be used to reduce the optical damage of the crystal. Similar to Fe and Cu, they are mainly included on lithium lattice positions but cannot act as an electron donor or acceptor within the band gap [38]. Doping with these atoms avoids the formation of Nb_{Li} antisite defects during the growth process [38, 45].

2 Fundamentals

In lithium niobate, the following four intrinsic small polarons and two types of STEs have been observed: the $\text{Nb}_{\text{Nb}}^{4+}$ free polaron, the $\text{Nb}_{\text{Li}}^{4+}$ bound polaron, the $\text{Nb}_{\text{Nb}}^{4+}:\text{Nb}_{\text{Li}}^{4+}$ bipolaron and the $\text{O}^- - \text{V}_{\text{Li}}$ hole polaron. Furthermore, electrons at extrinsic doping atoms, such as $\text{Fe}_{\text{Li}}^{2+/3+}$, can be modeled as a small polaron as well [9, 46]. An overview about the optical absorption properties, the optical generation, and decay behaviors of these polarons is given in reference [3] and references therein. A self-trapped exciton in lithium niobate is assumed to be an electron-hole pair within a NbO_6 octahedron at a regular Nb_{Nb} site or at a Nb_{Li} antisite defect. Both STEs exhibit a broad-band emission during the recombination [47–49]. However, the emission intensity and spectral maximum strongly depends on the stoichiometry of the sample (appearance of Nb_{Li} antisite defects) and the temperature [47, 50, 51].

3 Hopping transport of small polarons in lithium niobate

3.1 The elusive role of Nb_{Li} bound polaron energy in hopping charge transport in $Fe:LiNbO_3$

The author contributed to the paper *The elusive role of Nb_{Li} bound polaron energy in hopping charge transport in $Fe:LiNbO_3$* . The abstract is printed here with friendly permission of the IOP Publishing Ltd. The accepted manuscript can be found in the appendix A.1.

- Laurent Guilbert, Laura Vittadello, Marco Bazzan, Imed Mhaouech, Simon Messerschmidt, and Mirco Imlau
The elusive role of Nb_{Li} bound polaron energy in hopping charge transport in $Fe:LiNbO_3$
J. Phys.: Condens. Matter **30** (2018); doi: 10.1088/1361-648X/aaad34

Abstract: Charge transport due to small polarons hopping among defective (bound polarons) and regular (free polarons) sites is shown to depend in a non-trivial way on the value of the stabilization energy provided by the lattice distortion surrounding the charge carriers. This energy, normally not directly accessible for bound polarons using spectroscopic techniques, is determined here by a combination of experimental and numerical methods for the important case of small electron polarons bound to Nb_{Li} defects in the prototype ferroelectric oxide lithium niobate. Our findings provide an estimation of the Nb_{Li} polaron stabilization energy $E_{GP} = (0.75 \pm 0.05)$ eV and demonstrate that in lithium niobate both free and bound polarons contribute to charge transport at room temperature, explaining the fast decay of the light-induced bound polaron population observed by transient absorption spectroscopy.

3.2 Small Polaron Hopping in Fe:LiNbO₃ as Function of Temperature and Composition

The author contributed to the paper *Small Polaron Hopping in Fe:LiNbO₃ as Function of Temperature and Composition*. The abstract is printed here with friendly permission of MDPI. The complete article can be found in the appendix A.2.

- Laura Vittadello, Marco Bazzan, Simon Messerschmidt, and Mirco Imlau
Small Polaron Hopping in Fe:LiNbO₃ as Function of Temperature and Composition
Crystals **8** (2018); doi: 10.3390/cryst8070294

Abstract: Small-polaron hopping involved in charge transport in Fe-doped congruent lithium niobate is investigated as a function of temperature and composition by means of light-induced transient absorption spectroscopy. The relaxation dynamics of the light-induced polaron population is characterized by individual activation energies within different temperature ranges. A numerical investigation carried out by Monte Carlo simulations reveals that these findings may be understood in terms of the varying abundance of the different types of hops that the polarons may perform among regular or defective lattice sites. The role of the temperature and of the sample composition on the distribution of the different hop types is thus explored for a wide range of parameters, allowing one to preview the charge transport properties for a given set of experimental conditions.

4 Formation and recombination dynamics of small polarons and self-trapped excitons

4.1 Picosecond near-to-mid-infrared absorption of pulse-injected small polarons in magnesium doped lithium niobate

The author contributed to the paper *Picosecond near-to-mid-infrared absorption of pulse-injected small polarons in magnesium doped lithium niobate*. The abstract is printed here with the friendly permission of the Optical Society of America (OSA). The complete article can be found in the appendix A.3.

- Felix Freytag, Phillip Booker, Gábor Corradi, Simon Messerschmidt, Andreas Krampf, and Mirco Imlau

Picosecond near-to-mid-infrared absorption of pulse-injected small polarons in magnesium doped lithium niobate

Opt. Mater. Express **8**, 1505-1514 (2018); doi: 10.1364/OME.8.001505

Abstract: Femtosecond-pulse-induced ($E_{\text{pump}} = 2.5 \text{ eV}$) picosecond infrared absorption is studied in the spectral region between 0.30 eV and 1.05 eV in $\text{LiNbO}_3:\text{Mg}$. We find a non-instantaneous mid-infrared absorption peak in the time domain up to 1 ps and a broad-band, long-lived absorption (maximum at 0.85 eV, width $\approx 0.5 \text{ eV}$), for $t > 1 \text{ ps}$. The modelling succeeds by considering small $\text{Nb}_{\text{Nb}}^{4+}$ electron polaron formation along the sequence: (i) two-photon injection of hot electron-hole pairs at Nb-O-octahedra, (ii) dissociation and electron cooling by electron-phonon-scattering, and (iii) electron self-localization by strong electron-phonon-coupling.

4.2 The role of self-trapped excitons in polaronic recombination processes in lithium niobate

The author contributed to the paper *The role of self-trapped excitons in polaronic recombination processes in lithium niobate*. The abstract is printed here with friendly permission of the IOP Publishing Ltd. The complete article can be found in the appendix A.4.

- Simon Messerschmidt, Andreas Krampf, Felix Freytag, Mirco Imlau, Laura Vitadello, Marco Bazzan, and Gábor Corradi

The role of self-trapped excitons in polaronic recombination processes in lithium niobate

J. Phys.: Condens. Matter **31** (2019); doi: 10.1088/1361-648X/aaf4df

Abstract: Transient absorption and photoluminescence are experimentally investigated in the polaronic reference system lithium niobate, LiNbO_3 (LN), with the aim to refine the microscopic model of small polaron dynamics in materials with strong electron-phonon coupling. As a unique feature, our study is performed by using two different spectroscopic methods, in crystals with dopants enhancing photorefraction or damage resistance, and over a broad temperature range from 15 – 400 K. Although being self-consistent for particular experimental conditions, the hitherto used microscopic polaronic models reveal inconsistencies when applied to this larger data set. We show that comprehensive modeling is unlocked by the inclusion of an additional type of polaronic state with the following characteristics: (i) strongly temperature- and dopant-dependent relaxation times, (ii) an absorption feature in the blue-green spectral range, and (iii) a Kohlrausch-Williams-Watts decay shape with a temperature-dependent stretching factor $\beta(T)$ showing a behavior contrary to that of small, strong-coupling polarons. The hypothesis of self-trapped excitons (STEs, i.e., bound electron-hole pairs strongly coupled to Nb^{5+} and O^{2-} within a niobium-oxygen octahedron) and their pinning on defects as the microscopic origin of these characteristics is supported by a spectroscopic linkage of photoluminescence at low (15 K) and elevated (300 K) temperatures and explains the long-lifetime components in transient absorption as due to pinned STEs.

4.3 Pulse-induced transient blue absorption related with long-lived excitonic states in iron-doped lithium niobate

The author contributed to the paper *Pulse-induced transient blue absorption related with long-lived excitonic states in iron-doped lithium niobate*. The abstract is printed here with friendly permission of the Optical Society of America (OSA). The complete article can be found in the appendix A.5.

- Simon Messerschmidt, Bjoern Bourdon, David Brinkmann, Andreas Krampf, Laura Vittadello, and Mirco Imlau
Pulse-induced transient blue absorption related with long-lived excitonic states in iron-doped lithium niobate
Opt. Mater. Express 9, 2748-2760 (2019); doi: 10.1364/OME.9.002748

Abstract: Transient absorption is studied in Fe-doped lithium niobate single crystals with the goal to control and probe a blue absorption feature related with excitonic states bound to Fe_{Li} defect centers. The exciton absorption is deduced from the comparison of ns-pump, supercontinuum-probe spectra obtained in crystals with different Fe-concentration and $\text{Fe}_{\text{Li}}^{2+/3+}$ -ratio, at different pulse peak and photon energies as well as by signal separation taking well-known small polaron absorption bands into account. As a result, a broad-band absorption feature is deduced being characterized by an absorption cross-section of up to $\sigma^{\text{max}}(2.85 \text{ eV}) = (4 \pm 2) \cdot 10^{-22} \text{ m}^2$. The band peaks at about 2.85 eV and can be reconstructed by the sum of two Gaussians centered at 2.2 eV (width $\approx 0.5 \text{ eV}$) and 2.9 eV (width $\approx 0.4 \text{ eV}$), respectively. The appropriate build-up and decay properties strongly depend on the crystals' composition as well as the incident pulse parameters. All findings are comprehensively analyzed and discussed within the model of $\text{Fe}_{\text{Li}}^{2+} - \text{O}^- - \text{V}_{\text{Li}}$ excitonic states.

5 Review of the absorption cross-sections of quasi-particles in lithium niobate

As discussed in sections 4.2 and 4.3, the description of absorption and recombination dynamics after pulse exposure can only successfully be explained by the consideration of (pinned) STEs alongside of polarons in the recombination path. The observed absorption which is now assigned to the (pinned) STE was interpreted in previous publication as absorption features of hole or iron polarons. Therefore, it is mandatory to review the published cross-sections and shapes of the small polarons considering the findings of the previous chapters to revise the results in the literature.

All following measurements were performed with a supercontinuum-probe setup (ordinary polarization) which was described in detail in section 4.3. Steady-state spectra were obtained with a commercial two-beam spectrometer (*Shimadzu UV-3600*). For the investigation of the single polaron shapes, different thermally treated or doped lithium niobate samples and various pump wavelengths were used to trigger distinct several kinds of polarons. An overview of the used samples in this section is given in Tab. 5.1.

Table 5.1 – Congruent LN crystals used in this study. The $\text{Fe}_{\text{Li}}^{2+}$ concentration in the iron-doped samples were determined by optical absorption measurements at 532 nm [21,52]. red:LN_1 was reduced 6 hours in vacuum at 650°C. The samples were grown by: 1 MolTech GmbH, 2 University of Padova, and 3 Wigner Research Centre for Physics, Budapest.

Sample	c_{FeLi} (mol %)	$c_{\text{FeLi}^{2+}}$ (10^{17}cm^{-3})	$c_{\text{FeLi}^{2+}}/c_{\text{FeLi}^{3+}}$	producer
Fe:LN_1	0.185	10.4	0.029	1
Fe:LN_2	0.100	5.1	0.028	2
Fe:LN_3	0.020	1.0	0.027	2
Fe:LN_4	0.005	0.3	0.033	2
Fe:LN_5	0.100	≈ 0.0	≈ 0.000	2
Fe:LN_6	0.050	7.0	0.090	2
LN_1	0.000	—	—	3
red:LN_1	0.000	—	—	3

5.1 $\text{Fe}_{\text{Li}}^{2+}$ and $\text{Fe}_{\text{Li}}^{3+}$

The anchor of all further calculations is based on the paper of Kurz *et al.* [52] who investigated the connection between the concentration c of $\text{Fe}_{\text{Li}}^{2+}$ -ions and the optical absorption α_0 at 2.6 eV. The data in that paper can be used to calculate absorption cross-section $\sigma_{\text{Fe}_{\text{Li}}^{2+}}$ via

$$\sigma_{\text{Fe}_{\text{Li}}^{2+}}(2.6 \text{ eV}) = \frac{\alpha_0(2.6 \text{ eV})}{c_{\text{Fe}_{\text{Li}}^{2+}}} \approx 4.5 \cdot 10^{-22} \text{ m}^2. \quad (5.1)$$

Since the $\text{Fe}_{\text{Li}}^{2+}$ polaron is stable at room temperature, the absorption shape can be measured in a steady-state condition with a commercial spectrometer.

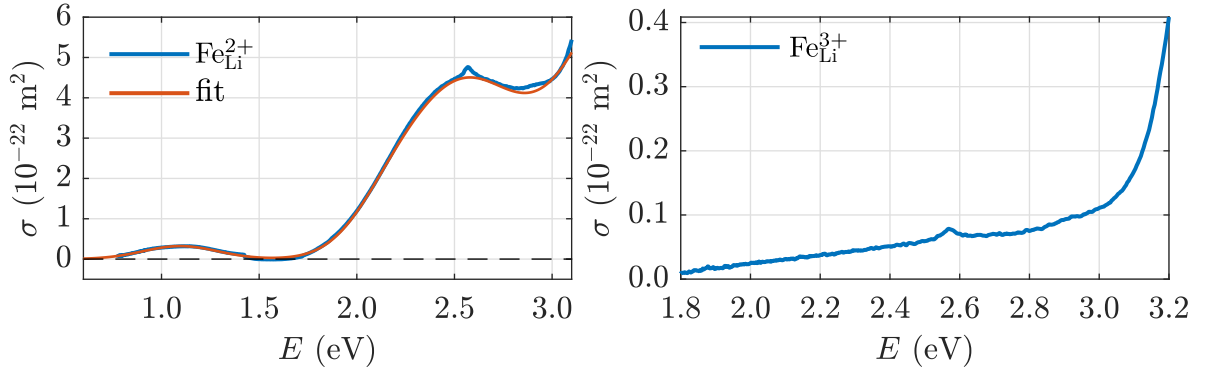


Figure 5.1 – Absorption cross-sections of $\text{Fe}_{\text{Li}}^{2+}$ and $\text{Fe}_{\text{Li}}^{3+}$. **Left:** $\sigma_{\text{Fe}_{\text{Li}}^{2+}}$ calculated from the steady-state absorption of Fe:LN_1 using $\sigma_{\text{Fe}_{\text{Li}}^{2+}}(2.6 \text{ eV}) = 4.5 \cdot 10^{-22} \text{ m}^2$ [52] (blue). Fit describing the $\text{Fe}_{\text{Li}}^{2+}$ absorption cross-section (red). The small deviations between data and fit above 2.5 eV are due to the iron F-band corresponding to spin-forbidden transitions connected with $\text{Fe}_{\text{Li}}^{3+}$ which were excluded in the fitting procedure. **Right:** $\sigma_{\text{Fe}_{\text{Li}}^{3+}}$ obtained from the steady-state absorption of sample Fe:LN_5 under the assumption that all of iron is in the valence state $\text{Fe}_{\text{Li}}^{3+}$.

Figure 5.1 (left) exemplarily shows such a steady-state absorption of the sample Fe:LN_1 scaled to match the previously reported cross-section at 2.6 eV which thereby provides the absorption cross-section of $\text{Fe}_{\text{Li}}^{2+}$ in the whole spectral range. The cross-section consists of a strong band centered at about 2.6 eV and a weak gaussian band centered at about 1.1 eV with an amplitude which is about 15 times smaller than the band in the visible spectral range.

The absorption cross-section $\sigma_{\text{Fe}_{\text{Li}}^{3+}}$ in the UV/VIS spectral range can be determined in a steady-state condition as well under the assumption that the used crystal is nearly completely oxidized, i.e., all iron-ions in the crystal are in the valence state $\text{Fe}_{\text{Li}}^{3+}$ (Fe:LN_5). Then, the cross-section can similarly be calculated from the optical absorption divided by the total concentration of iron ($\sigma_{\text{Fe}_{\text{Li}}^{3+}}(E) = \alpha_0(E)/c_{\text{Fe}_{\text{Li}}^{3+}}$) (Figure 5.1 (right)). The cross-section is at least two orders of magnitude smaller than $\sigma_{\text{Fe}_{\text{Li}}^{2+}}$ in the

visible range and has essentially no impact on the absorption. However, $\sigma_{\text{Fe}_{\text{Li}}^{3+}}$ starts to increase strongly above 3.1 eV and overlaps with the lithium niobate band edge above 3.8 eV.

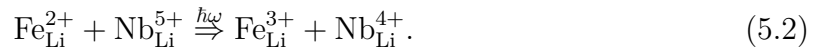
Discussion

The origin of the different absorption bands in Fe:LN is well-known and has been discussed in detail by Clark *et al.* and Dischler *et al.* [43, 44]: the visible spectral range is dominated by the $\text{Fe}_{\text{Li}}^{2+}$ D-band absorption centered at about 2.6 eV which is due to a charge transfer from $\text{Fe}_{\text{Li}}^{2+} \rightarrow \text{Nb}^{5+}$. As elaborated by Schirmer *et al.* [9, 53], the low energy tail up to the maximum can be described by the small polaron theory whereas higher energies are explained by excitations to extended states within the conduction band. The D-band is superimposed by two small absorption peaks at 2.57 eV and 2.95 eV resulting from spin-forbidden transitions within $\text{Fe}_{\text{Li}}^{3+}$ and known as F-band. A second weak absorption can be found in the NIR which is known as the iron A-band and due to an inter orbital transfer within the $\text{Fe}_{\text{Li}}^{2+}$ d-orbitals. The red curve in Figure 5.1 (left) is a phenomenological fit describing the $\text{Fe}_{\text{Li}}^{2+}$ absorption which is used for further calculations in the following sections.

In contrast to $\text{Fe}_{\text{Li}}^{2+}$, $\text{Fe}_{\text{Li}}^{3+}$ exhibits only a minor impact on the absorption in the VIS and NIR spectral range. However, there is a strong increase of the absorption starting at about 3.1 eV (Figure 5.1 (right)) which overlaps with the fundamental absorption of lithium niobate. This absorption can be assigned to the iron C-band and is due to a charge transfer from $\text{O}^{2-} \rightarrow \text{Fe}_{\text{Li}}^{3+}$. In literature, only a few information about the cross-section in the UV spectral range can be found, e.g., the C- and D-band show an isosbestic point at about 3.6 eV with a cross-section $\sigma_{\text{Fe}_{\text{Li}}^{3+}}(3.6 \text{ eV}) = \sigma_{\text{Fe}_{\text{Li}}^{2+}}(3.6 \text{ eV}) \approx 5.7 \cdot 10^{-22} \text{ m}^2$ [54]. This value is in agreement with the calculated cross-sections in this work.

5.2 $\text{Nb}_{\text{Li}}^{4+}$ bound polaron

The $\text{Nb}_{\text{Li}}^{4+}$ bound polaron (GP) is not stable at room temperature in contrast to the $\text{Fe}_{\text{Li}}^{2+}$ center and the absorption cross-section can therefore not be measured in a steady-state condition. However, as it was described in detail in section 4.3, metastable bound polarons can be formed by a one-photon absorption after pulse exposure of an iron-doped lithium niobate sample in the green spectral range:



Since it was shown before that $\text{Fe}_{\text{Li}}^{3+}$ essentially exhibits no absorption in the visible range, the change in the absorption connected with Eq. (5.2) can be written as follows:

$$\alpha_{\text{li}}(t, E, I) = \sigma_{\text{GP}}(E) \cdot \Delta c_{\text{GP}}(t, I) + \sigma_{\text{Fe}_{\text{Li}}^{2+}}(E) \cdot \Delta c_{\text{Fe}_{\text{Li}}^{2+}}(t, I). \quad (5.3)$$

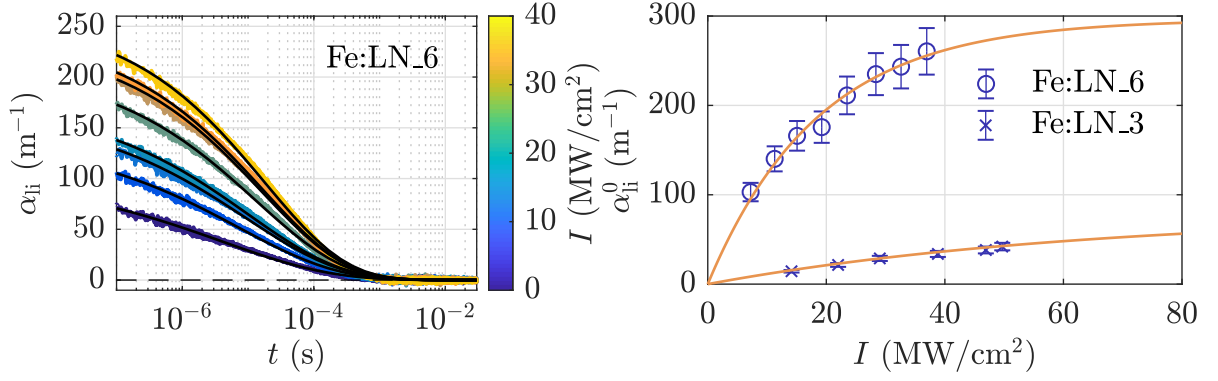


Figure 5.2 – Intensity dependence of the light-induced absorption in iron-doped lithium niobate. **Left:** Decay of the light-induced absorption at 1.58 eV (785 nm) in the sample Fe:LN_6 after exposure of a 2.33 eV (532 nm) ns-pulse for different pump intensities. The pump intensities are given by the color code. The black-lines are KWW-functions fitted to the data to estimate α_{li}^0 . **Right:** Intensity dependence of the maximum light-induced absorption α_{li}^0 measured at 1.58 eV (785 nm) for two different $\text{Fe}_{\text{Li}}^{2+}$ concentrations (Fe:LN_3 and Fe:LN_6). The orange lines are fits of Eq. (5.5) to the data. The values of $\alpha_{\text{li}}^0(1.58 \text{ eV}, I \rightarrow \infty)$ are presented in Tab. 5.2.

Here, Δc describes the change of the $\text{Fe}_{\text{Li}}^{2+}$ and $\text{Nb}_{\text{Li}}^{4+}$ concentration induced by the pump pulse, respectively. Eq. (5.3) can be rewritten under the assumption that every excited electron from $\text{Fe}_{\text{Li}}^{2+}$ forms a bound polaron ($-\Delta c_{\text{Fe}_{\text{Li}}^{2+}}(t, I) = \Delta c_{\text{GP}}(t, I)$) to

$$\sigma_{\text{GP}}(E) = -\frac{\alpha_{\text{li}}(t, E, I)}{\Delta c_{\text{Fe}_{\text{Li}}^{2+}}(t, I)} + \sigma_{\text{Fe}_{\text{Li}}^{2+}}(E). \quad (5.4)$$

Since $\sigma_{\text{Fe}_{\text{Li}}^{2+}}(E)$ is already known from section 5.1 and $\alpha_{\text{li}}(t, E, I)$ was measured before in section 4.3 (Figure 2 (left)), the only missing quantity in Eq. (5.4) is the changed concentration $\Delta c_{\text{Fe}_{\text{Li}}^{2+}}(t, I)$ produced by the pump pulse for a certain pump intensity I . However, since the total amount of $\text{Fe}_{\text{Li}}^{2+}$ is known for a given sample (Eq. (5.1)), the light-induced absorption has to be estimated under the condition that the pump pulse completely depletes the $\text{Fe}_{\text{Li}}^{2+}$ centers, i.e., determine the saturation value of the light-induced absorption. This can be done by measuring the light-induced absorption $\alpha_{\text{li}}(t, I)$ for different pump intensities and fitting KWW-functions to the decay shape (exemplarily shown in Figure 5.2 (left) for the sample Fe:LN_6). The fitting parameter $\alpha_{\text{li}}^0(E, I)$ then yields the maximum induced absorption at $t = 0$ for a certain pump intensity. If the depletion of $\text{Fe}_{\text{Li}}^{2+}$ is the only electron source for the bound polaron formation, $\alpha_{\text{li}}^0(E, I)$ should follow an exponential function [20]:

$$\alpha_{\text{li}}^0(E, I) = \alpha_{\text{li}}^0(E, I \rightarrow \infty) \cdot \left[1 - \exp\left(-\frac{I}{I_{\alpha}}\right) \right], \quad (5.5)$$

with the maximal absorption $\alpha_{\text{li}}^0(E, I \rightarrow \infty)$ where all $\text{Fe}_{\text{Li}}^{2+}$ centers are depleted, and the characteristic intensity I_{α} where the total amount of $\text{Fe}_{\text{Li}}^{2+}$ is reduced to $1/e$.

The maximum amplitudes of the light-induced absorption $\alpha_{\text{li}}^0(1.58 \text{ eV}, I)$ are shown in Figure 5.2 (right) for different pump intensities and for two samples with different $\text{Fe}_{\text{Li}}^{2+}$ concentrations. The data can be well described by Eq. (5.5), allowing extraction of the fitting parameters $\alpha_{\text{li}}^0(1.58 \text{ eV}, I \rightarrow \infty)$ as presented in Tab. 5.2 including an additional measurement from reference [20] which can be used for this calculation as well. The bound polaron absorption cross-section can then be deduced for the given measurements via Eq. (5.4) with the maximum light-induced absorption and the knowledge of the corresponding concentration. The average over all measurements is $\sigma_{\text{GP}}(1.58 \text{ eV}) \approx (6 \pm 2) \cdot 10^{-22} \text{ m}^2$.

Table 5.2 – Fit values $\alpha_{\text{li}}^0(1.58 \text{ eV}, I \rightarrow \infty)$ (cf. Figure 5.2 (right)), and absorption-cross section $\sigma_{\text{GP}}(1.58 \text{ eV})$ calculated via Eq. (5.4). Note: the values in the last row are obtained from ref. [20].

Sample	$\alpha_{\text{li}}^0(1.58 \text{ eV}, I \rightarrow \infty) \text{ (m}^{-1}\text{)}$	$\sigma_{\text{GP}}(1.58 \text{ eV}) \cdot 10^{-22} \text{ (m}^2\text{)}$
Fe:LN_3	80 ± 10	8 ± 2
Fe:LN_6	300 ± 20	4 ± 2
[20]	282	5.1

The dispersion of $\sigma_{\text{GP}}(E)$ can be obtained by applying Eq. (5.4) on a transient absorption measurement probed by a supercontinuum laser. The data from section 4.3 (Figure 2 (left)) will be used in the following. That measurement was not performed in a condition in which all $\text{Fe}_{\text{Li}}^{2+}$ ions were depleted. However, since the absorption cross-section of the bound polaron is now known at 1.58 eV, one can calculate for every pump intensity I and decay time t the changed concentration $\Delta c_{\text{Fe}_{\text{Li}}^{2+}}(t, I)$ from α_{li} . Then, the obtained concentration is used to calculate $\sigma_{\text{GP}}(E)$ for all photon energies E via Eq. (5.4). The result is depicted in Figure 5.3. $\sigma_{\text{GP}}(E)$ has its maximum at about 1.6 eV and a gaussian shape at the near-infrared site, whereas it slowly decreases in the visible spectral range and roughly coincides between (2.5 – 3.0) eV with $\sigma_{\text{Fe}_{\text{Li}}^{2+}}(E)$.

Discussion

The decay behavior of the bound polaron in iron-doped lithium was discussed in detail in sections 3.1 and 3.2. The cross-section determined in this work at 1.58 eV as well as the maximum absorption at 1.6 eV is in agreement with previous published values within its uncertainty [53, 55, 56]. However, the absorption band decreases less in the UV/VIS than expected from a measurement performed by Sweeney *et al.* [57]. The reason for the discrepancy might be that Sweeney *et al.* measured the absorption band at 80 K and with an unpolarized probe beam. In contrast, theoretical investigations by Friedrich *et al.* [58] support the measured shape in this work. In general, the high cross-section in the UV/VIS can again be explained with transitions of the electron to higher states in the conduction band [53].

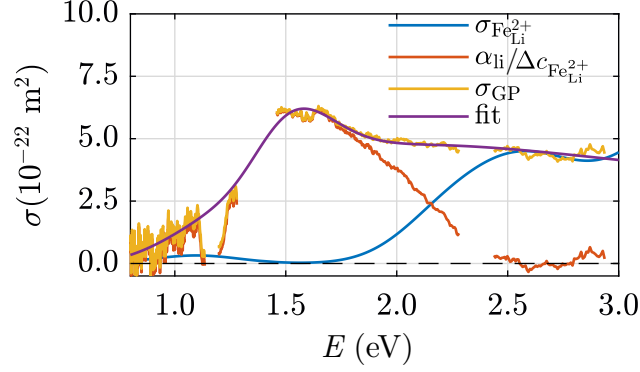


Figure 5.3 – Absorption cross-section of $\text{Fe}_{\text{Li}}^{2+}$ (blue) as it was determined in section 5.1, the measured light-induced absorption of Fe:LN_1 (section 4.3, Figure 2 (left)) divided by the induced concentration change of $\text{Fe}_{\text{Li}}^{2+}$, and the calculated shape of the bound polaron absorption cross-section σ_{GP} (yellow). The purple line is an arbitrary fit to the data describing the bound polaron cross-section.

5.3 $\text{O}^- - \text{V}_{\text{Li}}$ hole polaron

An undoped congruent lithium niobate sample (LN_1) was chosen for the determination of the $\text{O}^- - \text{V}_{\text{Li}}$ hole polaron (HP) cross-section σ_{HP} . It can be assumed that in such a sample mainly bound and hole polarons are formed after pulse exposure. Secondly, both should have the same concentration due to reasons of charge conservation, i.e., $\Delta c_{\text{GP}}(t, I) = \Delta c_{\text{HP}}(t, I)$ [3, 59]. Therefore, in analogy to the previous calculations (cf. Eqs. (5.3) and (5.4)), the hole polaron absorption cross-section may be calculated via:

$$\sigma_{\text{HP}}(E) = \frac{\alpha_{\text{li}}(t, E, I)}{\Delta c_{\text{GP}}(t, I)} - \sigma_{\text{GP}}(E). \quad (5.6)$$

Likewise, the first step focuses on the determination of the light-induced absorption $\alpha_{\text{li}}(t, E, I)$ (cf. Figure 5.4). The measurement was performed in LN_1 with a pump intensity $I = 25 \text{ MW/cm}^2$ and a photon energy $E = 3.49 \text{ eV}$ (355 nm). The pulse induces a broad absorption spectrum ranging from the visible to the near-infrared which diminishes within a few milliseconds. However, a small fraction of the induced absorption in the blue spectral range can still be observed in a time range of 0.1 s whereas the infrared absorption has completely vanished.

In a second step, the corresponding induced bound polaron concentration $\Delta c_{\text{GP}}(t, I)$ leading to the observed $\alpha_{\text{li}}(t, E, I)$ is estimated. Without any knowledge about the hole polaron absorption cross-section, in particular its dispersion, a single probe-wavelength, e.g., 785 nm, cannot be used for the calculation of the induced bound polaron concentration since it could be possible that the hole polaron coincidentally absorbs at the chosen wavelength leading to erroneous results. Instead, another approach is applied under the assumptions (i) that the formation of hole polarons only induce an absorption and does not lead to any transparency effect, i.e., $\sigma_{\text{HP}}(E)$ should be positive or zero for every photon energy E and (ii) that the hole polaron does not absorb exactly in the same spectral

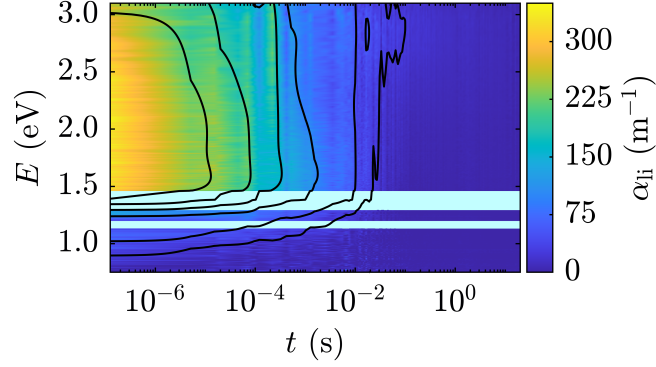


Figure 5.4 – Light-induced absorption in undoped congruent lithium niobate (LN_1) after a pump pulse at $E = 3.49$ eV (355 nm) with an intensity $I = 25$ MW/cm². The contour lines indicate steps of $\Delta\alpha_{ii} = 50$ m⁻¹.

range as the bound polaron. Then, Eq. (5.6) can be used in combination with the largest value $\Delta c_{GP}(t, I)$ for which $\sigma_{HP}(E)$ is still positive or zero. Then, the difference between the scaled light-induced absorption and the bound polaron cross-section is assigned to the hole polaron $\sigma_{HP}(E)$.

Figure 5.5 shows the result of the new ansatz. The used shape of the light-induced absorption was obtained by averaging over the first hundred microseconds in Figure 5.4. As apparent in Figure 5.5, the complete near-infrared part of α_{ii} can be described by bound polarons. In contrast, in the visible spectral range, the bound polaron absorption is not large enough to fully explain the induced absorption. According to Eq. (5.6), the difference can be ascribed to the hole polaron. The hole polaron cross-section starts at about 1.5 eV and exhibits a broad band in the visible to the ultraviolet spectral range with a maximum at about 2.1 eV and amplitude of $\sigma_{HP}(2.1 \text{ eV}) \approx 1.2 \cdot 10^{-22} \text{ m}^2$.

Discussion

The relaxation of the light-induced absorption is in agreement with previous investigations in congruent undoped lithium niobate [60]. In particular, a second long-lived blue absorption was detected in this study as well. The spectral absorption shape of this decay (not shown for brevity) reveals the same form as the $\text{Fe}_{\text{Li}}^{2+} - \text{O}^- - \text{V}_{\text{Li}}$ STE determined in section 4.3. Therefore, it is assumed that the sample contains a certain amount of iron impurities. However, as discussed before in section 4.3, the $\text{Fe}_{\text{Li}}^{2+} - \text{O}^- - \text{V}_{\text{Li}}$ STE has a formation time in the range of a few hundred microseconds such that it can be neglected from present considerations. Instead, the light-induced absorption below this time constant is assumed to be dominated by bound and hole polarons as well as the STE pinned at $\text{Fe}_{\text{Li}}^{3+}$. In general, though, the determined absorption-cross section σ_{HP} depicted in Figure 5.5 should only minor be influenced by the (pinned) STEs due to the overall low iron concentration.

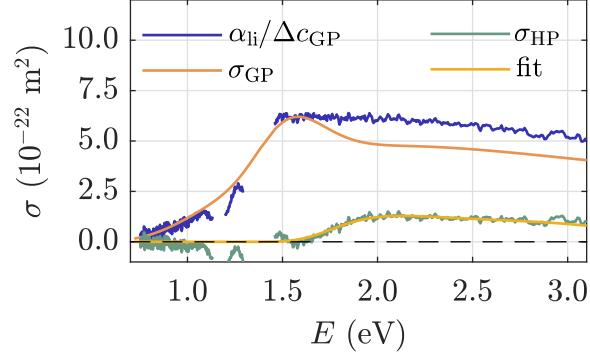


Figure 5.5 – Average over the first hundred microseconds of the light-induced absorption in Figure 5.4 (dark blue). The data are scaled in a manner that the hole polaron absorption cross-section does not become negative. Based on Eq. (5.6), the difference between scaled data and the bound polaron absorption shape (orange) is ascribed to the $O^- - V_{Li}$ hole polaron (green). An arbitrary fit describing the hole polaron cross-section σ_{HP} is chosen in yellow.

The amplitude of the cross-section σ_{HP} at 488 nm was determined for the first time by Merschjann *et al.* [55] in a congruent as well as a Mg-doped sample. However, the authors found a discrepancy of a factor four between the cross-sections of both samples which could not satisfactorily be explained. Though, the estimated value of the congruent sample is in agreement with the presented cross-section in Figure 5.5 deduced from an undoped congruent sample as well. Considering the results from section 4.2, a large amount of the blue absorption in Mg-doped lithium niobate may be possible due to a pinned STE in addition to a single $O^- - V_{Li}$ hole polaron which might explain the discrepancy between doped and undoped LN.

The absorption shape of the hole polaron was estimated for the first time by Halliburton *et al.* [61]. They measured the optical absorption of a congruent sample after electron irradiation at 77 K and assigned the blue absorption centered at 2.5 eV to the hole polaron. However, Halliburton *et al.* stated that the band might be bleached during the measurement which could serve as a possible reason to the 0.4 eV shift of the absorption maximum observed in the present work. Furthermore, the results herein have been exclusively recorded upon ordinary polarization at room temperature to ensure consistency with the investigation of other polaron species.

5.4 $Nb_{Li}^{4+}:Nb_{Nb}^{4+}$ bipolaron

Bipolarons (BP) in lithium niobate can be preferably detected in reduced lithium niobate and are responsible for the dark color of the crystal [62]. A naive assumption could be that the absorption shape of the bipolaron can be measured under steady-state conditions as it was the case for iron in section 5.1. However, Koppitz *et al.* showed that the steady-state absorption at room temperature is a mixture of $Nb_{Li}^{4+}:Nb_{Nb}^{4+}$ bipolarons

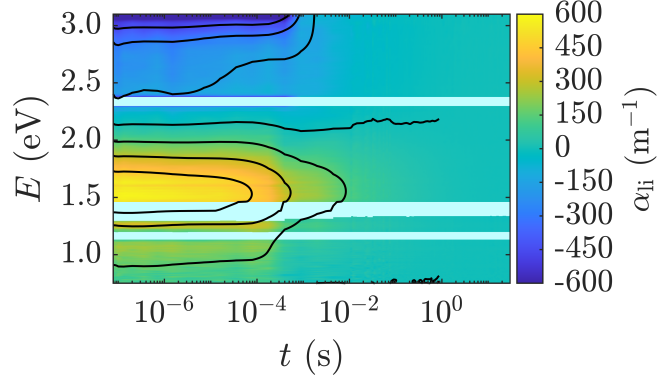


Figure 5.6 – Light-induced absorption in undoped reduced congruent lithium niobate after a pump pulse at 2.33 eV ($I = 40 \text{ MW/cm}^2$). The contour lines indicate steps of $\Delta\alpha_{\text{li}} = 150 \text{ m}^{-1}$.

and $\text{Nb}_{\text{Li}}^{4+}$ bound polarons since a portion of the bipolarons are thermally split [62]:



Therefore, the steady-state absorption cannot be used for the determination of the absorption shape.

Since it is known in literature that bipolarons can be split by light whose dynamics follow Eq. (5.7) at high intensities [60, 63], the technique of the light-induced absorption can be used again for the determination of the bipolaron absorption cross-section. The light-induced absorption $\alpha_{\text{li}}(t, E, I)$ (cf. Figure 5.6) induced by a 2.33 eV ns pump-pulse ($I = 40 \text{ MW/cm}^2$) shows a strong absorption in the red and near-infrared spectral range centered at about 1.5 eV and a width of approximately 1.0 eV. In contrast, an induced transparency in the blue/UV spectral range can be observed with increasing magnitude to higher photon energies. Both the induced transparency and the induced absorption decay with the same dynamic. Between the induced transparency and induced absorption, an isosbestic point is located at almost 2.1 eV.

In analogy to the procedure described in the sections before and in combination with Eq. (5.7), σ_{BP} can be deduced from $\alpha_{\text{li}}(t, E, I)$:

$$\sigma_{\text{BP}}(E) = 2 \cdot \left(\sigma_{\text{GP}}(E) - \frac{\alpha_{\text{li}}(t, E, I)}{\Delta c_{\text{GP}}(t, I)} \right). \quad (5.8)$$

Since the absorption shape does not change during the recombination process, one can use the average over the first few milliseconds of $\alpha_{\text{li}}(t, E, I)$ for the calculation of $\sigma_{\text{BP}}(E)$. Figure 5.7 shows the result of applying Eq. (5.8) to the data by using the largest value of $\Delta c_{\text{GP}}(t, I)$ for which $\sigma_{\text{BP}}(E)$ does not become negative. For low photon energies below 1.5 eV, the induced absorption is governed solely by bound polarons whereas a deviation manifests for higher energies. The difference between the scaled data and the two-fold polaron absorption cross-section is attributed to the bipolaron

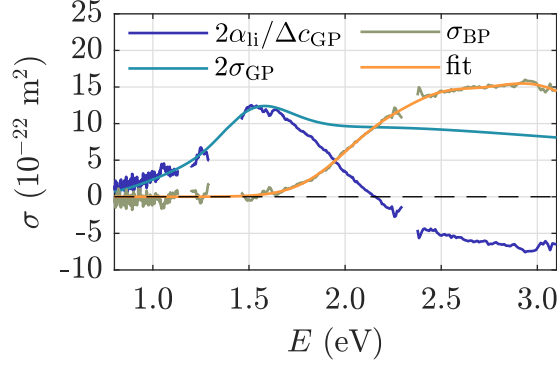


Figure 5.7 – Average over the first few milliseconds of the light-induced absorption in Figure 5.6 (blue). Absorption cross-section of the bound polaron (turquoise). The data are scaled in a manner that the bipolaron absorption cross-section does not become negative. Based on Eq. (5.8), the difference between both shapes is ascribed to the $\text{Nb}_{\text{Li}}^{4+}:\text{Nb}_{\text{Nb}}^{4+}$ bipolaron (green). Arbitrary fit describing the bipolaron cross-section σ_{BP} (orange).

cross-section $\sigma_{\text{BP}}(E)$. The estimated absorption shape of the bipolaron starts at about 1.5 eV and increases toward the green/blue spectral range. The cross-section is nearly constant above 2.5 eV and exhibits a small maximum at about 2.9 eV with an amplitude of approximately $16 \cdot 10^{-22} \text{ m}^2$.

Discussion

The discussion about bipolarons in lithium niobate raises new attention since theoretical calculations by Friedrich *et al.* [58] showed that experimentally measured absorption in reduced lithium niobate cannot be described by the $\text{Nb}_{\text{Li}}^{4+}:\text{Nb}_{\text{Nb}}^{4+}$ complex. Instead, they proposed a model in which the bipolaron might rather be formed at a $\text{Nb}_{\text{Nb}}:\text{Nb}_{\text{V}} - \text{V}_{\text{Li}}$ complex. However, the formation model of two bound polarons as measured and calculated within this section can be assumed fulfilled irregardless of the exact microscopic picture of the bipolaron. This approach might be valid since the NIR part of the light-induced absorption (Figure 5.7) can be fully described by the bound polaron absorption.

In general, the absorption and transparency dynamics are in agreement with previous investigations by Merschjann *et al.* [60]. Furthermore, the determined amplitude of the cross-section at 2.5 eV is within the uncertainty comparable to a previous study [55]. It is known from Koppitz *et al.* [62] that the steady-state absorption of a reduced lithium niobate sample consists of a mixture of bound and bipolaron absorption and that the ratio $c_{\text{GP}}/c_{\text{BP}}$ can be changed by the temperature. Therefore, it might be possible to compare the low temperature data in that paper, where nearly no bound polarons are present, with the bipolaron shape in this work. In this case, both shapes start at approximately 1.5 eV and increase toward the green spectral range. Furthermore, both isosbestic points coincide. However, the blue/UV spectral shapes deviate from each other. The bipolaron shape in this work (Figure 5.7) exhibits no clear maximum at 2.5 eV. The reason might be found in the used ordinary probe polarization in this work

in contrast to unpolarized light used by Koppitz *et al.* [62]. It is known that the polarization has a huge impact in reduced lithium niobate on the steady-state absorption above 2.5 eV [64].

5.5 Overview of the absorption cross-sections

Concludingly, the absorption cross-sections of individual quasi-particles in LN as determined in the previous sections will be presented which is summarized in Figure 5.8 (ordinary polarization and at room temperature). All quasi-particles exhibit broad asymmetric bands in the VIS and the NIR spectral range which are nearly in the same order of magnitude (10^{-22} m^2). Especially in the blue/UV spectral range, all cross-sections show significant overlap, e.g., the absorption of a bound polaron and $\text{Fe}_{\text{Li}}^{2+}$ are between 2.5 eV and 3.0 eV nearly indistinguishable.

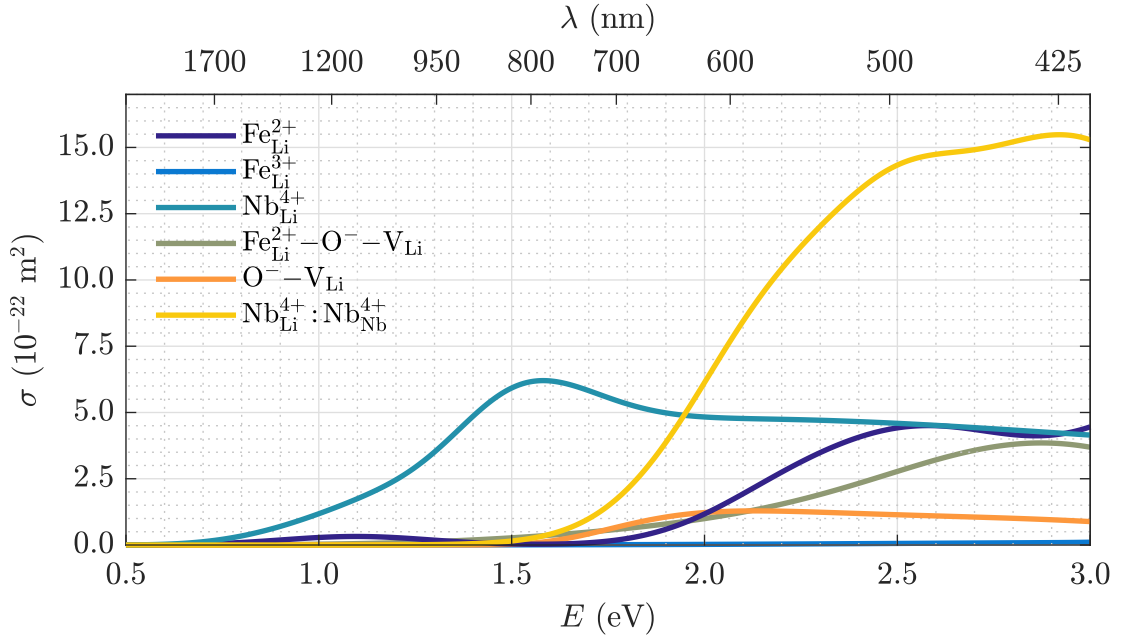


Figure 5.8 – Overview of the absorption cross-sections at room temperature for ordinary polarization of different quasi-particles in lithium niobate determined in the sections before.

Discussion

In general, the small polaron cross-sections are similar to the results in reference [55]. This is astonishing for a number of reasons: (i) previously reported data were sampled only at few selected wavelengths, (ii) STE dynamics were unknown at that time, and (iii) the estimated dispersion of the cross-sections were deduced from absorption data collected from literature measured at different experimental conditions. The advantage

of latter reason is based on the possibility to observe individual species that are normally inaccessible at room temperature, e.g., free polarons and intrinsic STEs within NbO_6 octahedra due to their fast recombination times or spectral locations of respective absorption bands. On the contrary, the comparability between these results is disturbed as absorption bands may exhibit a temperature dependency [26].

Therefore, the presented cross-sections within this work have been deduced using identical experimental parameters, i.e., (i) at room temperature, (ii) with the same probe beam polarization, and (iii) with a supercontinuum-probe laser offering a broad spectral range. Upon further detailed inspection, the cross-sections considerably differ from the presented values in reference [55], especially in the blue/UV spectral range, i.e., the additional $\text{Fe}_{\text{Li}}^{2+} - \text{O}^- - \text{V}_{\text{Li}}$ STE and the weaker hole polaron absorption. The detailed and comprehensive overview of quasi-particles in LN may be applied in a wider context, e.g., by transforming the light-induced absorption to number densities for further quantitative analysis and use of LN as a general-purpose optical material.

6 Summary

Quasi-particles formed in lithium niobate after pulse exposure were investigated by transient absorption and photoluminescence spectroscopy as well as numerical simulations. This includes the formation process, the transport through the crystal, interim pinning on defects during the relaxation process, and the final recombination with deep centers. It was shown that the charge-transport through the crystal can be described by a hopping transport including different types of hops between regular or defective lattice sites, i.e., the transport includes a mixture of free and bound small polarons. Furthermore, the different types of hops connected with varying activation energies and their distribution are responsible for an altered temporal decay curve when changing the crystal composition or temperature.

Additionally, it was shown that the hitherto accepted recombination model is insufficient to describe all transient absorption and luminescence effects in lithium niobate under certain experimental conditions, i.e., long-living absorption dynamics in the blue/UV spectral range do not follow the typical polaron dynamics and cannot be described under the assumption of charge compensation. However, similar decay characteristics between self-trapped excitons known from photoluminescence spectroscopy and the unexpected behavior of the transient absorption were found leading to a revised model. This includes, besides the known polaron relaxation and recombination branch, a significant role of self-trapped excitons and their pinning on defects (pinned STEs).

Since the consideration of further absorption centers in the relaxation path after pulse exposure might result in misinterpretations of previously determined polaron absorption cross-sections and shapes, the necessity to perform a review became apparent. Therefore, a supercontinuum pump-probe experiment was designed and all measurements applied under the same experimental conditions (temperature, polarization) so that one can extract the absorption amplitudes of the single quasi-particles in a spectral range of (0.7 – 3.0) eV. The detailed knowledge might be used to deconvolve the absorption spectra and transform them to number densities of the involved centers which enables one to obtain an easier insight into recombination and decay dynamics of small polarons and self-trapped excitons.

As the hopping transport of quasi-particles and the concept of pinned STEs might be fundamental processes, a thorough understanding opens up the possibility of their exploitation in various materials. In particular, results presented herein are not only limited to lithium niobate and its applications; an extension to a wide range of further strongly polar crystals in both their microscopic processes and their use in industry can be considered.

Bibliography

- [1] L. D. Landau. *Über Die Bewegung der Elektronen in Kristallgitter*. Phys. Z. Sowjetunion **3**, 644–645 (1933).
- [2] R. T. Williams, K. S. Song. *The self-trapped exciton*. Journal of Physics and Chemistry of Solids **51**, 679–716 (1990).
- [3] M. Imlau, H. Badorreck, C. Merschjann. *Optical nonlinearities of small polarons in lithium niobate*. Applied Physics Reviews **2**, 040606 (2015).
- [4] K. S. Song, R. T. Williams. *Self-Trapped Excitons*. Springer Series in Solid-State Sciences Springer Berlin Heidelberg (1993).
- [5] R.G. Batchko, G.D. Miller, A. Alexandrovski, M.M. Fejer, R.L. Byer. *Limitations of high-power visible wavelength periodically poled lithium niobate devices due to green-induced infrared absorption and thermal lensing*. Technical Digest. Summaries of Papers Presented at the Conference on Lasers and Electro-Optics. Conference Edition. 1998 Technical Digest Series, Vol.6 (IEEE Cat. No.98CH36178) (1998).
- [6] Y. Furukawa, K. Kitamura, A. Alexandrovski, R. K. Route, M. M. Fejer, G. Foulon. *Green-induced infrared absorption in MgO doped LiNbO₃*. Applied Physics Letters **78**, 1970–1972 (2001).
- [7] N. Waasem, A. Markosyan, M. M. Fejer, K. Buse. *Green-induced blue absorption in MgO-doped lithium niobate crystals*. Optics Letters **38**, 2953 (2013).
- [8] K. Lengyel, Á. Péter, L. Kovács, G. Corradi, L. Pálfalvi, J. Hebling, M. Unferdorben, G. Dravecz, I. Hajdara, Zs. Szaller, K. Polgár. *Growth, defect structure, and THz application of stoichiometric lithium niobate*. Applied Physics Reviews **2**, 040601 (2015).
- [9] O. F. Schirmer, M. Imlau, C. Merschjann. *Bulk photovoltaic effect of LiNbO₃:Fe and its small-polaron-based microscopic interpretation*. Physical Review B **83** (2011).
- [10] J. He, C. Franchini, J. M. Rondinelli. *Lithium Niobate-Type Oxides as Visible Light Photovoltaic Materials*. Chemistry of Materials **28**, 25–29 (2015).
- [11] N. Lu, L. Li, D. Geng, M. Liu. *A review for polaron dependent charge transport in organic semiconductor*. Organic Electronics **61**, 223–234 (2018).
- [12] O. F. Schirmer. *O⁻ bound small polarons in oxide materials*. Journal of Physics: Condensed Matter **18**, R667–R704 (2006).
- [13] D. Emin. *Dynamics of the optically induced properties of a small-polaronic glass*. Journal of Non-Crystalline Solids **35-36**, 969–973 (1980).

Bibliography

- [14] P. Reichenbach, T. Kämpfe, A. Haußmann, A. Thiessen, T. Woike, R. Steudtner, L. Kocsor, Z. Szaller, L. Kovács, L. Eng. *Polaron-Mediated Luminescence in Lithium Niobate and Lithium Tantalate and Its Domain Contrast*. Crystals **8**, 214 (2018).
- [15] J. E. Toney. *Lithium Niobate Photonics*. Artech House applied photonics series Artech House (2015).
- [16] L. Arizmendi. *Photonic applications of lithium niobate crystals*. physica status solidi (a) **201**, 253–283 (2004).
- [17] Marco Bazzan, Cinzia Sada. *Optical waveguides in lithium niobate: Recent developments and applications*. Applied Physics Reviews **2**, 040603 (2015).
- [18] P. Reichenbach, T. Kämpfe, A. Thiessen, A. Haußmann, T. Woike, L. M. Eng. *Multiphoton photoluminescence contrast in switched Mg:LiNbO₃ and Mg:LiTaO₃ single crystals*. Applied Physics Letters **105**, 122906 (2014).
- [19] P. Reichenbach, T. Kämpfe, A. Thiessen, M. Schröder, A. Haußmann, T. Woike, L. M. Eng. *Multiphoton-induced luminescence contrast between antiparallel ferroelectric domains in Mg-doped LiNbO₃*. Journal of Applied Physics **115**, 213509 (2014).
- [20] P. Herth, D. Schaniel, T. Woike, T. Granzow, M. Imlau, E. Krätzig. *Polarons generated by laser pulses in doped LiNbO₃*. Physical Review B **71** (2005).
- [21] D. Berben, K. Buse, S. Wevering, P. Herth, M. Imlau, Th. Woike. *Lifetime of small polarons in iron-doped lithium–niobate crystals*. Journal of Applied Physics **87**, 1034–1041 (2000).
- [22] T. Holstein. *Studies of Polaron Motion: Part I. The Molecular-Crystal Model*. Annals of Physics **8**, 325–342 (1959).
- [23] T. Holstein. *Studies of Polaron Motion: Part II. The "small" polaron*. Annals of Physics **8**, 343–389 (1959).
- [24] D. Emin. *Polarons*. Cambridge University Press (2012).
- [25] D. Emin. *Phonon-assisted transition rates I. Optical-phonon-assisted hopping in solids*. Advances in Physics **24**, 305–348 (1975).
- [26] D. Emin. *Optical properties of large and small polarons and bipolarons*. Physical Review B **48**, 13691–13702 (1993).
- [27] Y. Toyozawa. *Optical Processes in Solids*. Cambridge University Press (2003).
- [28] I. Pelant, J. Valenta. *Luminescence Spectroscopy of Semiconductors*. OUP Oxford (2012).
- [29] Y. Toyozawa. *Phonon structures in the spectra of solids*. Journal of Luminescence **1-2**, 732–746 (1970).
- [30] Y. Toyozawa. *Dynamics of excitons in deformable lattice*. Journal of Luminescence **24-25**, 23–30 (1981).
- [31] M. Georgiev, L. Mihailov, J. Singh. *Exciton self-trapping processes*. Pure and Applied Chemistry **67**, 447–456 (1995).

Bibliography

- [32] R. V. Yusupov, I. N. Gracheva, A. A. Rodionov, P. P. Syrnikov, A. I. Gubaev, A. Dejneka, L. Jastrabik, V. A. Trepakov, M. Kh. Salakhov. *Experimental manifestations of the $Nb^{4+}-O^-$ polaronic excitons in $KTa_{0.988}Nb_{0.012}O_3$* . Physical Review B **84** (2011).
- [33] N. F. Mott, A. M. Stoneham. *The lifetime of electrons, holes and excitons before self-trapping*. Journal of Physics C: Solid State Physics **10**, 3391–3398 (1977).
- [34] P. Li, S. Gridin, K. B. Ucer, R. T. Williams, P. R. Menge. *Picosecond absorption spectroscopy of self-trapped excitons and transient Ce states in $LaBr_3$ and $LaBr_3:Ce$* . Physical Review B **97** (2018).
- [35] R. T. Williams, M. N. Kabler. *Excited-state absorption spectroscopy of self-trapped excitons in alkali halides*. Physical Review B **9**, 1897–1907 (1974).
- [36] D. Emin. *Small polarons*. Physics Today **35**, 34–40 (1982).
- [37] R. S. Weis, T. K. Gaylord. *Lithium niobate: Summary of physical properties and crystal structure*. Applied Physics A Solids and Surfaces **37**, 191–203 (1985).
- [38] T. Volk, M. Wöhlecke. *Lithium Niobate: Defects, Photorefraction and Ferroelectric Switching*. Springer Series in Materials Science Springer Berlin Heidelberg (2008).
- [39] B. C. Grabmaier, F. Otto. *Growth and investigation of MgO-doped $LiNbO_3$* . Journal of Crystal Growth **79**, 682–688 (1986).
- [40] L. Kovács, G. Ruschhaupt, K. Polgár, G. Corradi, M. Wöhlecke. *Composition dependence of the ultraviolet absorption edge in lithium niobate*. Applied Physics Letters **70**, 2801–2803 (1997).
- [41] K. Peithmann, A. Wiebrock, K. Buse. *Photorefractive properties of highly-doped lithium niobate crystals in the visible and near-infrared*. Applied Physics B: Lasers and Optics **68**, 777–784 (1999).
- [42] T. Gog, P. Schotters, J. Falta, G. Materlik, M. Grodzicki. *The lattice position of Fe in Fe-doped $LiNbO_3$* . Journal of Physics: Condensed Matter **7**, 6971–6980 (1995).
- [43] M. G. Clark, F. J. DiSalvo, A. M. Glass, G. E. Peterson. *Electronic structure and optical index damage of iron-doped lithium niobate*. The Journal of Chemical Physics **59**, 6209–6219 (1973).
- [44] B. Dischler, J.R. Herrington, A. Räuber, H. Kurz. *Correlation of the photorefractive sensitivity in doped $LiNbO_3$ with chemically induced changes in the optical absorption spectra*. Solid State Communications **14**, 1233–1236 (1974).
- [45] B. C. Grabmaier, W. Wersing, W. Koestler. *Properties of undoped and MgO-doped $LiNbO_3$; correlation to the defect structure*. Journal of Crystal Growth **110**, 339–347 (1991).
- [46] A. Sanson, A. Zaltron, N. Argiolas, C. Sada, M. Bazzan, W. G. Schmidt, S. Sanna. *Polaronic deformation at the $Fe^{2+/3+}$ impurity site in $Fe:LiNbO_3$ crystals*. Physical Review B **91** (2015).

Bibliography

- [47] D. M. Krol, G. Blasse, R. C. Powell. *The influence of the Li/Nb ratio on the luminescence properties of LiNbO₃*. The Journal of Chemical Physics **73**, 163–166 (1980).
- [48] G. Blasse. *Fluorescence of Niobium-Activated Antimonates and an Empirical Criterion for the Occurrence of Luminescence*. The Journal of Chemical Physics **48**, 3108–3114 (1968).
- [49] M. Wiegel, M. H. J. Emond, E. R. Stobbe, G. Blasse. *Luminescence of alkali tantalates and niobates*. Journal of Physics and Chemistry of Solids **55**, 773–778 (1994).
- [50] F. Klose, M. Wöhlecke, S. Kapphan. *UV-excited luminescence of LiNbO₃ and LiNbO₃:Mg*. Ferroelectrics **92**, 181–187 (1989).
- [51] M. Wiegel, G. Blasse, A. Navrotsky, A. Mehta, N. Kumada, N. Kinomura. *Luminescence of the Ilmenite Phase of LiNbO₃*. Journal of Solid State Chemistry **109**, 413–415 (1994).
- [52] H. Kurz, E. Krätzig, W. Keune, H. Engelmann, U. Gonser, B. Dischler, A. Rüber. *Photorefractive centers in LiNbO₃, studied by optical-, Mössbauer- and EPR-methods*. Applied Physics **12**, 355–368 (1977).
- [53] O. F. Schirmer, M. Imlau, C. Merschjann, B. Schoke. *Electron small polarons and bipolarons in LiNbO₃*. Journal of Physics: Condensed Matter **21**, 123201 (2009).
- [54] M. V. Ciampolillo, A. Zaltron, M. Bazzan, N. Argiolas, C. Sada. *Quantification of Iron (Fe) in Lithium Niobate by Optical Absorption*. Applied Spectroscopy **65**, 216–220 (2011).
- [55] C. Merschjann, B. Schoke, D. Conradi, M. Imlau, G. Corradi, K. Polgár. *Absorption cross sections and number densities of electron and hole polarons in congruently melting LiNbO₃*. Journal of Physics: Condensed Matter **21**, 015906 (2008).
- [56] O. Beyer, D. Maxein, K. Buse, B. Sturman, H. T. Hsieh, D. Psaltis. *Investigation of nonlinear absorption processes with femtosecond light pulses in lithium niobate crystals*. Physical Review E **71** (2005).
- [57] K. L. Sweeney, L. E. Halliburton. *Oxygen vacancies in lithium niobate*. Applied Physics Letters **43**, 336–338 (1983).
- [58] M. Friedrich, W. G. Schmidt, A. Schindlmayr, S. Sanna. *Polaron optical absorption in congruent lithium niobate from time-dependent density-functional theory*. Physical Review Materials **1** (2017).
- [59] D. Conradi, C. Merschjann, B. Schoke, M. Imlau, G. Corradi, K. Polgár. *Influence of Mg doping on the behaviour of polaronic light-induced absorption in LiNbO₃*. physica status solidi (RRL) - Rapid Research Letters **2**, 284–286 (2008).
- [60] C. Merschjann, B. Schoke, M. Imlau. *Influence of chemical reduction on the particular number densities of light-induced small electron and hole polarons in nominally pure LiNbO₃*. Physical Review B **76** (2007).

Bibliography

- [61] L. E. Halliburton, K. L. Sweeney, C. Y. Chen. *Electron spin resonance and optical studies of point defects in lithium niobate*. Nuclear Instruments and Methods in Physics Research Section B: Beam Interactions with Materials and Atoms **1**, 344–347 (1984).
- [62] J. Koppitz, O. F. Schirmer, A. I. Kuznetsov. *Thermal Dissociation of Bipolarons in Reduced Undoped LiNbO₃*. Europhysics Letters (EPL) **4**, 1055–1059 (1987).
- [63] C. Merschjann, D. Berben, M. Imlau, M. Wöhlecke. *Evidence for Two-Path Recombination of Photoinduced Small Polarons in Reduced LiNbO₃*. Physical Review Letters **96** (2006).
- [64] H. Brüning. *Transiente Gitter Auf der Basis Kleiner Polaronen in Thermisch Reduziertem LiNbO₃*. Logos Verlag Berlin (2012).

A Publications

A.1 The elusive role of Nb_{Li} bound polaron energy in hopping charge transport in $Fe:LiNbO_3$

- Laurent Guilbert, Laura Vittadello, Marco Bazzan, Imed Mhaouech, Simon Messerschmidt, and Mirco Imlau
The elusive role of Nb_{Li} bound polaron energy in hopping charge transport in $Fe:LiNbO_3$
J. Phys.: Condens. Matter **30** (2018); doi: 10.1088/1361-648X/aaad34

This Accepted Manuscript is available for reuse under a CC BY-NC-ND 3.0 licence after the 12 month embargo period provided that all the terms of the licence are adhered to.

1
2
3 **The elusive role of Nb_{Li} bound polaron energy in hopping charge**
4 **transport in $\text{Fe} : \text{LiNbO}_3$**
5
6
7

8 Laurent Guilbert

9
10 *Université de Lorraine, LMOPS et CentraleSupélec,*
11 *EA 4423, 2 rue E. Belin, F-57070 Metz, France*
12

13
14 Laura Vittadello and Marco Bazzan

15 *Dipartimento di Fisica e Astronomia,*
16 *Università di Padova, via Marzolo 8, 35131, Italy*
17
18

19
20 Imed Mhaouech

21 *Université de Lorraine, LMOPS et CentraleSupélec,*
22 *EA 4423, 2 rue E. Belin, F-57070 Metz, France*
23
24

25
26 Simon Messerschmidt and Mirco Imlau

27 *School of Physics, Osnabrueck University,*
28 *Barbarastrasse 7, 49076, Osnabrueck, Germany*
29
30

31
32
33 **Abstract**
34

35 Charge transport due to small polarons hopping among defective (bound polarons) and regular
36 (free polarons) sites is shown to depend in a non-trivial way from the value of the stabilization energy
37 provided by the lattice distortion surrounding the charge carriers. This energy, normally not directly
38 accessible for bound polarons by spectroscopic techniques, is here determined by a combination of
39 experimental and numerical methods for the important case of small electron polarons bound to
40 Nb_{Li} defects in the prototype ferroelectric oxide lithium niobate. Our findings provide an estimation
41 of the Nb_{Li} polaron stabilization energy $E_{GP} = (0.75 \pm 0.05) \text{ eV}$ and point out that in lithium
42 niobate both free and bound polarons contributes to charge transport already at room temperature,
43 explaining the fast decays of the light-induced bound polaron population observed by transient
44 absorption spectroscopy.
45
46
47
48
49
50
51
52
53
54
55
56
57
58
59
60

1. INTRODUCTION

Polaron conduction plays an important role in several properties of oxide crystals, from the response to focused laser beams (optical damage and photorefractive effect) [1, 2] to the bulk photovoltaic effect and its application in ferroelectric photovoltaics [3]. In this type of transport the charge carriers are electrons or holes self-localized by a local distortion of the ionic lattice, moving by thermally activated hopping [4]. According to basic considerations [5, 6] the lattice distortion stabilizes the localized charge with an energy that is twice as large as the energy paid to distort the lattice. The net energy E obtained by the system thanks to this effect will be denoted as deformation-stabilization energy (DSE). If some charged defects are present in the lattice, the polaron can form preferentially on these sites, taking advantage of the Coulombic potential of the defect which gives an additional energy contribution of ε . This case is referred to as *bound polaron*.

The energy of a bound polaron is generally measured by the peak position of the relative absorption band, given by $M = 2E + \varepsilon$ and by its width, given by $W = (4E\hbar\omega_{LO} \ln(2))^{\frac{1}{2}}$ where $\hbar\omega_{LO}$ is the energy of the longitudinal optical (LO) phonon involved in the polaronic deformation [2]. Since this parameter is not generally known precisely, a direct estimation of E is not possible for bound polarons by spectroscopic methods alone.

On the other hand, if a material supports only one kind of polaron, its DSE appears into the average mobility as a Boltzmann-like term accounting for the effect of temperature [4, 5]:

$$\mu = \mu_0 \exp(-E/2kT)$$

However, when different hopping sites with unequal energy are present in the material, the above equation in general does not hold and it is not easy to preview what is the impact of the DSE of one specific polaronic center on the macroscopic transport properties.

Iron -doped lithium niobate (Fe:LN) is a technologically important material representing very well this situation. According to the well-accepted charge compensation model [9], the standard congruent LN structure is characterized by the replacement of 1% of lithium ions by niobiums constituting the so-called Nb_{Li} antisite defects. This defect in particular can trap a photo-excited electron forming a bound polaron ($\text{Nb}_{\text{Li}}^{4+} \equiv GP$), deeper in energy than the free polaron ($\text{Nb}_{\text{Nb}}^{4+} \equiv FP$), greatly reducing the carriers' mobility. Previously published data [2] report $M = 1.69$ eV, $E_{GP} = 0.58$ eV and $\varepsilon_{GP} = 0.53$ eV. According to these values, the electron is strongly bound to the antisite but the energy gained from the

	($\times 10^{24} \text{ m}^{-3}$)	[Fe]	[Fe ²⁺]	[Fe ³⁺]	[Fe ²⁺]/[Fe ³⁺]	[Nb _{Li}]	Initial polaron concentration
Fe:LN 0.02 mol.%		3.8	0.1	3.7	0.04	190.9	0.1
Fe:LN 0.05 mol.%		9.5	0.8	7.9	0.1	190.9	0.8
Fe:LN 0.1 mol.%		18.90	13.7	5.2	2.62	190.9	3.2

Table I: Sample defect concentrations.

local deformation of the lattice is close to the one of a free $\text{Nb}_{\text{Nb}}^{4+}$ polaron, being $E_{FP} = 0.54$ eV [2]. However, those data were obtained assuming that the frequency ω_{LO} of the vibration mode involved in the deformation around a Nb ion is the same for both the $\text{Nb}_{\text{Li}}^{4+}$ (antisite) and $\text{Nb}_{\text{Nb}}^{4+}$ (normal site) and equal to $\hbar\omega_{LO} = 0.1$ eV.

In the present work we study the role of the bound polaron DSE on the hopping transport in Fe:LN. The time decays of light-induced polaron populations in three different Fe:LN samples with different dopant concentrations and reduction degrees are measured as a function of temperature to put in evidence the role of thermally activated hopping phenomena. Particular care is devoted to the choice of the experimental conditions, so that it can be assumed that the decay occurs only towards deep Fe_{Li} traps, for which the relevant polaron parameters are known fairly well [2]. This allow us to compute the $\text{Nb}_{\text{Li}}^{4+}$ population decays in the same conditions by a Monte-Carlo (MC) simulation based on Marcus-Holstein's model [17]. The results provide an estimation of E_{GP} and of other microscopic parameters.

2. METHODS

Three Fe:CLN crystal boules are Czochralski-grown mixing together congruent LiNbO_3 (Sigma Aldrich) and Fe_2O_3 powders, with Fe contents in the melt of 0.02%, 0.05% and 0.1% mol. respectively. Being grown in congruent conditions, the expected Li/Nb ratio of the final crystals is 0.94 (neglecting compensation of intrinsic defects by Fe impurities). Parallelepipeds $4 \times 5 \times 1 \text{ mm}^3$ cut from these crystals are optically polished. The sample with the highest doping level has been chemically reduced under a mixture of $\text{Ar} - \text{H}_2$ atmosphere at 500K for several hours. The absorption coefficient at 532 nm [10] is measured for Sample #1 (Fe:LN 0.02 mol.%) and Sample #2 (Fe:LN 0.05 mol.%), while for Sample #3 (Fe:LN 0.1 mol.%) at 1128nm [11], from which the Fe^{2+} concentration is deduced. The samples compositions are given in Table I.

The polaron decays were studied by transient absorption spectroscopy (TA) using the

1
 2
 3
 4
 5
 6
 7
 8
 9
 10
 11
 12
 13
 14
 15
 16
 17
 18
 19
 20
 21
 22
 23
 24
 25
 26
 27
 28
 29
 30
 31
 32
 33
 34
 35
 36
 37
 38
 39
 40
 41
 42
 43
 44
 45
 46
 47
 48
 49
 50
 51
 52
 53
 54
 55
 56
 57
 58
 59
 60

setup described elsewhere [12, 13] based on a Q-switched, frequency doubled Nd:YAG laser at a wavelength of $\lambda = 532$ nm with a pulse duration of $\tau_{\text{FWHM}} \simeq 8$ ns and a maximum pulse energy of $E_{\text{max}} = (290 \pm 10)$ mJ. Four ordinarily polarized continuous-wave probe lasers enabled a time-resolved detection of changes in the absorption simultaneously at different wavelengths ($\lambda = 445$ nm, 488 nm, 785 nm and 633 nm or 1310 nm). The sample temperature is set by a cryostat equipped with four plane-parallel optical windows for all-optical access. The pump pulse generates an initial polaron population by excitation from Fe^{2+} donors. Due to the moderate pump pulse intensity, the photo-excitation of electrons from the valence to the conduction band by two-photon processes is disfavoured [12]. Accordingly, the presence of hole polarons is here neglected. Furthermore, by comparing the absorption coefficients with the peak photon fluence of our pump, we may consider that in Sample #1 (Fe:LN 0.02 mol.%) and in Sample #2 (Fe:LN 0.05 mol.%) all Fe^{2+} ions are likely to be ionized after the pulse, so that the initial polaron concentration can be taken to be equal to the Fe^{2+} concentration in the dark. In Sample #3 (Fe:LN 0.1 mol.%) instead, due to the high Fe^{2+} content, the absorption of the pump beam along the sample thickness cannot be neglected so that the number of photo-excited carriers becomes depth-dependent. In this case we estimated an effective initial polaron density by comparing the starting amplitude of the TA signal with that of the other samples, for which the initial polaron concentration can be assumed. The relative data are reported in Tab. I. Finally, since the polaron formation time (< 1 ps, see ref. [1]) is much shorter than our pulse duration, we can assume that the polarons position after the pulse is completely uncorrelated from the initial photogeneration site [14]. The so-produced polaron population perform a random walk hopping either among defective Nb_{Li} sites (bound polarons) or regular Nb_{Nb} sites (free polarons) until they are trapped by a Fe^{3+} ion. Both bound and free polarons contribute to the absorption at 785 nm [13]. The TA decays at this wavelength are thus calculated by summing the instantaneous bound and free polarons concentrations weighted for their respective absorption cross sections at 785 nm. Due to the incertitude in the exact cross section value and in the initial value of the absorption curve, which is quite sensitive to the experimental conditions, we allow for an arbitrary overall scale factor in matching the experimental absorption curves to the simulations.

According to the Marcus - Holstein polaron hopping model [4, 6, 7], the non-adiabatic

1
2
3 hopping frequency for a ($i \rightarrow f$) hop is:
4

$$5 \quad w_{i,f}(r, T) = \frac{1}{2} \left(\frac{\pi}{kT\lambda_{i,f}} \right)^{\frac{1}{2}} \frac{I_{i,f}^2}{\hbar} \exp \left(-\frac{r}{a_{i,f}} - \frac{U_{i,f}}{kT} \right) \quad (1)$$

6
7
8
9 In Eq. (1), r is the distance between initial and final sites and kT the absolute temperature
10 (in energy units). $\lambda_{i,f}$ is the reorganization energy of Marcus' theory corresponding to the
11 energy paid to rearrange the lattice, here equal to $(E_i + E_f)$, sum of the elastic energies of
12 the two polarons; $a_{i,f}$ is an orbital parameter describing the overlap between the electronic
13 wavefunctions at site i and f . The 1/2 factor is due to the fact that Eq. (1) expresses
14 the individual rate to a given final site, and is thus one half of the total rate in Holstein's
15 molecular chain [6]. $U_{i,f} \neq U_{f,i}$ is the hopping barrier, given by [15, 17]:
16
17
18
19
20

$$21 \quad U_{i,f} = \frac{(2E_i + \varepsilon_i - \varepsilon_f)^2}{4(E_i + E_f)} \quad (2)$$

22
23 with ε_i and ε_f the binding energies of the electron at zero deformation. When the hopping
24 is between sites of the same type ($i = f$), $U_{i,i} = E_i/2$, recovering the standard result that
25 the hopping activation energy is one half of the DSE [1, 2, 5]. The pre-exponential factor $I_{i,f}$
26 describes the intrinsic hopping rate between the two sites and is determined by the choice of
27 the (i, f) combination. Due to some considerations detailed in Appendix 1, we can restrict
28 the numbers of unknown parameters to three: the bound polaron DSE E_{GP} , the hopping
29 orbital parameter $a_{i,f} = a_{f,i} = a$ (with $i, f = FP, GP$) and the trapping orbital parameter
30 $a_{i,f} = c$ (with $i = FP$ or GP and $f = Fe$). The Nb_{Li}^{4+} population decays are computed
31 by a MC code in a 80 x 80 x 80 super-cell of the LN structure with periodic boundary
32 conditions. The three samples used in this work are described by the defect concentrations
33 listed in Table I, assuming that they are the same as in the melt. Possible errors of the
34 defect concentrations in the crystal have been taken into account in the incertitude of the
35 final results.
36
37
38
39
40
41
42
43
44
45
46
47
48
49

50 3. RESULTS AND ANALYSIS

51
52 In Figure (1) experimental results for the TA are shown at three different temperatures in
53 the three samples. The amplitude $\Delta\alpha_{TA}$ of the absorption change at 785 nm is depicted as
54 a function of time from $t = 10^{-7}$ s up to 10 s. The data have been normalized to $\Delta\alpha_{TA}(t =$
55 $10^{-7} \text{ s})$. Different simulations were performed by manually varying the values for the DSE
56 of the bound polaron E_{GP} and of the orbital lengths a and c until a satisfactory agreement
57
58
59
60

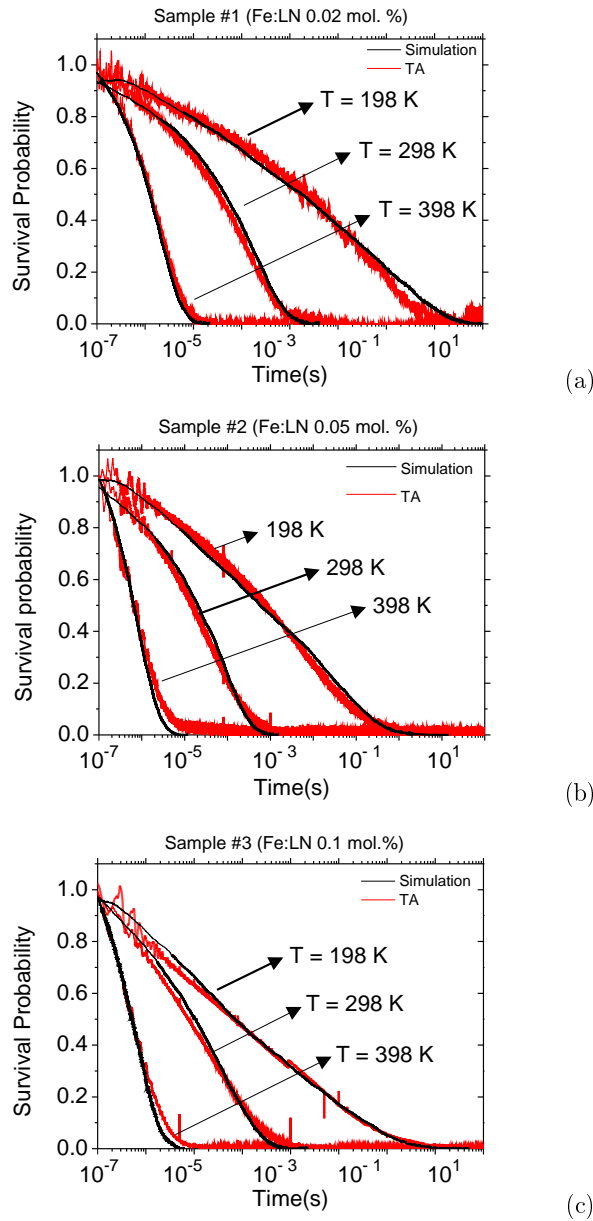


Figure 1: (Color online) Comparison between experimental results (red) and MC simulations (black) for Sample #1 (Fe:LN 0.02 mol.%, (a)), Sample #2 (Fe:LN 0.05 mol.%, (b)) and Sample #3 (Fe:LN 0.1 mol. %) for three temperatures (see Table I for sample details). The input parameters for the simulations are reported in Table II.

Sample	Description	a (Å)	c (Å)	E_{GP} (eV)
#1	Fe:LN 0.02 mol. %	1.6 ± 0.1	1.7 ± 0.1	0.75 ± 0.05
#2	Fe:LN 0.05 mol. %	1.7 ± 0.1	1.3 ± 0.1	0.75 ± 0.05
#3	Fe:LN 0.1 mol. %	1.6 ± 0.1	1.3 ± 0.1	0.75 ± 0.05

Table II: Parameters used for the simulations shown in Figure (1). For all the calculations the pre-exponential factor $I_{i,f} = I$ in Eq. (1) is taken to be equal to 0.1 eV, in accordance with Ref. [16] (see Appendix 1 for details).

between the simulations and the experimental datasets is found simultaneously for all the temperatures. The shape of the low-T curves is affected mainly by c , while high-T curves are sensitive both to a and c . The E_{GP} parameter instead rules the temperature evolution of the curves. The independent effect of the three parameters on the simulated curves allow to find a unique combination to match the experimental data. The results of this procedure for each sample are reported in Table II where the errors indicate the minimum increment considered in our trial-and error procedure. As it can be seen, all the experimental data can be reproduced fairly well by using a similar set of parameters.

It is known (see e.g. [1]) that a Kohlrausch - Williams - Watt (KWW) function of the kind $\Delta\alpha_{TA}(t) = \alpha_0 \exp[-(t/\tau_K)^\beta]$ with $0 < \beta < 1$ provides a fair description of the TA decay at 785 nm. To be more quantitative, in Table III we compare the KWW parameters obtained by fitting the experimental and the simulated decays reported in Figure (1). From those data it appears that the finer details of the decay curve shapes, embodied by the τ_K and β parameters are still beyond the accuracy of our procedure. To improve this aspect it would be necessary to minimize the difference between the experimental and numerical KWW decays by varying a , c and E_{GP} on each sample by means of a rigorous fitting procedure and/or by using more free parameters (see Appendix 1 for details) which is here practically impossible due to the high computational cost. Anyway it is clear that the global agreement between the simulated curves and the experimental data is respected over more than seven decades and for all the sample compositions, by using a coherent set of parameters. In particular the temperature dependence of the average decay time can be reproduced for all the samples only by increasing E_{GP} to 0.75 eV. It is important to note that among all the parameters entering the hopping frequency (Eq. 1), no other parameters can be used to match the temperature dependence of the experimental decay times (the other energetic parameters

	Temperature (K)	Experimental				Simulation		
		α_0 (m ⁻¹)	τ_K (μ s)	β	$\langle\tau\rangle$ (μ s)	τ_K (s)	β	$\langle\tau\rangle$ (μ s)
Sample #1 Fe:LN 0.02 mol. %	198	36 ± 2	5590 ± 60	0.20 ± 0.02	(6 ± 3) × 10 ⁵	8010 ± 68	0.202 ± 0.001	9 × 10 ⁵
	298	39 ± 2	59 ± 6	0.38 ± 0.04	227 ± 112	142 ± 14	0.561 ± 0.001	234
	398	39 ± 2	1.5 ± 0.1	0.62 ± 0.06	2.2 ± 1.1	1.81 ± 0.05	0.836 ± 0.001	2
Sample #2 Fe:LN 0.05 mol. %	198	264 ± 13	1359 ± 13	0.20 ± 0.02	(1.6 ± 0.8) × 10 ⁵	1480 ± 20	0.189 ± 0.001	2.9 × 10 ⁵
	298	249 ± 13	22 ± 2	0.34 ± 0.03	122 ± 61	56 ± 5	0.549 ± 0.001	96
	398	246 ± 13	0.63 ± 0.06	0.53 ± 0.05	1.1 ± 0.6	0.78 ± 0.01	0.820 ± 0.001	0.88
Sample #3 Fe:LN 0.1 mol. %	198	1287 ± 60	9.0 ± 1.0	0.12 ± 0.01	(7 ± 4) × 10 ⁵	51 ± 1	0.148 ± 0.001	1.6 × 10 ⁵
	298	1398 ± 70	6.7 ± 0.7	0.27 ± 0.03	104 ± 52	25 ± 2	0.446 ± 0.001	63
	398	1258 ± 60	0.40 ± 0.04	0.53 ± 0.05	0.7 ± 0.4	0.61 ± 0.01	0.828 ± 0.001	0.68

Table III: Comparison between the fitted KWW parameters of experimental and simulated curves. The error of experimental data includes both systematic and random uncertainties, the errors of numerically computed curves are obtained from standard fitting procedures and are due essentially to the deviation of simulated curves with respect to the KWW law.

being fixed to their measured value, see Tab. V below). This means that, independently on the fact that the shape of the curves could be reproduced more accurately by exploring in some finer way the parameter space, the value of the bound polaron DSE needs to be comprised in the range between 0.7 and 0.8 eV .

4. DISCUSSION

Our simulations strongly point out that a Marcus-Holstein hopping model can match experimental TA decays only if the DSE of the bound polaron is increased to $E_{GP} = 0.75$ eV. This can be understood by considering the configuration diagrams of the non-adiabatic hopping processes [2, 4, 6] from Nb_{Li} to Nb_{Li} and from Nb_{Li} to Nb_{Nb} depicted in Figure (2). According to Eq. (2), by increasing E_{GP} , the conversion barrier $U_{GP,FP}$ for the bound to free hops is decreased, while the trapping barrier $U_{FP,GP}$ from free to bound state would rise and thus reduce the efficiency of Nb_{Li} as a free polaron trap (Table IV). In other words, by increasing E_{GP} we favour the conversion from Nb_{Li} bound polarons to regular Nb_{Nb} free polarons at a given temperature. To better illustrate this finding, in Figure (3) we show as

1
2
3
4
5
6
7
8
9
10
11
12
13
14
15
16
17
18
19
20
21
22
23
24
25
26
27
28
29
30
31
32
33
34
35
36
37
38
39
40
41
42
43
44
45
46
47
48
49
50
51
52
53
54
55
56
57
58
59
60

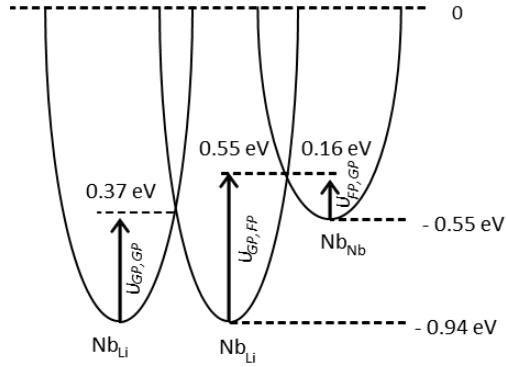


Figure 2: Configuration diagram, with energy levels deduced from $E_{GP} = 0.75$ eV and referred to the Nb $4d^1$ ground level (electron localized on a Nb orbital of the rigid crystal).

E_{GP}	$U_{GP,GP}$	$U_{FP,GP}$	$U_{FP,Fe}$	$R_{FP,GP}$	T_{conv}	Notes
	(eV)			(Å)	(K)	
0.58	0.64	0.07	0.04	13.5	670	[2]
0.75	0.55	0.16	0.04	8.6	350	This work
0.84	0.52	0.21	0.04	5.5	190	Maximum DSE compatible with optical absorption data

Table IV: Hopping barriers calculated by Eq. (2) and trapping radii calculated by Eq. (3), using the values of Table II for different values of E_{GP} . The conversion temperature T_{conv} is roughly estimated using Eq. (2.1).

an example the percentage of hops performed as a free (n_{FF}/N_{tot}) or as a bound polaron (n_{PP}/N_{tot}) for Sample #1 (Fe:LN 0.02 mol.%) using the values listed in Table II.

We can define a conversion temperature T_{conv} at which the number of $Nb_{Nb} \rightarrow Nb_{Nb}$ hops over the total is as large as the number of $Nb_{Li} \rightarrow Nb_{Li}$. In Figure (3) $T_{conv} \approx 350K$ corresponds to the point where the curves relatives to $n_{FP,FP}$ and $n_{GP,GP}$ cross each other. At room temperature, the polarons perform 5% of their hops among Nb_{Nb} sites and 22% among Nb_{Li} ones. The rest of the hops (73%) being “two - way conversions” $Nb_{Li} \leftrightarrow Nb_{Nb}$. Therefore, our data indicates that a free polaron contribution to transport is already active at 300 K, which explains why the observed TA decay time decreases so fast by increasing T . It is important to stress that T_{conv} is extremely sensitive to the E_{GP} value. If the previously reported value $E_{GP} = 0.58$ eV is assumed [2], T_{conv} is found at around 650K and no free polarons contribution should be observed at room temperature. In Appendix 2 we provide a

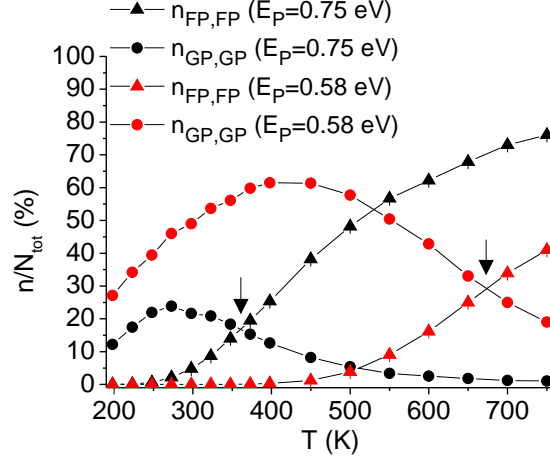


Figure 3: Percentage fraction of hops per random walk performed as free ($n_{FP,FP}$) or as bound ($n_{GP,GP}$) polaron in Sample #1 (Fe:LN 0.02 mol. %) for $E_{GP} = 0.75$ eV (black symbols) and for $E_{GP} = 0.58$ eV (red symbols). The other simulation parameters are as in Table II. The black arrows indicate the conversion temperature T_{conv} in the two cases.

criterion to estimate the temperature T_{conv} above which the free polaron transport becomes dominant.

It is instructive to visualize our results using the concept introduced in Ref. [17] of effective radius $R_{i,j}$ of a trap (j) for a polaron (i). This radius, expressing the distance below which a moving polaron is likely to be captured by a trap, is given by:

$$R_{i,j}(T) \approx a_{i,j} \left(\frac{d_i}{a_{i,i}} + \frac{U_{i,i} - U_{i,j}}{kT} - b_{i,j} \right) \quad (3)$$

with d_i the (mean) hopping length and $b_{i,j}$ a small correction. For the free polaron FP captured by an antisite GP we have $d_{FP} = 3.76$ Å and $b_{FP,GP} \sim 1.2$ Å. The value of E_{GP} reported in table II gives a trapping radius about 30% smaller than the one obtained using the energy reported in [2]. This accounts for the fact that the FP polarons can perform several hops without being trapped, already at room temperature and *a fortiori* above.

The determination of E_{GP} can be used to gain some insights on the structure of the antisite polaron. From the total bound polaron energy $M = 2E_{GP} + \varepsilon_{GP}$ known from spectroscopic data [2], we can estimate the binding energy $\varepsilon_{GP} = (0.2 \pm 0.1)$ eV (instead of 0.53 eV with $E_{GP} = 0.58$ eV). This means that the Coulomb attraction between the charge carrier and the defect is relatively weak. This appears to be reasonable if we consider that the anionic environments of both polarons are very similar (a Nb atom inside an oxygen

Parameter	Value	Unit	Ref.	Note
E_{FP}	0.545	eV	[2]	Free polaron DSE
E_{GP}	0.75 ± 0.05	eV	This work	Bound polaron DSE
E_{Fe}	0.7	eV	[2]	Fe defect DSE
ε_{FP}	0	eV		
ε_{GP}	0.2 ± 0.1	eV	This work	Bound polaron pre-localization energy
ε_{Fe}	1.22	eV	[2]	Fe defect pre-localization energy
$(\omega_{LO})_{FP}$	0.1	eV	[2]	Free polaron phonon energy
$(\omega_{LO})_{GP}$	0.077 ± 0.005	eV	This work	Bound polaron phonon energy

Table V: Refined values of the energetic parameters of small electron polarons in LN.

octahedron). We therefore can expect a similar charge density distribution and a similar Coulombic attraction for the electronic wavefunctions.

On the contrary, the cationic lattice structure of the two centers is quite different. The Nb_{Li} site “feels” the proximity of the heavy Nb_{Nb} atom, which has been uncovered as origin of the large lattice relaxation in the bipolaron state $Nb_{Li}^{4+} - Nb_{Nb}^{4+}$, as being computed by LDA calculations [18]. From the width of the Nb_{Li}^{4+} polaron optical absorption band, proportional to $(E_{GP}\hbar\omega_{LO})^{1/2}$, our new estimate for E_{GP} gives $\hbar\omega_{LO} = (77 \pm 5)$ meV. This is significantly less than the phonon energy of the NbO_6 breathing mode (109 meV, i.e. 871 cm^{-1} according to Raman data [19]). In other words, the self-trapping is favoured on Nb_{Li} versus Nb_{Nb} mainly because the surrounding lattice is softer. In Table V we report the refined values of the energetic parameters for the electron polarons in LN according to our analysis.

5. CONCLUSIONS

In conclusion, we investigated the role of the bound polaron DSE on charge transport in congruent Fe:LN by a quantitative comparison of experimental transient absorption measurements with numerical modelling based on Marcus-Holstein hopping model. The temperature dependence of the decay curves is extremely sensitive to the DSE as this parameter rules not only the hopping frequency between alike sites, but also the possibility for the polaron to hop from Nb_{Li} to regular Nb_{Nb} sites, which are characterized by a dramatically higher mobility. This fact allowed us to estimate the DSE for the Nb_{Li} bound polaron with a

1
2
3 good accuracy already from a semi-quantitative reproduction of the decay shapes, obtaining
4 $E_{GP} = (0.75 \pm 0.05) \text{ eV}$. Our results indicate that the higher total energy of the bound
5 polaron with respect to the free one is mainly due to the elastic properties of the atomic
6 surroundings of this defect, rather than to a strong electronic affinity. As an additional by-
7 product, we obtain also a first estimation of the two microscopic parameters a and c which,
8 together with E_{GP} permit to describe the polaron hopping transport of Fe:LN in a wide
9 range of temperatures and compositions using the Marcus - Holstein model. The agreement
10 between the shapes of numerical and experimental decay curves could be improved by a
11 finer exploration of the parameters' space and/or a more sophisticated modelling, which
12 is recommended for future studies. In particular, the dependence of the TA curves upon
13 the sample stoichiometry would permit to refine the values of the orbital parameters a and
14 c and of the pre-exponential factors $I_{i,f.}$. Our study was centered on Fe:LN because this
15 material offers already a rich literature on polaron transport to use as input data for our
16 simulations. We believe however that the approach and the results obtained here can be
17 extended also to other ferroelectric oxides such as perovskites for photovoltaic applications
18 or conductive polymers, for which a microscopic understanding of the material conductivity
19 would be crucial for applications.
20
21
22
23
24
25
26
27
28
29
30
31
32
33

34 Acknowledgments

35
36
37 S.M. and M.I. acknowledge Prof. O. Schirmer and A. Krampf of the University of Os-
38 nabruock for fruitful discussions. L.V. acknowledges the PhD school of Science and Engi-
39 neering of Materials and Nanostructures of the University of Padova for financial support.
40 L. V. and M. B. are grateful to the Cloud Veneto infrastructure for providing access to
41 calculus resources. All the authors are grateful to the reviewers for valuable suggestions.
42
43
44
45
46
47

48 1. MONTE CARLO SIMULATION

49
50
51 The Monte Carlo code is based on a classical Gillespie algorithm, where the lattice is
52 generated at the beginning and the hopping frequencies between neighboring sites are cal-
53 culated using eq. (1). One polaron is launched and the time that it needs to be captured
54 by a Fe^{3+} trap is computed. This procedure gives the number and type of hops performed
55 during its path. The simulation is repeated until the statistical noise is virtually eliminated.
56
57
58
59
60

1
2
3 This scheme is the same as adopted in [17], except for two differences: (i) According to the
4 photo-excitation model assumed here, we consider that a large part of the Fe^{2+} present in
5 the dark are emptied by the laser pulse. This number corresponds to the starting concen-
6 tration of polarons N_0 created by the pulse that needs to relax back to deep Fe^{3+} traps.
7 Accordingly, the concentration of Fe^{3+} traps immediately after the pulse is given by the
8 dark concentration of Fe^{3+} increased by the number of Fe^{2+} emptied by the pulse, i.e. N_0 .
9 . Likewise, this number gradually decreases to the dark concentration value (cf. Table (I))
10 during the recombination process between photo excited carriers and Fe^{3+} . We modeled this
11 effect in our simulation by decreasing the trap concentration at each iteration. (ii) When the
12 simulation is started, a given defect distribution is randomly generated inside the super-cell
13 and maintained for all the runs (instead than generating a new distribution for each run).
14 The trap saturated in the j -th iteration is deleted from the box in the $(j + 1)$ -th. In this
15 way we model the fact that, due to the random nature of the defective lattice, not all traps
16 are equivalent and those with higher probability to be visited are the first to disappear.
17

18 According to the simple polaron model described in [2, 4, 6, 7], each of the three cen-
19 ters here considered (two Nb- based polarons, Nb_{Li} and Nb_{Nb} and the $\text{Fe}^{2+/3+}$ defect) and
20 the hopping combinations between them are described by a set of parameters. Labeling
21 i the initial site and f the final site we have: (i) three energetic parameters, namely the
22 distortion-related stabilization energy E_i , the pre-localization energy ε_i and the energy of
23 the characteristic phonon mode involved in the polaron deformation $(\hbar\omega_{LO})_i$; (ii) six orbital
24 parameters $a_{i,f} = a_{f,i}$ and (iii) six pre-factors $I_{i,f} = I_{f,i}$ defining the transfer integral which
25 rules all the possible hopping processes.
26

27 Since the Nb-O octahedron structure is very similar between the Nb_{Li} antisite defect and
28 the Nb_{Nb} regular site, we consider that the transfer integrals between those sites should
29 not be very different. For the same reason, we can assume that all the transitions to and
30 from the Fe site are described by the same transfer integral. This leads to the following
31 simplifications:
32

$$33 \quad a_{FP,FP} = a_{FP,GP} = a_{GP,FP} = a_{GP,GP} = a$$

$$34 \quad a_{FP,\text{Fe}} = a_{GP,\text{Fe}} = c$$

$$35 \quad I_{FP,FP} = I_{FP,GP} = I_{GP,FP} = I_{GP,GP} = I_1$$

$$36 \quad I_{FP,\text{Fe}} = I_{GP,\text{Fe}} = I_2$$

1
2
3
4
5
6
7
8
9
10
11
12
13
14
15
16
17
18
19
20
21
22
23
24
25
26
27
28
29
30
31
32
33
34
35
36
37
38
39
40
41
42
43
44
45
46
47
48
49
50
51

Additionally, we can neglect the hopping processes from Fe towards other polarons because, due to the energies involved, those processes are much less frequent than the others. In other words, Fe is considered a “perfect” trap. Therefore the parameters $a_{\text{Fe},f}$ and $I_{\text{Fe},f}$ play no role. Finally, as the simulation results are weakly dependent on the pre-factors I_i , for sake of simplicity we can set $I_1 \approx I_2 = I$. This value can be estimated from Ref. [16] which measured the transfer integral at high temperature in Fe:LN, where the conduction is due essentially to free polarons. The data are probably not very accurate, yet, as stressed before, this parameter is not strongly affecting our results. The origin of the energies is taken on the Nb $4d^1$ ground state so that $\varepsilon_{FP} = 0$ on any Nb_{Nb} site (energetic disorder neglected). The other parameters are locked to their published values (see [2]) and are resumed in Table V.

22
23
24
25
26
27
28
29
30
31
32
33
34
35
36
37
38
39
40
41
42
43
44
45
46
47
48
49
50
51
52
53
54
55
56
57
58
59
60

In a simulated curve, the different hopping events can be considered to be ordered as a function of time. At very short timescales, we find the fastest hopping processes, typically direct trapping from a newborn Nb_{Nb}⁴⁺ polaron to a deep Fe³⁺. Subsequently there are slower processes such as the transformation of a free to a bound polaron which is then trapped by a Fe. At even longer time scales we find multi-hop processes and so on. From this view, it is clear that by relaxing some of our constraints on the symmetry of the different parameters in Eq. (1), one could improve independently any part of the decay curve. For example, by tuning independently the parameter $a_{FP,Fe}$ which is responsible for hopping events that occur typically at short time scales, one could speed up or slow down the first part of the curve, etc. In other words, a highly accurate fitting of the experimental curves with is in principle feasible. However, this would require a huge computation time and to test a number of tailored samples in order to evidence one type of hopping against one other. On the other hand, the main goal here was not to reproduce the detailed shape of the decay curves but to determine, in a reasonably simplified model, in which range must lie the investigated parameters to grant at least a semi-quantitative agreement between the Marcus- Holstein hopping model and experimental data.

52 2. CONVERSION TEMPERATURE

55
56
57
58
59
60

A theoretical expression of the so-called conversion temperature T_{conv} can be obtained by equalling the effective hopping rate and the effective conversion rate. The latter can be estimated by summing the conversion frequencies $w_{GP,FP}(r_{ij})$ for $r_{i,j} > R_{FP,GP}$ (trapping

radius of Nb_{Li} , given by Eq. (3)). Since $R_{FP,GP}$ depends itself on T , an implicit equation is obtained:

$$kT_{\text{conv}} \approx \frac{(U_{GP,FP} - U_{FP,GP}) - (U_{GP,GP} - U_{FP,FP})}{\ln(q) + (l_{\text{eff}} - d_0)/a} \quad (2.1)$$

with:

$$q = 12\pi N_0 a^3 \left(\left[\frac{R_{FP,GP}(T_{\text{conv}})}{a} \right]^2 + 2 \frac{R_{FP,GP}(T_{\text{conv}})}{a} - 2 \right) (E_{GP}/E_{FP})^{\frac{1}{2}}$$

In Eq. (2.1), l_{eff} (effective hopping length) is defined by $w_{GP,GP}(l_{\text{eff}}) = n_{GP,GP}/\tau$, with τ the mean polaron lifetime and $n_{GP,GP}$ the mean number of hops on the antisite network per random walk. From MC simulations we estimate $l_{\text{eff}} = 10 \sim 11\text{\AA}$ in our Fe:cLN samples. The corresponding results for T_{conv} are roughly given (at $\pm 5\%$) in Table IV.

-
- [1] M Imlau, H Badorreck, and C Merschjann. Optical nonlinearities of small polarons in lithium niobate. *Applied Physics Reviews*, 2(4):040606, 2015.
- [2] OF Schirmer, M Imlau, C Merschjann, and B Schoke. Electron small polarons and bipolarons in LiNbO_3 . *Journal of Physics: Condensed Matter*, 21(12):123201, 2009.
- [3] D Raiser, S Mildner, B Ifland, M Sotoudeh, P Blöchl, S Techert, and C Jooss. Evolution of hot polaron states with a nanosecond lifetime in a manganite perovskite. *Advanced Energy Materials*, 2017.
- [4] David Emin. *Polarons*. Cambridge University Press, 2013.
- [5] IG Austin and NF Mott. Polarons in crystalline and non-crystalline materials. *Advances in Physics*, 50(7):757–812, 2001.
- [6] Th Holstein. Studies of polaron motion: Part ii. the "small" polaron. *Annals of Physics*, 8(3):343–389, 1959.
- [7] RA Marcus. On the theory of oxidation-reduction reactions involving electron transfer. i. *The Journal of Chemical Physics*, 24(5):966–978, 1956.
- [8] OF Schirmer, M Imlau, and C Merschjann. Bulk photovoltaic effect of LiNbO_3 : Fe and its small-polaron-based microscopic interpretation. *Physical Review B*, 83(16):165106, 2011.
- [9] P Lerner, C Legras, and JP Dumas. Stoechiométrie des monocristaux de manganite de lithium. *Journal of Crystal Growth*, 3:231–235, 1968.

- 1
2
3
4 [10] MV Ciampolillo, A Zaltron, M Bazzan, N Argiolas, and C Sada. Quantification of iron (Fe)
5 in lithium niobate by optical absorption. *Applied Spectroscopy*, 65(2):216–220, 2011.
6
7 [11] H Kurz, E Krätzig, W Keune, H Engelmann, U Gonser, B Dischler, and A Räufer. Pho-
8 torefractive centers in LiNbO₃, studied by optical-, müessbauer-and epr-methods. *Applied*
9 *Physics A: Materials Science & Processing*, 12(4):355–368, 1977.
10
11 [12] C Merschjann, B Schoke, and M Imlau. Influence of chemical reduction on the particular
12 number densities of light-induced small electron and hole polarons in nominally pure LiNbO₃.
13 *Physical Review B*, 76(8):085114, 2007.
14
15 [13] C Merschjann, B Schoke, D Conradi, M Imlau, G Corradi, and K Polgar. Absorption cross
16 sections and number densities of electron and hole polarons in congruently melting LiNbO₃.
17 *Journal of Physics: Condensed Matter*, 21(1):015906, 2008.
18
19 [14] J Carnicero, M Carrascosa, G García, and F Agulló-López. Site correlation effects in the
20 dynamics of iron impurities Fe²⁺/ Fe³⁺ and antisite defects Nb_{Li}⁴⁺/ Nb_{Li}⁵⁺ after a short-pulse
21 excitation in LiNbO₃. *Physical Review B*, 72(24):245108, 2005.
22
23 [15] A Zylbersztejn. Thermally activated trapping in Fe-doped LiNbO₃. *Applied Physics Letters*,
24 29(12):778–780, 1976.
25
26 [16] A Dhar and A Mansingh. Optical properties of reduced lithium niobate single crystals. *Journal*
27 *of applied physics*, 68(11):5804–5809, 1990.
28
29 [17] I Mhaouech and L Guilbert. Temperature dependence of small polaron population decays in
30 iron-doped lithium niobate by monte carlo simulations. *Solid State Sciences*, 60:28–36, 2016.
31
32 [18] HH Nahm and CH Park. First-principles study of microscopic properties of the nb antisite in
33 LiNbO₃: Comparison to phenomenological polaron theory. *Physical Review B*, 78(18):184108,
34 2008.
35
36 [19] S Sanna, S Neufeld, M Rüesing, G Berth, A Zrenner, and WG Schmidt. Raman scattering
37 efficiency in LiTaO₃ and LiNbO₃ crystals. *Physical Review B*, 91(22):224302, 2015.
38
39
40
41
42
43
44
45
46
47
48
49
50
51
52
53
54
55
56
57
58
59
60

A.2 Small Polaron Hopping in Fe:LiNbO₃ as Function of Temperature and Composition

- Laura Vittadello, Marco Bazzan, Simon Messerschmidt, and Mirco Imlau
Small Polaron Hopping in Fe:LiNbO₃ as Function of Temperature and Composition
Crystals **8** (2018); doi: 10.3390/cryst8070294

©2018 by the authors. Licensee MDPI, Basel, Switzerland. This article is an open access article distributed under the terms and conditions of the Creative Commons Attribution (CC BY) license (<http://creativecommons.org/licenses/by/4.0/>).



Article

Small Polaron Hopping in Fe:LiNbO₃ as a Function of Temperature and Composition

Laura Vittadello ¹, Marco Bazzan ^{1,*} , Simon Messerschmidt ²  and Mirco Imlau ²

¹ Dipartimento di Fisica e Astronomia, Università di Padova, via Marzolo 8, 35131 Padova, Italy; laura.vittadello@uni-osnabrueck.de

² School of Physics, Osnabrueck University, Barbarastrasse 7, 49076 Osnabrueck, Germany; smesserschmi@uni-osnabrueck.de (S.M.); mirco.imlau@uni-osnabrueck.de (M.I.)

* Correspondence: marco.bazzan@unipd.it

Received: 11 June 2018; Accepted: 13 July 2018; Published: 18 July 2018



Abstract: Small-polaron hopping involved in charge transport in Fe-doped congruent lithium niobate is investigated as a function of temperature and composition by means of light-induced transient absorption spectroscopy. The relaxation dynamics of the light-induced polaron population is characterized by individual activation energies within different temperature ranges. A numerical investigation carried out by Monte Carlo simulations reveals that these findings may be understood in terms of the varying abundance of the different types of hops that the polarons may perform among regular or defective lattice sites. The role of the temperature and of the sample composition on the distribution of the different hop types is thus explored for a wide range of parameters, allowing one to preview the charge transport properties for a given set of experimental conditions.

Keywords: lithium niobate; small polarons hopping; light-induced charge transport; transient absorption; Marcus-Holstein Theory

1. Introduction

The study of small-polaron charge transport is emerging as a hot topic for the important ferroelectric crystal lithium niobate (LiNbO₃, LN). In the field of nonlinear, ultra-fast and integrated optics, it is the physical mechanism determining how photo-excited charges redistribute in the material, giving rise to internal space charge fields that affect, via the electro-optic effect, the interaction of the material with laser beams [1,2]. This is the origin of the so-called optical damage that often constitutes a major problem for laser applications. On the other hand, in photorefractive optics and holography, those mechanisms allow for low-intensity optical interaction and for recording of high fidelity optical gratings and real-time holograms [3]. In analogous materials, polaron formation and transport play a key role as well in a number of important applications such as ferroelectric photovoltaics [4–6] and in oxide catalysis [7–9].

As demonstrated in [10], by increasing the temperature and/or changing the sample composition, the conduction of LN increases by orders of magnitude, canceling out any photo-generated internal field. Analogous effects may be obtained by doping the crystal with the so-called Optical Damage-Resistant Ions (ODRIs) such as Mg, Zn or Zr. This is obviously of great importance for practical applications because it allows one to control the material response against light. However, to date, there has not been a quantitative interpretation of those phenomena in terms of polaron transport, so that it appears mandatory to check the dependence of the above-mentioned properties in this framework.

Polarons are quasiparticles made up of an electrical charge that, by the interaction with the polar crystalline environment, is able to distort the neighboring lattice, creating a local potential well. As a net result, the particle becomes self-localized. If the confinement effect is strong, the charge is concentrated on a single lattice site (small strong-coupling polaron) and moves by randomly hopping among different sites in response to lattice thermal motion. The hopping frequency of the polaron can be computed by the Marcus–Holstein theory [11–13]. In an ideal, defect-free material, the polaron mobility can be then calculated using the standard Einstein relation [14]:

$$\mu = \frac{ed^2w_0}{kT} \exp\left(-\frac{U}{kT}\right) \quad (1)$$

where e is the elementary charge, d is the characteristic hopping length (here equal to the anionic distance), kT is the thermal energy and U is the hopping barrier, which in standard polaron theory is equal to one half of the polaron energy $U = E/2$. The term $w_0 \exp\left(-\frac{U}{kT}\right)$ is thus the hopping frequency among equally-spaced identical sites. The pre-factor w_0 can be also obtained by the Marcus–Holstein theory, as will be explained in the following.

Unfortunately, in real materials, this situation is hardly realized: standard LN crystals of congruent composition contain a high density of point defects, such as the substitutional “antisite” defect $\text{Nb}_{\text{Li}}^{5+}$ or the Li vacancy V_{Li}^- , both extrinsic (dopants or impurities). Those defects constitute preferential sites for the formation of polarons, so that three types of small electron polarons are intrinsically recognized in LN [15]: the free polaron FP forming on regular $\text{Nb}_{\text{Nb}}^{5+}$ sites; the bound polaron GP forming on antisite defects $\text{Nb}_{\text{Li}}^{4+}$; the bipolaron BP, which is a combination of a free and of a bound polaron on neighboring sites $\text{Nb}_{\text{Nb}}^{4+} : \text{Nb}_{\text{Li}}^{4+}$. LN may also host O^- holes, created when energetic photons capable of band-to-band excitation are involved. In this case, hole polarons HP are formed. Finally, impurities with two valence states such as the prototypical case of $\text{Fe}_{\text{Li}}^{2+/3+}$, have the possibility to capture an electron with a potential that is a mixture of Coulomb attraction and polaronic lattice deformation. Those charged defects can be described in the polaron formalism, as well [15]. The energy barriers for hopping processes involving those sites are quite different from each other, so that there now is a set of possible activation energies instead of a single one. Moreover, the w_0 term in Equation (1) depends on the distance between the hopping sites, and if direct hopping among defective sites is considered, this may entail an anomalous diffusion regime for which Einstein’s relation is no longer valid [16]. As a consequence, the relation (1) cannot be used in real crystals. Nevertheless, in recent works [17,18], it was shown that by an appropriate choice of a few microscopic parameters, the problem can be tackled numerically by resorting to Monte Carlo simulations incorporating the presence of defects in the lattice structure of LN. In line with those studies, one may expect that depending on the temperature and composition of the crystal, one type of hop may dominate the transport process.

The aim of this work is thus to quantify the number and type of hops among the different polaronic centers upon variation of the temperature and composition. We will focus on the case of Fe doping in LN, because here, we can assume that, under the experimental conditions used, all the charges are generated by photoexcitation of Fe^{2+} centers. This allows us to neglect the presence of hole polarons (that would have been present in undoped material [19]) for which the polaronic parameters are not well known yet. At the same time, Fe^{3+} can be assumed to be the sole deep trap state. The situation herein addressed is of practical importance because it corresponds to the typical situation encountered in photorefractive experiments. The problem is attacked both experimentally and numerically. Transient absorption data are collected as a function of temperature to provide direct evidence of a change in the activation energy of the transport, hinting at the activation of different hopping processes with temperature. The situation is then explored in greater detail with the help of a dedicated simulation software based on the Monte Carlo approach.

2. Experiment

2.1. Samples

Three Fe:CLN crystal boules were Czochralski-grown at the University of Padova mixing together congruent LiNbO₃ (Sigma Aldrich, St. Louis, MO, USA) and Fe₂O₃ powders, with Fe contents in the melt of 0.02%, 0.05% and 0.1% mol, respectively. Being grown in congruent conditions, the Li/Nb ratio of the final crystals was assumed to be 0.94 (neglecting the compensation of intrinsic defects by Fe impurities). We verified that small deviations from this value and yet below the typical compositional uncertainties of the samples produced in our laboratories had no effect on the results presented in the following paragraphs. Parallelepipeds 4 × 5 × 1 mm³ cut from these crystals were optically polished. The sample with the highest doping level was chemically reduced under a mixture of Ar – H₂ atmosphere at 500 K for several hours. The absorption coefficient at 532 nm was measured for samples Fe:LN 0.02 mol % and Fe:LN 0.05 mol %, from which the Fe²⁺ concentration was obtained [20]. For sample Fe:LN 0.1 mol %, instead, due to the high absorption level, we preferred to use the datum at 1128 nm [21] from which the Fe²⁺ concentration was also deduced. The total Fe content was assumed for simplicity to be the same as in the melt, and the Fe³⁺ concentration was obtained by the difference. The samples compositions are given in Table 1.

Table 1. Defect concentrations for the samples under study determined by optical absorption (see the text).

(×10 ²⁴ m ⁻³)	[Fe]	[Fe ²⁺]	[Fe ³⁺]	[Fe ²⁺]/[Fe ³⁺]	[Nb _{Li}]
Fe:LN 0.02 mol %	3.8	0.1	3.7	0.04	190.9
Fe:LN 0.05 mol %	9.5	0.8	7.9	0.1	190.9
Fe:LN 0.1 mol %	18.90	13.7	5.2	2.62	190.9

2.2. Transient Absorption

The polaron decays were studied by light-induced Transient Absorption Spectroscopy (TAS) using the setup described elsewhere [22,23] based on a Q-switched, frequency-doubled Nd:YAG laser at a wavelength of $\lambda = 532$ nm with a pulse duration of $\tau_{FWHM} \simeq 8$ ns and a maximum pulse energy of $E_{max} = (290 \pm 10)$ mJ. The pump intensities in the various experiments were adjusted to maximize the signal to noise ratio of the experimental decay: for Fe:LN 0.02 mol %, $I \sim 60$ MW/cm²; for Fe:LN 0.05 mol %, $I \sim 200$ MW/cm²; and for Fe:LN 0.1 mol %, $I \sim 40$ MW/cm². Four ordinarily-polarized continuous-wave probe lasers enabled a time-resolved detection of changes in the absorption simultaneously at different wavelengths ($\lambda = 445$ nm, 488 nm, 785 nm and 633 nm or 1310 nm). The sample temperature was set by a cryostat equipped with four plane-parallel optical windows for all-optical access.

In Figure 1, typical TA measurements obtained on sample Fe:LN 0.1 mol % are shown at $T = 298$ K and 198 K, probing simultaneously the transient absorption at different combinations of the wavelengths: 488, 785, 1310 nm.

All the data demonstrated the previously-reported behavior [22,23]: after the pulse, a marked increase of the absorption was detected for some of the probe wavelengths, which decay to their dark value after some time, with a dynamics that depends on the probe. The signal at 785 nm was attributed mainly to bound polaron absorption, in view of the spectral dependence of the polaron cross-section, and to a minor extent, to the absorption tail of the free polaron at this wavelength. In the following, we will therefore consider that this signal is essentially proportional to the instantaneous concentration of *GP* decaying towards Fe traps, with a possible correction for the presence of free polarons. Similar considerations indicated that the signal at 1310 nm can be attributed essentially to free polarons with a contribution due to the bound polarons' absorption. The initial amplitude of the TA signal in the red/infrared correlated directly with the concentration [Fe²⁺] present in the samples

(see Table 1), suggesting that $[\text{Fe}^{2+}]$ was the main source for photoexcitation of the centers probed at 785 and 1310 nm [22]. In the following, we will restrict our attention to these probes and to free and bound polarons.

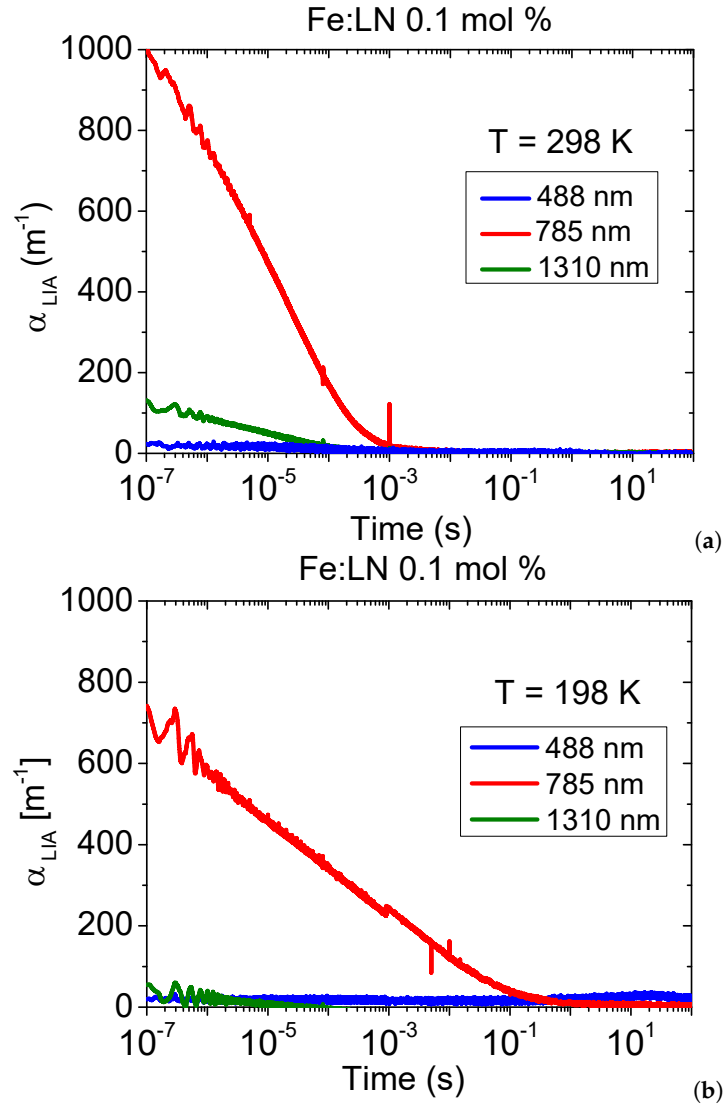


Figure 1. Typical experimental results of TA spectroscopy on the sample Fe:LN 0.1 mol %. (a) Room temperature; (b) Low temperature.

At room temperature, the absorption signals decayed to zero in the range of milliseconds, while at a low temperature, the processes were slowed down. The observed decay spectra can in general be described using an empirical stretched exponential function, named after Kohlrausch, Williams and Watts (KWW) [24,25]. This so-called KWW function is given by:

$$\alpha_{TA}(t) = \alpha_{TA}^0 \exp[-(t/\tau_K)^\beta] \quad (2)$$

where α_{TA}^0 is the absorption coefficient for $t \rightarrow 0$ (not to be confused with the signal amplitude at the beginning of the time window of our data), β is the stretching factor $0 < \beta < 1$, where $\beta = 1$ denotes the case of a mono-exponential relaxation, and τ_K is the characteristic decay time.

3. Monte Carlo Simulations

3.1. Decay Model

The pump pulse generated an initial polaron population by direct excitation from Fe^{2+} donors. Due to the moderate pump pulse intensity, the photo-excitation of electrons from the valence to the conduction band by the two-photon processes was disfavored [22], so that the presence of hole polarons was neglected here. Furthermore, by comparing the absorption coefficients with the peak photon fluence of our pump, we may consider that in samples Fe:LN 0.02 mol % and Fe:LN 0.05 mol %, all Fe^{2+} ions were likely to be ionized after the pulse so that the initial concentration of deep Fe^{3+} traps can be assumed to be equal to the total Fe concentration. In sample Fe:LN 0.1 mol %, instead, due to the high Fe^{2+} content, the absorption of the pump beam along the sample thickness cannot be neglected so that the number of photo-excited carriers became depth-dependent. To deal with this, we considered in this case an effective initial population calculated from the amplitude of the absorption signal by comparison with the other samples. Finally, since the polaron formation time (< 1 ps, see [1]) was much shorter than our pulse duration, we can assume that the polarons' position after the pulse was completely uncorrelated from the initial photogeneration site [26]. The so-produced polaron population performed a random walk hopping either among defective Nb_{Li} sites (bound polarons) or regular Nb_{Nb} sites (free polarons) until they were trapped by a Fe^{3+} ion. Both bound and free polarons contributed to the absorption at 785 nm [23].

3.2. Simulation Code

According to the Marcus–Holstein polaron hopping model [11–13], the non-adiabatic hopping frequency for a ($i \rightarrow f$) hop was:

$$w_{i,f}(r, T) = \frac{1}{2} \left(\frac{\pi}{kT\lambda_{i,f}} \right)^{\frac{1}{2}} \frac{I_{i,f}^2}{\hbar} \exp \left(-\frac{r}{a_{i,f}} - \frac{U_{i,f}}{kT} \right) \quad (3)$$

In Equation (3), r is the distance between initial and final sites and kT the absolute temperature (in energy units). $\lambda_{i,f}$ is the reorganization energy of Marcus' theory corresponding to the energy paid to rearrange the lattice, here equal to $(E_i + E_f)$, the sum of the elastic energies of the two polarons. $a_{i,f}$ is an orbital parameter describing the overlap between the electronic wavefunctions at site i and f . $U_{i,f} \neq U_{f,i}$ is the hopping barrier, given by [17,27]:

$$U_{i,f} = \frac{(2E_i + \varepsilon_i - \varepsilon_f)^2}{4(E_i + E_f)} \quad (4)$$

with ε_i and ε_f the binding energies of the electron at zero deformation. When the hopping was between sites of the same type ($i = f$), $U_{i,i} = E_i/2$, recovering the standard result that the hopping activation energy was one half of the polaron stabilization energy [1,14,15]. The pre-exponential factor $I_{i,f}$ describes the intrinsic hopping rate between the two sites and was determined by the choice of the (i, f) combination. Using the data reported in [15,18] the hopping barrier (4) for any process and the hopping rates (3) can be calculated. This result was used in a dedicated Monte Carlo code based on a classical Gillespie algorithm. The LN structure was generated at the beginning of the code with a randomly-placed set of Nb_{Li} and Fe defects, the concentration of which was set according to Table 1, assuming that they were the same as in the melt. The $\text{Nb}_{\text{Li}}^{4+}$ and $\text{Nb}_{\text{Nb}}^{4+}$ population decays were

computed by an MC code in a $80 \times 80 \times 80$ super-cell of the LN structure with periodic boundary conditions.

4. Results and Discussion

4.1. Activation Energies Deduced via TAS

According to the discussion reported elsewhere [17,18,22,23] it can be considered that $\alpha_{TA}(785 \text{ nm}, t)$ was proportional to the weighted sum of the bound and free polarons populations. Since the signal at 1310 nm remained always much smaller than the one at 785 nm and in general proportional to it, we may in a first approximation consider that the signal at 785 nm was proportional to the instantaneous bound polaron concentration and that the signal at 1310 was due essentially to the absorption tail of the bound polaron. From the measured KWW parameters, the average bound polaron lifetime can thus be computed:

$$\langle \tau \rangle = \int_0^\infty \exp \left[- \left(\frac{t}{\tau_K} \right)^\beta \right] dt = \frac{\tau_K}{\beta} \Gamma \left(\frac{1}{\beta} \right) \quad (5)$$

where $\Gamma(x)$ is the gamma Euler function. This approach has the advantage of considering both the parameters τ_K and β , allowing for a comparison between decays with different stretching exponents [28]. The result of the $\langle \tau \rangle$ calculation for the three samples is shown in Figure 2 as a function of the temperature in an Arrhenius plot. The results gave evidence of two distinct activation energies with a transition temperature around 180 K for all samples. The high temperature activation energy was the same for all three samples $U(T > 200 \text{ K}) = (0.42 \pm 0.01) \text{ eV}$. At low T , it was possible to measure an activation energy only for the less doped sample, providing $U(T < 200 \text{ K}) = (0.08 \pm 0.01) \text{ eV}$. Nevertheless, all the samples appeared to follow the same qualitative behavior.

What was the origin of the observed slope change? The total mean lifetime defined in Equation (5) was determined mainly by the slowest processes leading to the bound polaron population disappearance. In this vision, the slope of the Arrhenius plot corresponded to the activation energy of the slowest hopping process. However, if more processes with similar hopping frequency occurred in a comparable amount, the observed activation energy would somehow lie in the middle.

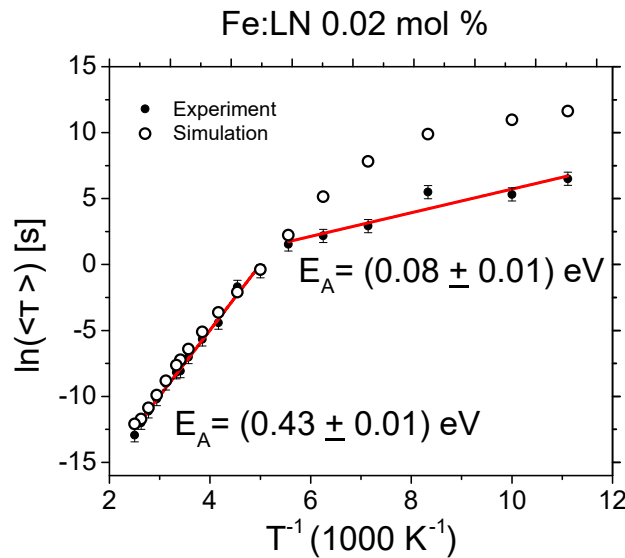


Figure 2. Cont.

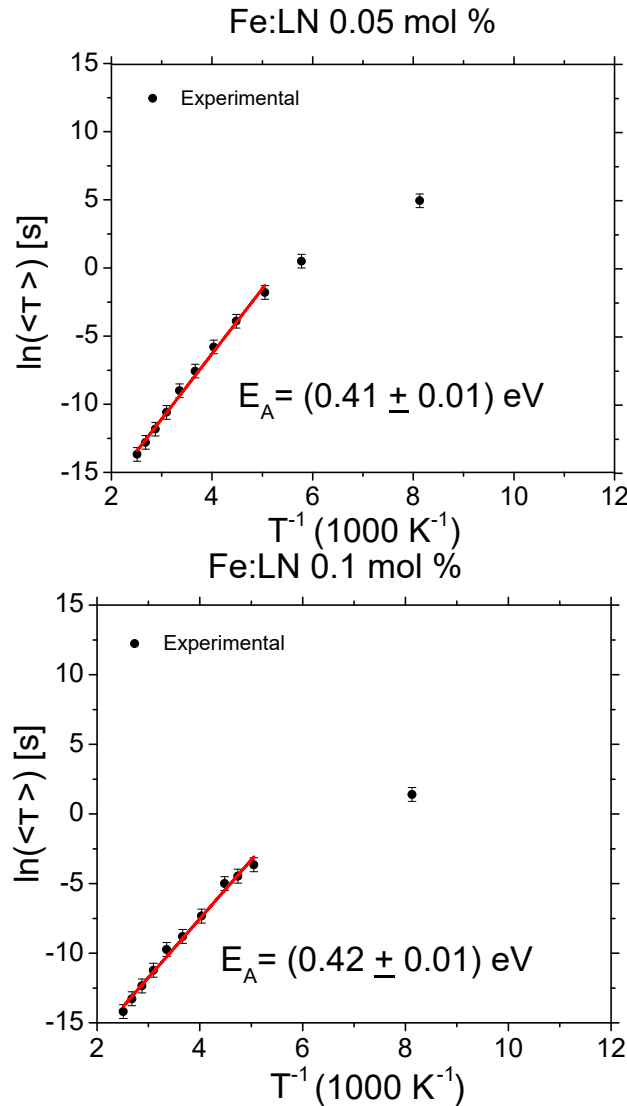


Figure 2. Arrhenius plot of the mean decay time of the signal at 785 nm, calculated using the parameters of the Kohlrausch, Williams and Watts (KWW) fit of the Transient Absorption Spectroscopy (TAS) data. The plots evidence a change in the transport mechanism around 200 K. The high temperature regime is described by an activation energy of $[U \sim 0.42]$ eV and is well matched by numerical simulations in sample Fe:LN 0.02 mol %.

Using Equation (4) and the known values of the polaron energies (see [18] and the references therein), it is possible to compute the characteristic hopping barriers for the different processes, reported in Figure 3. As can be verified by inserting some typical values in Equation (3), the processes requiring the longest time to hop away from an antisite were the $\text{Nb}_{\text{Li}} - \text{Nb}_{\text{Li}}$ and $\text{Nb}_{\text{Li}} - \text{Nb}_{\text{Nb}}$ hops, characterized by an activation energy of 0.375 eV and 0.55 eV. The measured activation energy was found in between (0.42 eV), accordingly. This means that the polaron, initially stuck on an antisite defect, either hopped directly towards another antisite or became a free polaron (which can eventually move on the Nb_{Nb} lattice or re-captured by an antisite, but since those processes were very fast, they did not significantly affect the polaron lifetime).

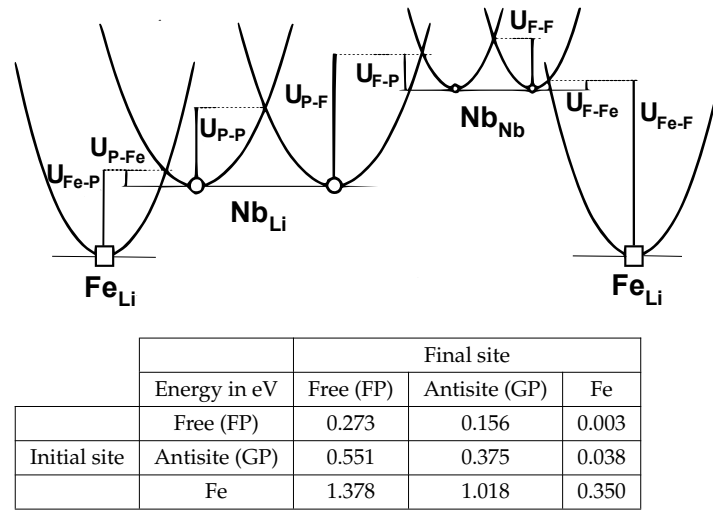


Figure 3. Hopping energy barrier (Equation (4)) calculated using the values for the different polaron energies detailed in [18]. *FP*, free polaron.

Those claims were quantitatively checked against the numerical simulations for the sample Fe:LN 0.02 mol %, for which two distinct slopes are clearly visible in the Arrhenius plot. An initial population of 5000 polarons, all forming on a $\text{Nb}_{\text{Nb}}^{4+}$ site just after the pulse, were considered. The TAS signal at 785 nm was computed by considering the weighted sum of the FP and GP populations $\alpha_{\text{Li}}(785 \text{ nm}, t) \propto \sigma_{\text{GP}}(785 \text{ nm})N_{\text{GP}}(t) + \sigma_{\text{FP}}(785 \text{ nm})N_{\text{FP}}(t)$, where $\sigma_{\text{GP}}(785 \text{ nm}) = 7 \times 10^{-22} \text{ m}$ and $\sigma_{\text{FP}}(785 \text{ nm}) = 3.1 \times 10^{-22} \text{ m}$ were the bound and free polaron cross-sections at 785 nm, respectively [23]. The numerically-computed decays were fitted by a KWW function in the experimental range starting from 10^{-8} s , and the average lifetime was calculated using Equation (5). The results are plotted in Figure 2. It can be seen that in the range between 180 and 400 K, the agreement between the simulated and experimental data was excellent, and the same situation was obtained for the other samples (not shown). Below 180 K, however, the agreement is less satisfactory: although the simulated data correctly reproduced the fact that the activation energy passed from $U \sim 0.42 \text{ eV}$ to $U \sim 0.08 \text{ eV}$, the experimentally-measured transition appeared to be sharper, and the simulated decays were several times slower than the experimental ones. One possible explanation for this disagreement was that at low temperatures, the Marcus–Holstein hopping frequency became inaccurate [13,14]. Another reason may stem from the fact that in our simulation, we disregarded the presence of holes, and this assumption may be not be fully adequate in sample Fe:LN 0.02 mol %, which contained the lowest concentration of Fe. A third possible explanation was that the absorption at 785 nm may have contained an additional contribution from some other center than GP and FP, decaying by an alternative relaxation channel. This problem was already apparent also in [18] in which the sample Fe:LN 0.02 mol % was analyzed from the point of view of the decay shape, obtaining a set of parameters somehow different from that in other samples, especially concerning the trapping parameter $a_{\text{GP-Fe}} = c$.

Despite the partial agreement, our simulations reproduced qualitatively the observed activation energy change. An inspection of the results indicated that at low temperatures, the number of hops decreased significantly to a few units and, in many cases, even to a single trapping event. Therefore, the change in the activation energy can be associated with what we may call the “trapping” regime, in which the polaron performed a very limited hop number, so that the pertinent activation energy was somehow in between the energy barrier for the different trapping processes: $\text{Nb}_{\text{Li}}^{4+} - \text{Fe}_{\text{Li}}^{3+}$ and $\text{Nb}_{\text{Nb}}^{4+} - \text{Fe}_{\text{Li}}^{3+}$ (see Figure 3).

4.2. Hopping Regimes' Landscapes Inspected by Monte Carlo Simulations

One of the most intriguing question concerns the understanding of the role played by the different types of polarons, according to temperature, Nb_{Li} antisites and Fe concentration. With the analysis of the activation energy of the mean lifetime, we obtained an indication that, depending on the temperature, different hopping processes can take place. It was only possible to conclude that at a high temperature, a mixed transport made by Nb_{Nb}^{4+} free and Nb_{Li}^{4+} bound polarons occurred, while at a low temperature, the iron had a greater impact on the results. These respective parts in light-induced transport are still an open question. The present section aims to study the interplay between these species and predict which type of transport should predominate, depending on temperature and trap concentrations, with the help of the Monte Carlo simulation.

4.2.1. Free Polaron Transport

To evaluate quantitatively the role of FP in charge transport, we can calculate, for a polaron performing N_{tot} hops from its birth to its death, the fraction N_{FP-FP}/N_{tot} of $Nb_{Nb}^{4+} \rightarrow Nb_{Nb}^{4+}$ hops performed as a free polaron. This quantity was then averaged over a large number of realizations. The calculation was performed by simulating 5000 polarons using the microscopic parameters reported in [18]. The experimental conditions (antisites and Fe traps concentration and temperature) were varied, to explore the typical range of parameters encountered in standard situations.

On the left side of Figure 4, we investigate the effect of the sample composition and of the temperature on the free polaron contribution to conduction. Here, the Fe concentration was set to zero. This situation therefore describes the impact of the stoichiometry or of doping with photorefractive-resistant ions (Mg, Zn, Zr) on the conduction. It can be seen that at room temperature, the reduction of the $[Nb_{Li}]$ concentration initially had a small influence on the amount of FP-FP hops. It was necessary to eliminate about 90% of the antisites before observing a steep increase in the free polaron contribution to the conduction. This result explained quantitatively the origin of the so-called photorefractive threshold, which was necessary to surpass in order to observe a marked decrease of the photorefractive effect in undoped LN [29]. The situation was even more extreme at low temperatures and, conversely, more gradual by heating the sample.

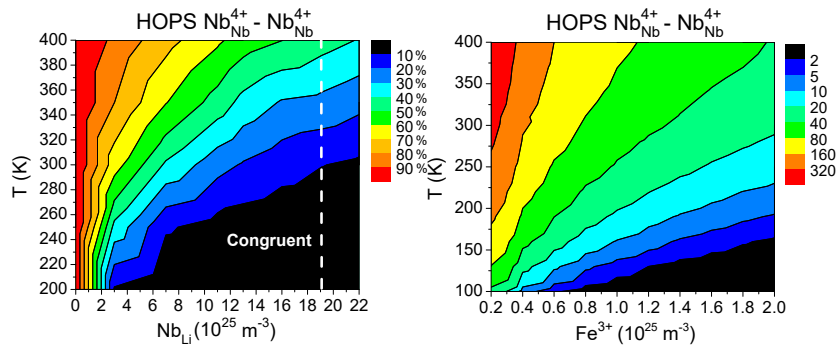


Figure 4. (Left) Fraction of hops as a free polaron N_{FP-FP}/N_{tot} as a function of temperature and $[Nb_{Li}]$ concentration for an undoped sample ($[Fe] = 0$). (Right) Total number of hops N_{FP-FP} as a function of the temperature and $[Fe]$ concentration for a stoichiometric sample ($[Nb_{Li}] = 0$).

On the right side of Figure 4, we consider now the impact of Fe doping from the point of view of free polaron conduction. We considered a stoichiometric sample to distinguish the effect of shallow Nb_{Li}^{5+} traps. The qualitative behavior was obviously similar. In this case, it is interesting to note that at room temperature, even for high Fe concentrations ($2 \times 10^{25} m^{-3}$), the free polarons were always able to perform on average several hops before being trapped. This is in contrast, as we will show below, with the behavior of bound polarons.

4.2.2. Bound Polaron Transport

As has been shown in the above paragraph, when some antisites were present and for not too elevated temperatures (Figure 4 (left)), only a limited percentage of the hops that a polaron performed during its life were of the $\text{Nb}_{\text{Nb}}^{4+} \rightarrow \text{Nb}_{\text{Nb}}^{4+}$ type. In Figure 5 (left), the same analysis is carried out for $\text{Nb}_{\text{Li}}^{4+} \rightarrow \text{Nb}_{\text{Li}}^{4+}$ hops. Here, the situation was reversed: if the temperature was not too high and the antisite concentration was close to the congruent one, a large (on average) percentage of the total hops was constituted by direct hops among antisite defects. This led us to the important conclusion that in standard conditions, i.e., a congruent material at room temperature (and below), the dominating polaronic species was the bound polaron, hopping directly among antisite defects. This situation was completely different with respect to the free polaron case, because bound polarons hopped on a disordered lattice, for which standard diffusion equations may not be valid [16]. Two important remarks are necessary: (i) the fact that a large percentage of hops was performed as a bound polaron does not necessarily mean that charge transport was ruled by bound polarons: free polarons were so much more mobile than bound ones that, even if they were scarce, they could carry charge in a very efficient way; (ii) even if some hops were performed as free polarons, their concentration remained small, because they performed their hops very quickly before being recaptured very soon either by a $\text{Nb}_{\text{Li}}^{5+}$ shallow trap or by a Fe^{3+} deep trap. Therefore, the rate at which they were produced was much slower than the rate at which they disappeared, so that their equilibrium concentration remained very limited. This was confirmed by our experimental TAS results showing that the signal at 1310 nm remained small or close to zero, especially at a low temperature.

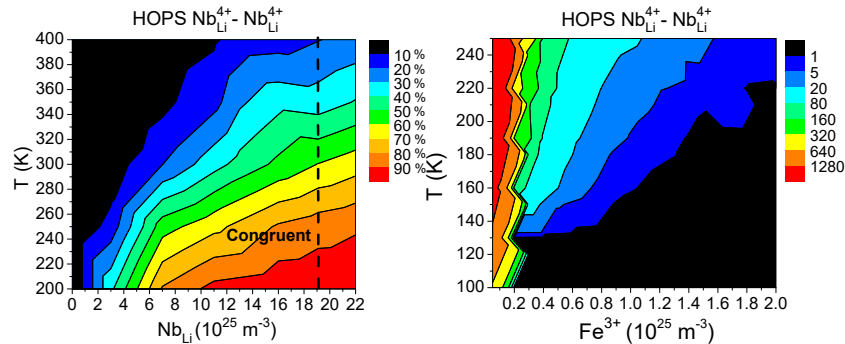


Figure 5. (Left) N_{GP-GP}/N_{tot} as a function of temperature and antisite concentration for an undoped sample ($[\text{Fe}] = 0$). (Right) N_{GP-GP} as a function of the temperature and $[\text{Fe}]$ concentration for a congruent sample ($[\text{Nb}_{\text{Li}}] = 19 \times 10^{25} \text{ m}^{-3}$). Free polaron contribution has been disregarded for simplicity. Note the different temperature range in the two plots.

The influence of iron traps on $\text{Nb}_{\text{Li}}^{4+}$ polarons is shown in Figure 5 (right). In this case, the contribution of free polaron can be disregarded because this analysis was performed at a low temperature for congruent composition, to reduce the computational cost of this simulation. Here, the situation was even more dramatic if compared to the free polarons case, because at a low temperature, even with a relatively low concentration of deep traps, the bound polaron could perform at most one single jump. The data shown in Figure 5 (right) may be taken as an overestimation because of the so-called “soft pair” effect. In other words, the Nb_{Li} polaron can perform in some cases a large number of hops back and forth between two close-by antisite defects, without contributing effectively to the transport. In any case, this graph can be used to look for the conditions for which the number of hops becomes smaller than one. This corresponds to the situation for which at a low temperature, the bound polarons were directly trapped by a Fe^{3+} , and the transport process was no longer based on $\text{Nb}_{\text{Li}}^{4+} \rightarrow \text{Nb}_{\text{Li}}^{4+}$ hops, but on $\text{Nb}_{\text{Li}}^{4+} \rightarrow \text{Fe}^{3+}$ ones. This is in qualitative agreement with the results of Figure 2, which show the gradual change in the activation energy

of the average hopping frequency by cooling down the sample. The measured activation energy ($E_A = (0.08 \pm 0.01)$ eV) at a low temperature in sample Fe:LN 0.02 mol % corresponded to a mix of hopping processes of the type $\text{Nb}_{\text{Li}}^{4+} \rightarrow \text{Nb}_{\text{Li}}^{4+}$ and $\text{Nb}_{\text{Li}}^{4+} \rightarrow \text{Fe}^{3+}$, with an apparent activation energy in between the ones of the corresponding processes reported in Equation (4) ($U_{GP-GP} = 0.375$ eV and $U_{GP-Fe} = 0.038$ eV, respectively).

5. Conclusions

In this work, we investigated how the relative weight of the different hopping processes for small polarons in Fe:LN was influenced by sample composition and temperature. A change in the hopping processes was evidenced experimentally by measuring the activation energy of the photo-generated electron polarons' lifetime for different trap concentrations and different temperatures. The activation energy passes from about 0.42 eV at room temperature to 0.08 eV at a low temperature. By a numerical analysis based on the Marcus–Holstein theory, we were able to ascribe the transport to a mix of hop $\text{Nb}_{\text{Li}}^{4+} \rightarrow \text{Nb}_{\text{Li}}^{4+}$ (GP–GP) and $\text{Nb}_{\text{Nb}}^{4+} \rightarrow \text{Nb}_{\text{Nb}}^{4+}$ (FP–FP) types. At high temperatures and low antisite concentrations, the number of hops performed as free polarons was dominant, so that the effective mobility approached the ideal “free polaron” case described by Equation (1). In standard conditions, i.e., at room temperature and congruent composition, the “antisite” hopping GP–GP occurred more frequently than free polaron hopping FP–FP, and by cooling down the sample, it became preponderant. Still, the role of free polaron conduction cannot be neglected: because of their much higher mobility, even a scarce presence of free polarons may significantly affect the conductivity. Finally, at very low temperatures (below 150 K) and for the range of compositions herein considered, one entered another regime in which the polarons typically performed only one or two hops before being captured by a deep Fe^{3+} trap. In these conditions, the activation energy of the transport process was close to the one of the trapping event, which was $U_{GP-Fe} = 0.038$ eV. We point out that in recent works [17,18], a useful scheme, based on the idea of associating a finite volume with deep and shallow traps, has been proposed that allows for a semi-quantitative description of our findings without resorting to numerical simulations.

Our results confirmed that in real materials, the situation was much more intricate than in the ideal case, and that numerical studies can effectively be used to investigate the role of the different polaronic species. As a future perspective, we plan to apply this approach to the practically important topic of transport processes under continuous illumination. As shown here, the effective polaron mobility resulted in general from a mix between free and bound polarons contributions. While for the former, a standard theoretical description is available, for the latter, the situation is more complicated, because they can be considered as particles hopping on the disordered lattice constituted by antisite defects, for which standard diffusion equations may not be valid. This may ultimately lead to a revision of the theoretical description of polaron conduction in lithium niobate and related materials.

Author Contributions: Conceptualization, M.B. Data curation, L.V. and S.M. Formal analysis, L.V. Investigation, L.V. and S.M. Methodology, M.B. Resources, M.I. Supervision, M.B. and M.I. Writing, original draft, M.B. Writing, review and editing, S.M. and M.I.

Funding: This research was funded by the University of Padova grant number BIRD174398 and by the Deutsche Forschungsgemeinschaft (DFG) via Projects IM37/11-1 and INST190/165-1 FUGG.

Acknowledgments: M.B. thanks Laurent Guilbert from LMOPS laboratory at Université Lorraine and CentraleSupélec (Metz, France) for providing useful ideas and discussions.

Conflicts of Interest: The authors declare no conflict of interest.

References

1. Imlau, M.; Badorreck, H.; Merschjann, C. Optical nonlinearities of small polarons in lithium niobate. *Appl. Phys. Rev.* **2015**, *2*, 040606. [[CrossRef](#)]
2. Bazzan, M.; Sada, C. Optical waveguides in lithium niobate: Recent developments and applications. *Appl. Phys. Rev.* **2015**, *2*, 040603. [[CrossRef](#)]

3. Günter, P.; Huignard, J.-P. *Photorefractive Materials and Their Applications 1*; Springer: New York, NY, USA, 2006; Volume 113.
4. He, J.; Franchini, C.; Rondinelli, J.M. Lithium niobate-type oxides as visible light photovoltaic materials. *Chem. Mater.* **2016**, *28*, 25–29. [[CrossRef](#)]
5. Schirmer, O.F.; Imlau, M.; Merschjann, C. Bulk photovoltaic effect of LiNbO₃: Fe and its small-polaron-based microscopic interpretation. *Phys. Rev. B* **2011**, *83*, 165106. [[CrossRef](#)]
6. Tisdale, W.A.; Williams, K.J.; Timp, B.A.; Norris, D.J.; Aydil, E.S.; Zhu, X.-Y. Hot-electron transfer from semiconductor nanocrystals. *Science* **2010**, *328*, 1543–1547. [[CrossRef](#)] [[PubMed](#)]
7. Nolan, M. First-principles prediction of new photocatalyst materials with visible-light absorption and improved charge separation: Surface modification of rutile TiO₂ with nanoclusters of MgO and Ga₂O₃. *ACS Appl. Mater. Interfaces* **2012**, *4*, 5863–5871. [[CrossRef](#)] [[PubMed](#)]
8. Migani, A.; Blancafort, L. Excitonic interfacial proton-coupled electron transfer mechanism in the photocatalytic oxidation of methanol to formaldehyde on TiO₂(110). *J. Am. Chem. Soc.* **2016**, *138*, 16165–16173. [[CrossRef](#)] [[PubMed](#)]
9. Sezen, H.; Shang, H.; Bebensee, F.; Yang, C.; Buchholz, M.; Nefedov, A.; Heissler, S.; Carbogno, C.; Scheffler, M.; Rinke, P.; et al. Evidence for photogenerated intermediate hole polarons in ZnO. *Nat. Commun.* **2015**, *6*, 6901. [[CrossRef](#)] [[PubMed](#)]
10. Volk, T.; Wöhlecke, M. *Lithium Niobate: Defects, Photorefraction and Ferroelectric Switching*; Springer Science & Business Media: Berlin/Heidelberg, Germany, 2008; Volume 115.
11. Marcus, R.A. On the theory of oxidation-reduction reactions involving electron transfer. I. *J. Chem. Phys.* **1956**, *24*, 966–978. [[CrossRef](#)]
12. Holstein, T. Studies of polaron motion: Part II. The “small” polaron. *Ann. Phys.* **1959**, *8*, 343–389. [[CrossRef](#)]
13. Emin, D. *Polarons*; Cambridge University Press: Cambridge, UK, 2013.
14. Austin, I.G.; Mott, N.F. Polarons in crystalline and non-crystalline materials. *Adv. Phys.* **2001**, *50*, 757–812. [[CrossRef](#)]
15. Schirmer, O.F.; Imlau, M.; Merschjann, C.; Schoke, B. Electron small polarons and bipolarons in LiNbO₃. *J. Phys. Condens. Matter* **2009**, *21*, 123201. [[CrossRef](#)] [[PubMed](#)]
16. Metzler, R.; Klafter, J. The random walk’s guide to anomalous diffusion: A fractional dynamics approach. *Phys. Rep.* **2000**, *339*, 1–77. [[CrossRef](#)]
17. Mhaouech, I.; Guilbert, L. Temperature dependence of small polaron population decays in iron-doped lithium niobate by monte carlo simulations. *Solid State Sci.* **2016**, *60*, 28–36. [[CrossRef](#)]
18. Guilbert, L.; Vittadello, L.; Bazzan, M.; Mhaouech, I.; Messerschmidt, S.; Imlau, M. The elusive role of Nb_{Li} bound polaron energy in hopping charge transport in Fe:LiNbO₃. *J. Phys. Condens. Matter* **2018**, *30*, 125701. [[CrossRef](#)] [[PubMed](#)]
19. Herth, P.; Granzow, T.; Schaniel, D.; Woike, T.; Imlau, M.; Krätzig, E. Evidence for light-induced hole polarons in LiNbO₃. *Phys. Rev. Lett.* **2005**, *95*, 067404. [[CrossRef](#)] [[PubMed](#)]
20. Ciampolillo, M.V.; Zaltron, A.; Bazzan, M.; Argiolas, N.; Sada, C. Quantification of iron (Fe) in lithium niobate by optical absorption. *Appl. Spectrosc.* **2011**, *65*, 216–220. [[CrossRef](#)]
21. Kurz, H.; Krätzig, E.; Keune, W.; Engelmann, H.; Gonser, U.; Dischler, B.; Räuber, A. Photorefractive centers in LiNbO₃, studied by optical-, mössbauer-and epr-methods. *Appl. Phys. A Mater. Sci. Process.* **1977**, *12*, 355–368. [[CrossRef](#)]
22. Merschjann, C.; Schoke, B.; Imlau, M. Influence of chemical reduction on the particular number densities of light-induced small electron and hole polarons in nominally pure LiNbO₃. *Phys. Rev. B* **2007**, *76*, 085114. [[CrossRef](#)]
23. Merschjann, C.; Schoke, B.; Conradi, D.; Imlau, M.; Corradi, G.; Polgar, K. Absorption cross sections and number densities of electron and hole polarons in congruently melting LiNbO₃. *J. Phys. Condens. Matter* **2008**, *21*, 015906. [[CrossRef](#)] [[PubMed](#)]
24. Kohlrausch, R. Ueber das dellmann’sche elektrometer. *Annalen der Physik* **1847**, *148*, 353–405. [[CrossRef](#)]
25. Berben, D.; Buse, K.; Wevering, S.; Herth, P.; Imlau, M.; Woike, T. Lifetime of small polarons in iron-doped lithium-niobate crystals. *J. Appl. Phys.* **2000**, *87*, 1034–1041. [[CrossRef](#)]
26. Carnicero, J.; Carrascosa, M.; García, G.; Agulló-López, F. Site correlation effects in the dynamics of iron impurities Fe²⁺ / Fe³⁺ and antisite defects Nb_{Li}⁴⁺ / Nb_{Li}⁵⁺ after a short-pulse excitation in LiNbO₃. *Phys. Rev. B* **2005**, *72*, 245108. [[CrossRef](#)]

27. Zylbersztein, A. Thermally activated trapping in Fe-doped LiNbO₃. *Appl. Phys. Lett.* **1976**, *29*, 778–780. [[CrossRef](#)]
28. Sheri, L.; Shamblin, B.C.; Hancock, Y.D.; Michael, J.P. Interpretation of relaxation time constants for amorphous pharmaceutical systems. *J. Pharm. Sci.* **2000**, *89*, 417–427.
29. Wöhlecke, M.; Volk, T. *Lithium Niobate*; Springer: Berlin/Heidelberg, Germany, 2009.



© 2018 by the authors. Licensee MDPI, Basel, Switzerland. This article is an open access article distributed under the terms and conditions of the Creative Commons Attribution (CC BY) license (<http://creativecommons.org/licenses/by/4.0/>).

A.3 Picosecond near-to-mid-infrared absorption of pulse-injected small polarons in magnesium doped lithium niobate

- Felix Freytag, Phillip Booker, Gábor Corradi, Simon Messerschmidt, Andreas Krampf, and Mirco Imlau

Picosecond near-to-mid-infrared absorption of pulse-injected small polarons in magnesium doped lithium niobate

Opt. Mater. Express **8**, 1505-1514 (2018); doi: 10.1364/OME.8.001505

©2018 Optical Society of America. Users may use, reuse, and build upon the article, or use the article for text or data mining, so long as such uses are for non-commercial purposes and appropriate attribution is maintained. All other rights are reserved.



Picosecond near-to-mid-infrared absorption of pulse-injected small polarons in magnesium doped lithium niobate

FELIX FREYTAG,¹ PHILLIP BOOKER,² GÁBOR CORRADI,³ SIMON MESSERSCHMIDT,¹ ANDREAS KRAMPF,¹ AND MIRCO IMLAU^{1,*}

¹School of Physics, Osnabrueck University, Barbarastrasse 7, 49076 Osnabrueck, Germany

²Laser Zentrum Hannover e.V., Hollerithallee 8, 30419 Hannover, Germany

³Wigner Research Centre for Physics, Institute for Solid State Physics and Optics, Hungarian Academy of Sciences, Konkoly-Thege u. 29-33, 1121 Budapest, Hungary

*mimlau@uos.de

Abstract: Femtosecond-pulse-induced ($E_{\text{pump}} = 2.5$ eV) picosecond infrared absorption is studied in the spectral region between 0.30 eV and 1.05 eV in LiNbO₃:Mg. We find a non-instantaneous mid-infrared absorption peak in the time domain up to 1 ps and a broad-band, long-lived absorption (maximum at 0.85 eV, width ≈ 0.5 eV), for $t > 1$ ps. The modelling succeeds by considering small Nb⁴⁺ electron polaron formation along the sequence: (i) two-photon injection of hot electron-hole pairs at Nb-O-octahedra, (ii) dissociation and electron cooling by electron-phonon-scattering, and (iii) electron self-localization by strong electron-phonon-coupling.

© 2018 Optical Society of America under the terms of the [OSA Open Access Publishing Agreement](#)

OCIS codes: (190.4720) Optical nonlinearities of condensed matter; (300.6340) Spectroscopy, infrared; (320.2250) Femtosecond phenomena.

References and links

1. Y. Furukawa, K. Kitamura, A. Alexandrovski, R. K. Route, M. M. Fejer, and G. Foulon, "Green-induced infrared absorption in MgO doped LiNbO₃," *Appl. Phys. Lett.* **78**, 1970–1972 (2001).
2. J. Hirohashi, V. Pasiskevicius, S. Wang, and F. Laurell, "Picosecond blue-light-induced infrared absorption in single-domain and periodically poled ferroelectrics," *J. Appl. Phys.* **101**, 033105 (2007).
3. S. Favre, T. Sidler, and R.-P. Salathe, "High-power long-pulse second harmonic generation and optical damage with free-running Nd: YAG laser," *IEEE J. Quantum Electron.* **39**, 733–740 (2003).
4. R. M. Wood, *Laser-Induced Damage of Optical Materials (Series in Optics and Optoelectronics)* (CRC Press, 2003).
5. G. Li and X. Xu, "Thermally induced dephasing of high power second harmonic generation in MgO:LiNbO₃ waveguides," *Chin. Opt. Lett.* **9**, 121901–121904 (2011).
6. O. F. Schirmer, "O⁻ bound small polarons in oxide materials," *J. Phys. Condens. Matter* **18**, R667–R704 (2006).
7. O. F. Schirmer, M. Imlau, C. Merschjann, and B. Schoke, "Electron small polarons and bipolarons in LiNbO₃," *J. Phys. Condens. Matter* **21**, 123201 (2009).
8. D. Emin, "Optical properties of large and small polarons and bipolarons," *Phys. Rev. B* **48**, 13691–13702 (1993).
9. Y. Qiu, K. B. Ucer, and R. T. Williams, "Formation time of a small electron polaron in LiNbO₃: Measurements and interpretation," *Phys. Status Solidi C* **2**, 232–235 (2005).
10. T. Holstein, "Studies of polaron motion," *Annals Phys.* **8**, 343–389 (1959).
11. D. Berben, K. Buse, S. Wevering, P. Herth, M. Imlau, and T. Woike, "Lifetime of small polarons in iron-doped lithium-niobate crystals," *J. Appl. Phys.* **87**, 1034–1041 (2000).
12. O. Beyer, D. Maxein, T. Woike, and K. Buse, "Generation of small bound polarons in lithium niobate crystals on the subpicosecond time scale," *Appl. Phys. B* **83**, 527–530 (2006).
13. D. A. Bryan, R. Gerson, and H. E. Tomaschke, "Increased optical damage resistance in lithium niobate," *Appl. Phys. Lett.* **44**, 847 (1984).
14. D. Conradi, C. Merschjann, B. Schoke, M. Imlau, G. Corradi, and K. Polgár, "Influence of Mg doping on the behaviour of polaron light-induced absorption in LiNbO₃," *Phys. Status Solidi RRL* **2**, 284–286 (2008).
15. S. Sasamoto, J. Hirohashi, and S. Ashihara, "Polaron Dynamics in Lithium Niobate upon Femtosecond Pulse Irradiation: Influence of Magnesium Doping and Stoichiometry Control," *J. Appl. Phys.* **105**, 083102 (2009).
16. S. Enomoto and S. Ashihara, "Comparative study on light-induced absorption between MgO:LiNbO₃ and MgO:LiTaO₃," *J. Appl. Phys.* **110**, 063111 (2011).

17. G. M. Greetham, P. Burgos, Q. Cao, I. P. Clark, P. S. Codd, R. C. Farrow, M. W. George, M. Kogimtzis, P. Matousek, A. W. Parker, M. R. Pollard, D. A. Robinson, Z. Xin, and M. Towrie, "Ultra: A unique instrument for time-resolved spectroscopy," *Appl. Spectrosc.* **64**, 1311–1319 (2010).
18. F. Xin, Z. Zhai, X. Wang, Y. Kong, J. Xu, and G. Zhang, "Threshold behavior of the einstein oscillator, electron-phonon interaction, band-edge absorption, and small hole polarons in $\text{LiNbO}_3:\text{Mg}$ crystals," *Phys. Rev. B* **86**, 165132 (2012).
19. O. Beyer, D. Maxein, K. Buse, B. Sturman, H. T. Hsieh, and D. Psaltis, "Investigation of nonlinear absorption processes with femtosecond light pulses in lithium niobate crystals," *Phys. Rev. E* **71** (2005).
20. D. Maxein, S. Kratz, P. Reckenthaeler, J. Bückers, D. Haertle, T. Woike, and K. Buse, "Polarons in magnesium-doped lithium niobate crystals induced by femtosecond light pulses," *Appl. Phys. B* **92**, 543–547 (2008).
21. X. Yang, G. Xu, H. Li, J. Zhu, and X. Wang, "Optical absorption edge of $\text{Mg} + \text{Zn}:\text{LiNbO}_3$," *Cryst. Res. Technol.* **31**, 521–527 (1996).
22. T. Roth and R. Laenen, "Absorption of free carriers in diamond determined from the visible to the mid-infrared by femtosecond two-photon absorption spectroscopy," *Opt. Commun.* **189**, 289–296 (2001).
23. R. Williams and K. Song, "The self-trapped exciton," *J. Phys. Chem. Solids* **51**, 679–716 (1990).
24. M. D. Fontana and P. Bourson, "Microstructure and defects probed by raman spectroscopy in lithium niobate crystals and devices," *Appl. Phys. Rev.* **2**, 040602 (2015).
25. G. Blasse, "Fluorescence of niobium-activated antimonates and an empirical criterion for the occurrence of luminescence," *J. Chem. Phys.* **48**, 3108–3114 (1968).
26. C. Fischer, M. Wöhlecke, T. Volk, and N. Rubinina, "Influence of the damage resistant impurities Zn and Mg on the UV-excited luminescence in LiNbO_3 ," *Phys. Status Solidi (a)* **137**, 247–255 (1993).
27. D. Emin, "Dynamics of the optically induced properties of a small-polaronic glass," *J. Non-Cryst. Solids* **35-36**, 969–973 (1980).
28. D. Emin, *Polarons* (Cambridge University Press, 2013).
29. H. Badorreck, S. Nolte, F. Freytag, P. Bäune, V. Dieckmann, and M. Imlau, "Scanning nonlinear absorption in lithium niobate over the time regime of small polaron formation," *Opt. Mater. Express* **5**, 2729 (2015).
30. M. Imlau, H. Badorreck, and C. Merschjann, "Optical nonlinearities of small polarons in lithium niobate," *Appl. Phys. Rev.* **2**, 040606 (2015).
31. B. Faust, H. Müller, and O. F. Schirmer, "Free small polarons in LiNbO_3 ," *Ferroelectrics* **153**, 297–302 (1994).
32. G. Kitaeva, K. Kuznetsov, V. Morozova, I. Naumova, A. Penin, A. Shepelev, A. Viskovatich, and D. Zhigunov, "Reduction-induced polarons and optical response of Mg -doped LiNbO_3 crystals," *Appl. Phys. B* **78**, 759–764 (2004).

1. Introduction

Pulse-induced transient absorption (TA) is a widely accepted nonlinear optical phenomenon in lithium niobate, LiNbO_3 (LN), prominently observed as green- or blue-induced infrared absorption (GRIIRA and BLIIRA) with a relaxation time of several seconds [1, 2]. Due to a long-lived transient absorption, propagating laser pulses in lithium niobate foster to a great extent the appearance of laser-induced bulk- and surface damages, and limits the conversion efficiency mainly by damping [3, 4]. It may also cause phase-detuning via localized crystal heating and the thermo-optical effect [5]. In LN, pulse-induced TA is closely connected with the optical generation of small polarons of the hole and electron type, trapped at O^{2-} and $\text{Nb}_{\text{Nb/Li}}^{5+}$ sites and absorbing in the blue and near-IR region, respectively [6, 7]. Consequently, the amplitude of the absorption maximum is expected to become proportional to the small polaron number density and the TA spectrum should be determined by the broad-bandwidth optical absorption features of small polarons [8]. The temporal evolution of TA is expected to reflect the complex path of carrier cooling and self-localization via phonon-scattering and -coupling [9], subsequent small polaron transport via thermally activated hopping [10] and its termination, e.g., via electron-hole recombination [11]. As a result, TA in LN ranges over 15 decades of time from sub-picoseconds up to seconds [12] and is best studied by a combination of ultrafast pump-probe spectroscopy (fs - ns) and conventional spectrophotometric techniques (ns - D.C.).

The effects of GRIIRA/BLIIRA can almost completely be suppressed by doping LN with Mg, Zn, etc. over their respective threshold concentrations [1]. The doping has the effect to eliminate $\text{Nb}_{\text{Li}}^{5+}$ antisite defects in LN and, thus, suppresses the formation of $\text{Nb}_{\text{Li}}^{4+}$ electron and $\text{Nb}_{\text{Li}}^{4+}:\text{Nb}_{\text{Nb}}^{4+}$ (bi-)polarons. Although the optical damage resistance is fairly increased in the visible range [13] a significant TA in the visible as well as in the infrared spectral region at timescales $< 10^{-5}$ s becomes more dominant in Mg-doped LN [14]. Despite the broad knowledge on the

dependence of GRIIRA/BLIIRA on the crystal composition only little is known about the spectral and temporal properties of TA. In particular, nearly nothing is known about the TA in the mid-IR (MIR) on the ultrafast time scale which is mandatory for the further improvement of high-power mid-infrared optical parametric oscillators (OPOs).

This contribution focuses on the spectral detection of picosecond MIR-TA in LN:Mg related to small $\text{Nb}_{\text{Nb}}^{4+}$ free polaron (FP) formation in the range between 0.30 eV and 1.05 eV that is difficult to access from the experimental point of view. Our study uncovers that free polaron TA is overlaid by a non-instantaneous, broad-band MIR absorption peak on timescales up to ≈ 1 ps that cannot be attributed to multi-photon absorption processes. Under the assumption of pulse-injection of hot-electron-hole pairs, electron-phonon-scattering and -coupling, both TA contributions can well be separated on the temporal axis. An undisturbed, broad-band small polaron absorption spectrum emerges at a temporal delay of 2 ps after the pump pulse. The obtained data set can be quantitatively modelled on the basis of theoretical expectations for the formation and absorption of small, free $\text{Nb}_{\text{Nb}}^{4+}$ polarons tested earlier using steady-state spectrophotometric techniques in thermally pre-treated Mg-doped LN and TA-measurements limited to near-IR frequencies [9, 15, 16].

2. Experiment

2.1. VIS-pump-MIR-probe spectrometer

The ps-MIR TA studies were performed by a home-made VIS-pump-MIR-probe spectrometer (schematically sketched in the insert of Fig. 1, for a typical setup see [17]) with a temporal resolution $\Delta t \approx 200$ fs, beam diameters of $d_{\text{pump}} = (500 \pm 50) \mu\text{m}$, $d_{\text{probe}} = (400 \pm 50) \mu\text{m}$ and an intersection angle of $\alpha = (8 \pm 1)^\circ$. The pump (2.5 eV; $\tau_{\text{pump}} = (100 \pm 10)$ fs; I_{pump}^0 up to $2.5 \text{ PW} \cdot \text{m}^{-2}$; $f_{\text{pump}} = 500$ Hz) and the probe (0.30 eV - 1.05 eV; $\tau_{\text{probe}} \approx 170$ fs; $I_{\text{probe}}^0 < 0.03 \text{ PW} \cdot \text{m}^{-2}$, $f_{\text{probe}} = 1$ kHz) pulses are polarized along the c-axis and within the plane of the incident pulses. The infrared signal was detected with a spectral resolution of $\Delta\omega/\omega < 10^{-3}$ and a sensitivity $\Delta\alpha/\alpha \approx 2 \cdot 10^{-2}$ (exemplarily at 0.6 eV) using a combination of a Czerny-Turner spectrograph and a mercury-cadmium-telluride-detector pixel array (32-elements). To improve the signal to noise ratio, every data point is averaged over 2000 sequential pump-probe events. A single crystal (dimensions $6 \times 7 \text{ mm}^2$; thickness $(200 \pm 10) \mu\text{m}$) of near-stoichiometric $\text{LiNbO}_3:\text{Mg}$ (Mg concentration in the melt 1.0 mol, residual iron content below 5 ppm, estimated molar Li/Nb ratio in the crystal 0.985), grown at the *WIGNER Research Centre for Physics*, Budapest, Hungary is used with a fundamental absorption in the near- to mid-infrared spectral range not exceeding $\alpha_0 = 100 \text{ m}^{-1}$ over the spectral range under investigation (0.30 eV–1.05 eV), apart from absorption due to OH^- -stretching vibrations in the spectral window $E = (0.424 - 0.443) \text{ eV}$ [13]. The exact time of maximum overlap between pump and probe pulses was determined using the signal generated via difference frequency generation (DFG) in the LN sample under study (photon energy at about 2 eV). The DFG process was enabled by a weak phase-matching condition using a very thin sample as well as a slightly non-collinear geometry (outer angle $\alpha = (8 \pm 1)^\circ$ between the incident pulses). The DFG pulse energy was measured by a standard Si-detector in transmission geometry. The temporal profile of the DFG signal was measured individually for each probe photon energy. Slight differences in the tails of the qualitatively similar profiles were observed and attributed to differences in the probe pulse durations. The two-photon absorption coefficient is determined to $\beta = (7.9 \pm 0.3) \text{ mm} \cdot \text{GW}^{-1}$ at 2.5 eV. Laser-induced damages of surface and bulk as well as cumulative effects of the MIR-TA between two sequential pump events were carefully checked, but not observed for $I_{\text{pump}}^0 = 1.4 \text{ PW} \cdot \text{m}^{-2}$.

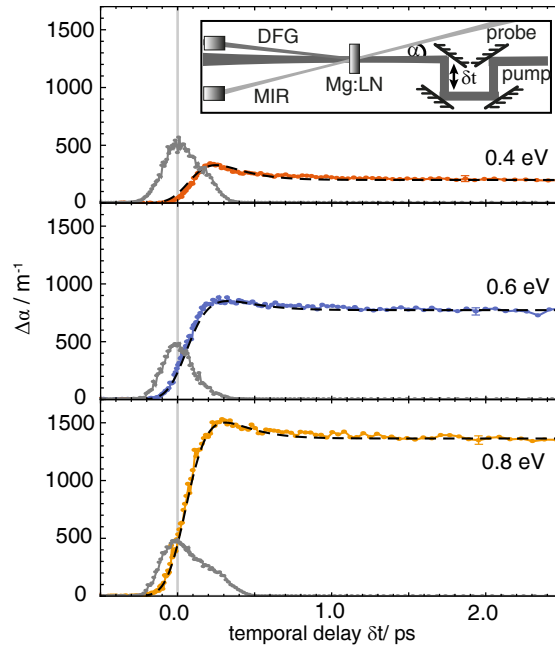


Fig. 1. Transient absorption in the ps range for a 2.5 eV pump pulse ($I_{\text{pump}}^0 = (1.4 \pm 0.2) \text{PW/m}^2$) and probe photon energies $E_{\text{probe}} = 0.40 \text{ eV}$ (3000 nm), 0.60 eV (2066 nm), 0.80 eV (1550 nm). The transient absorption is defined as $\Delta\alpha(E_{\text{probe}}, \delta t) = \alpha(E_{\text{probe}}, \delta t)_{\text{pumped}} - \alpha(E_{\text{probe}}, \delta t)_{\text{unpumped}}$. The depicted values represent the average over 2000 pump-probe events and the error margin is given by the standard deviation. The gray data points are the corresponding DFG correlation signal between pump and probe pulse (schematic setup shown in the insert) and the dotted black lines correspond to the numerical fits (see chapter 3.2).

2.2. Transient absorption of LN:Mg in the infrared spectral range

Figure 1 shows the transient absorption $\Delta\alpha(\delta t)$ of LN:Mg for three probe photon energies ($E_{\text{probe}} = 0.4 \text{ eV}$, 0.6 eV, and 0.8 eV) as examples. The vertical gray line (cf. Fig. 1) marks the zero point $\delta t = 0$ defined as the maximum of DFG between pump and probe pulses (type-II eoe phasematching). The cross-correlation signal (dark gray dots in Fig. 1) has a Full-Width-Half-Maximum (FWHM) of $(200 \pm 10) \text{ fs}$.

All transients of Fig. 1 show qualitatively similar TA dynamics: A moderate non-instantaneous absorption peak dominates the time domain up to 1 ps after the pump pulse. Its maximum shows a marked dependence on the photon energy of the probe pulse and increases from $\Delta\alpha^{\text{max}} \approx 340 \text{ m}^{-1}$ (0.4 eV) up to $\Delta\alpha^{\text{max}} \approx 1520 \text{ m}^{-1}$ (0.8 eV). It is important to note that this absorption peak has a remarkable temporal shift of $\Delta t^{\text{peak}} \approx (270 \pm 30) \text{ fs}$ (0.6 eV) compared to the pump pulse. In the time domain $t > 1 \text{ ps}$, a plateau absorption materializes with an amplitude that also depends on the photon energy. The values, e.g., at $\delta t = 2.5 \text{ ps}$, rise from $\Delta\alpha(2.5 \text{ ps}) = (200 \pm 10) \text{ m}^{-1}$ (0.4 eV) up to $\Delta\alpha(2.5 \text{ ps}) = (1350 \pm 20) \text{ m}^{-1}$ (0.8 eV) and remain constant all over the sub-ns time domain. Similar data sets were obtained for all probe photon energies in the investigated range between 0.30 eV and 1.05 eV. For photon energies below 0.4 eV as well as those above

0.8 eV, the MIR-TA shows a clear tendency to smaller values of $\Delta\alpha^{\max}$ and $\Delta\alpha(2.5\text{ ps})$. All transients were investigated as a function of pump peak energy in the range from 0.03 PW/m^2 to 2.50 PW/m^2 and for different polarizations, as well. Qualitatively, the transients show a similar behavior, but the overall absorption change rises with increasing peak energy. In particular, a quadratic dependence of non-instantaneous peak maximum and plateau absorption is found. The polarization of the beams was chosen to optimize the absorption signal (in accordance with Ref. [15]).

Similar transients were obtained for different crystals of the same boule. We have limited our study to a Mg concentration in the melt of 1.0 mol% in order to suppress the impact of either $\text{Nb}_{\text{Li}}^{4+}$ formation (for lower Mg concentrations) and of the incorporation of Mg on Nb sites (larger Mg concentrations) [18]. Furthermore, only slight differences in the observed time constants and absolute values of the absorption signals are to be expected (cf. Ref. [15]).

3. Discussion

3.1. Carrier-formation path

These data cannot be explained straightforwardly with the state-of-the-art knowledge of picosecond TA in LN and provide further insights into the optical formation of small $\text{Nb}_{\text{Nb}}^{4+}$ electron polarons. In particular, to our knowledge, there are no reports on a temporal shift of the absorption peak of the TA with respect to the incident pump pulse in LN for any probe energy. This observation most likely remained inaccessible since the zero point $\delta t = 0$ has been assigned to the time of the maximum value of the absorption peak in recent studies. Consequently, the absorption peak itself was attributed to a *quasi-instantaneous* non-linearity, i.e., non-degenerate two- or multi-photon absorption in Refs. [15, 19, 20] using probe energies $E_{\text{probe}}=1.55\text{ eV}$ in nominally undoped LN and LN:Mg. For the given fs-pump-probe technique some delay between the pump and a non-degenerate Two-Photon-Absorption (TPA) peak might indeed be expected due to the different group velocities of the probe and pump pulse, as it has been discussed comprehensively by Beyer et al. [19]. According to our experimental approach, we here need to consider the GVD difference between the probe and the DFG pulses. For this case, our calculations reveal temporal corrections of up to $\delta t = (50 \pm 10)\text{ fs}$ depending on the probe photon energy. These values are below our temporal resolution ($\approx 200\text{ fs}$) and below the discovered temporal offset between DFG maximum and non-instantaneous absorption peak. The temporal offset can therefore not be attributed to the effect of GVD, only. Furthermore, the probe photon energies between 0.30 eV and 1.05 eV of our experiment are insufficient to enable non-degenerate two-photon absorption with a pump photon energy of 2.5 eV at a band gap energy of LN of $\approx 3.92\text{ eV}$ [21]. Three-photon interaction of two VIS and one MIR photons may be assumed, instead, but this does not comply with the considerable TA signal amplitudes of our study. However a similar shift of the peak-absorption, dependent on the photon energy, has been reported for diamond [22]. The authors attribute this phenomenon to the long-lasting presence of electrons within the conduction band.

In what follows, we attribute our findings to small $\text{Nb}_{\text{Nb}}^{4+}$ electron polaron formation according to the process schematically depicted in Fig. 2.

It is reasonable to expect the excitation of hot electron-hole pairs (hot excitons) to occur in a process localized within a Nb-O-octahedron of the LN structure. Such e^-h^+ -pairs may recombine immediately (1) or may become self-trapped as self-trapped excitons (STE) [23] by strong coupling to the lattice (2). According to the phonon frequencies in LN up to the 10 THz range [24], the latter process will be delayed by a few hundreds of femtoseconds. It is noteworthy that the STE decay is closely connected with the emission of light in the blue-green spectrum in Mg-doped LN crystals [25, 26] as used in our present study. Path (3) marks the possibility of phonon-assisted small polaron formation from an essentially unrelaxed e^-h^+ -pair [27] by transfer of the electron to a next-neighboring $\text{Nb}_{\text{Nb}}^{5+}$ ion (analogously, a transfer of a hole to a next

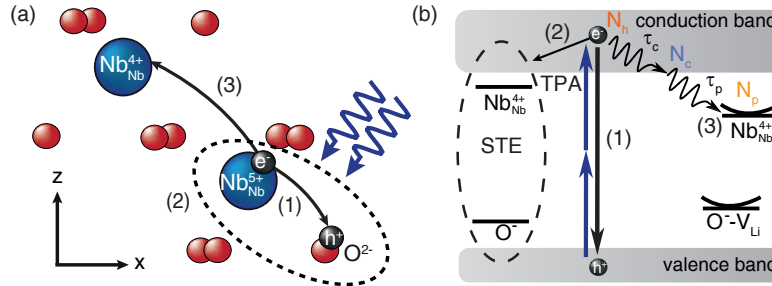


Fig. 2. Recombination paths of fs-pulse generated hot electrons and holes in LN:Mg displayed (a) in a model of the atomic structure and (b) in an energy level diagram. Three recombination paths are considered: (1) the direct recombination of electrons and holes, (2) the formation of self-trapped excitons within a Nb-O-octahedron, and (3) the phonon-assisted formation of small polarons. Our modelling of Eqs. 1-3 is based on relaxation path (3), i.e., paths (1) and (2) are disregarded in our model. This assumption accords with our experimental setup and crystal choice being tailored for small free polaron detection. Furthermore, it considers the comparably low probability for paths (1) and (2).

neighboring O^{2-} also resulting in the dissociation of the e^-h^+ -pair may also be considered). This electron will be cooled by means of electron-phonon scattering prior to self-localization via electron-phonon coupling. From the perspective of our experiment, we will be able to detect the MIR absorption features of cooled electrons and Nb_{Nb}^{4+} electron polarons. In contrast, hot exciton states, that most probably show a UV/blue absorption feature, may not be accessible within the spectral region of our probe pulse. As a result, the transients in the MIR should reflect at least two main characteristic time constants: τ_c that takes into account the phonon-assisted processes of e^-h^+ dissociation and hot-electron cooling and τ_p that is determined by the response time of the lattice.

A very similar understanding of TA related to small free Nb_{Nb}^{4+} polaron formation in MgO-doped LN was presented by Qiu et al. [9]. Although a non-instantaneous absorption peak of TPA was not observed, after a delay of the order of 1 ps a long-lived absorption plateau with rise time of about 200 fs at room temperature was clearly discovered and attributed to the formation of Nb_{Nb}^{4+} polarons. The delay was assigned to phonon-assisted cooling of optically excited hot carriers and the time required for carrier localization by electron-phonon coupling. We here note, that paths (1-3) represent three different options for the initially generated electron hole pair. According to D. Emin [28] a sequence of paths (2) \rightarrow (3) may occur, i.e., the transformation of a STE into a Nb_{Nb}^{4+} electron and O^- hole polaron. In our modelling, however, we disregard paths (1) and (2) as well as a sequential formation process due to a low probability for these processes. In agreement with a theoretical estimate, a delay time of about 80 fs [9] was deduced for the cooling process. In a recent work of Badorreck et al. [29], we were able to verify this delay-time experimentally in nominally undoped, congruent LN with a value of $\tau_c \approx 80$ fs for a TPA excitation process at 2.5 eV, i.e., equivalent to this work.

The characteristics of the absorption plateau remain in full accordance with the state-of-the-art knowledge on TA in the near-infrared spectral range. Its interpretation via small, strong-coupling Nb_{Nb}^{4+} electron polarons is verified by a temperature dependent formation time of a few hundred femtoseconds [9, 15, 19, 20]. The respective decay process obeys a stretched-exponential behavior with a decay time in the regime of a few hundred nanoseconds (over-threshold LN:Mg) [14, 15, 20]. This is short enough to avoid cumulative effects upon repetitive polaron formation at frequencies of 1 kHz.

3.2. Modelling

Based on these considerations, we will now turn to the numerical analysis of our data applying the following set of rate equations:

$$\frac{\partial N_h(L, t)}{\partial t} = \frac{\beta I^2(L, t)}{2\hbar\omega} - \frac{N_h(L, t)}{\tau_c} \quad (1)$$

$$\frac{\partial N_c(L, t)}{\partial t} = \frac{N_h(L, t)}{\tau_c} - \frac{N_c(L, t)}{\tau_p} \quad (2)$$

$$\frac{\partial N_p(L, t)}{\partial t} = \frac{N_c(L, t)}{\tau_p}, \quad (3)$$

where L is a coordinate along the light propagation direction in the crystal, β the TPA-coefficient at the photon energy of the pump pulse $\hbar\omega$, $N_{h,c,p}$ the number densities of injected hot electrons, cold electrons, and polarons, respectively and $I(L, t)$ is the pump light intensity inside the crystal for a gaussian shaped pulse influenced by two-photon absorption based on the considerations from Beyer et al. [19]:

$$I(t, L) = \frac{2 \cdot \exp[-4 \log(2) \left(\frac{t}{\tau_{\text{pump}}}\right)^2]}{\beta L \sqrt{\pi}} \int_0^\infty \ln[1 + \beta I_{\text{pump}}^0 L \cdot \exp(-s^2)] ds. \quad (4)$$

The calculated transient absorption signal α_{calc} is given by the mean value over the sample length d of the sum of three individual number densities multiplied by their respective absorption cross sections:

$$\alpha_{\text{calc}}(t) = \frac{1}{d} \int_0^d [\sigma_p \cdot N_p(L, t) + \sigma_h \cdot N_h(L, t) + \sigma_c \cdot N_c(L, t)] dL. \quad (5)$$

For comparison with the experimentally determined transient absorption α_{exp} the calculated absorption α_{calc} has to be convolved with the gaussian temporal envelope of the probe pulse:

$$\alpha_{\text{exp}}(\Delta t) = 2 \sqrt{\frac{\log(2)}{\pi \tau_{\text{probe}}^2}} \int_{-\infty}^{\infty} \alpha_{\text{calc}}(t) \cdot \exp\left[-4 \log(2) \left(\frac{t - \Delta t}{\tau_{\text{probe}}}\right)^2\right] dt \quad (6)$$

This interplay of three types of carriers (see Eq. 5) is the key for a successful modelling of the determined characteristics of the MIR-TA. The numerical solution of equations (1)-(6) with the simultaneous fitting of the parameters $\tau_{c,p}$ and $\sigma_{h,c,p}$ could only be performed with the following restrictions: (i) at $t = -300$ fs the number densities of all carriers are assumed to be zero, (ii) according to the sequence of carriers in our approach the number densities initially have to fulfill the relation $N_h^{\text{total}} \geq N_c^{\text{total}} \geq N_p^{\text{total}}$, (iii) the absorption cross section of hot electrons in the MIR is neglected: $\sigma_h \approx 0$, and (iv) electronic cooling stages are faster than lattice relaxation (both on the sub-ps scale): $\tau_c < \tau_p \ll 1$ ps. Again, we note that losses of the probe pulse by three-photon absorption including the pump pulse are not considered.

Figure 3 compares the spatially integrated, convolved outcome of fitting equation (6) (green line) to the experimental data set (green dots), exemplarily for $E_{\text{probe}} = 0.6$ eV.

The temporal evolution of the individual number densities $N_h(t)$, $N_c(t)$ and $N_p(t)$ at $L = 200 \mu\text{m}$ are depicted as determined from the solution of the rate equations (1)-(3). Fitting was performed for all spectra with a very high quality according to the fitting results depicted as dotted lines in Fig. 1 (normalized root-mean-square deviation (NRMSD) values of (7.1% (0.4 eV), 3.0%

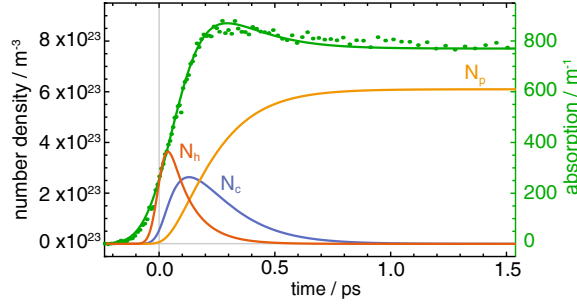


Fig. 3. Numerical fit of the transient absorption (green line) and the data set (green dots) at 0.6 eV. Fitting parameters: $\tau_c = 100$ fs and $\tau_p = 150$ fs. The dynamics of the individual number densities are calculated assuming full conversion of pump photons to hot electrons and are plotted as orange (N_h), blue (N_c) and yellow (N_p) lines. Note that N_h does not contribute to the MIR absorption as $\sigma_h = 0$, but is still fully defined due to the nonlinear term in Eq. 1.

(0.6 eV), 2.3% (0.8 eV)). We note that the fitting procedure was performed iteratively for all photon energies using the same set of free fitting parameters $\tau_c = 100$ fs, $\tau_p = 150$ fs.

All fitting parameters agree very well with previously reported values of the generation time of free (≈ 100 fs in [15]) and bound polarons (< 400 fs in [12], [30]) and the free electron cooling time (cf. $\tau_c \approx 80$ fs in [9,29]), confirming our assumptions. We note, that the sum of τ_c and τ_p may be interpreted as polaron formation time with respect to the incident pump pulse.

In the time range of -0.2 ps $< t < 1$ ps, we find that only the number densities of cold electrons and polarons contribute to the overall TA signal. For $t > 1$ ps, on the other hand, TA is solely determined by the absorption of small, strong-coupling polarons. At the same time, our fit reveals a non-zero population of hot carriers at the maximum of the incident pulse. This feature can be attributed to the temporal width of the incident pulse peak with a pulse duration of ≈ 100 fs at peak maximum $t = 0$ fs. Therefore, it must be considered that the pump pulse intensity already rises considerably at $t \approx -50$ fs that results in a non-zero population of hot carriers at $t = 0$ fs.

3.3. Small polaron fingerprint

Based on these findings, it is possible to deduce the absorption fingerprint of $\text{Nb}_{\text{Nb}}^{4+}$ electron polarons by plotting the spectral dependence of the TA signal at a fixed delay time of $t = 2$ ps as displayed in Fig. 4.

The data reveal a broad spectral distribution with a maximum at $E(h\nu)_{\text{peak}} \approx 0.80$ eV that can be applied for an estimate of the small-polaron stabilization energy E_p due to the induced lattice distortion: $E_p = (1/2)E(h\nu)_{\text{peak}} \approx 0.40$ eV. A more precise approach with respect to the asymmetric shape of the spectral distribution is given by Emin's theory of small free polarons at elevated temperatures [8]:

$$\Delta\alpha(\hbar\omega) \propto \frac{1}{\hbar\omega} \exp[-(2E_p - \hbar\omega)^2 / (8E_p k_B T)], \quad (7)$$

describing the lineshape in excellent agreement with experimental data (cf. solid line in Fig. 4), with k_B being the Boltzmann constant. The fit yields the free polaron binding energy $E_p = (0.44 \pm 0.02)$ eV, a peak maximum at $E(h\nu)_{\text{peak}} = (0.83 \pm 0.04)$ eV and a half width at half maximum of $W = (0.26 \pm 0.01)$ eV at room temperature and $t = 2$ ps. A comparison of the values obtained in this study with previous investigations using thermally stabilized small polarons

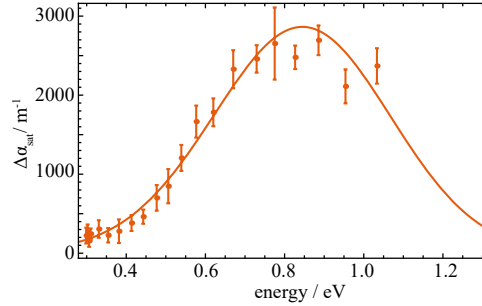


Fig. 4. Absorption fingerprint of fs-pulse induced free polarons at a fixed time delay of $t = 2$ ps ($I_{\text{pump}}^0 = (2.5 \pm 0.2) \text{PW/m}^2$). The continuous line fits Eq. 7 to the experimental data set. The error margin is given by the standard deviation and the error made by determining the light intensity.

is given in Tab. 1. The peak position is in agreement with previous studies, whereas slight differences can be seen in the case of the spectral width.

The discovered differences can be attributed to (i) the use of an asymmetric fitting function and (ii) the impact of a non-equilibrium electronic state that has to be expected on the picosecond time scale after exposure to an intense fs-laser pulse. Driving evidence for the latter conclusion is the short lifetime of a few μs of the transient absorption with a complete recovery of the involved electronic state.

Table 1. Polaron stabilization energy E_p and half width at half maximum W of the MIR absorption feature in comparison.

E_p (eV)	W (eV)	T(K)	Reference
0.44 ± 0.02	0.26 ± 0.01	295	this study
0.48	≈ 0.23	295	[31]
0.54	≈ 0.40	6	[31]
0.54	0.37	295	[7]
0.47	≈ 0.25	295	[32]

4. Conclusion & novelty

In conclusion, our analysis clarifies the picosecond transient absorption of femtosecond-pulse injected carriers during their relaxation to small free $\text{Nb}_{\text{Nb}}^{4+}$ electron polarons in the spectral range of 0.30 eV up to 1.05 eV. It extends the knowledge about the optical properties of small electron polarons to the ultrafast time regime that also comprises small polaron formation.

From a fundamental viewpoint, our findings demonstrate that the theoretical concepts about the optical properties of small, strong-coupling polarons (Holstein-Emin approach) can be transferred to the field of nonlinear optics and femtophysics in general, i.e., to the non-equilibrium state, which is indicated by a fair agreement of the spectral parameters of the TA plateau with 'steady-state' values for free polarons.

A specific result of our study is the interpretation of the TA maximum as a non-instantaneous absorption peak due to an intermediary (unrelaxed cold) electron state that cannot be attributed to the action of multiphoton absorption. This was obtained using a methodical peculiarity of fs-VIS-pump-MIR-probe spectroscopy in nonlinear optical LN that makes use of the difference frequency generation signal between pump and probe to define the exact time of maximal overlap.

By comprehensive modelling of the multi-step flow of electronic energy induced by two-photon absorption, that was missing in the literature so far, existing models for small polaron formation are supported, confirming also predictions for the lifetimes of early stages despite the negligible mid-IR absorption of hot electrons. The ps-MIR TA may be considered for fs-pulse-exposed frequency converters based on lithium niobate crystals and for the further development and engineering of demanding high-power MIR fs-laser sources using polar representatives of niobates and of the borate class (LBO, BBO, etc.).

This study may also serve as a hint for the need of a further subdivision of the small polaron formation process and will push forward studies on the appearance and transport of hot excitons by probing the UV/VIS spectral range.

Funding

Deutsche Forschungsgemeinschaft (DFG) (IM37/5-2, INST 190/137-1 FUUG, INST 190/165-1); Open Access Publishing Fund of Osnabrueck University.

Acknowledgements

The authors gratefully acknowledge crystal preparation by K. Polgár and coworkers at the Wigner Research Centre for Physics, Budapest.

A.4 The role of self-trapped excitons in polaronic recombination processes in lithium niobate

- Simon Messerschmidt, Andreas Krampf, Felix Freytag, Mirco Imlau, Laura Vitadello, Marco Bazzan, and Gábor Corradi

The role of self-trapped excitons in polaronic recombination processes in lithium niobate

J. Phys.: Condens. Matter **31** (2019); doi: 10.1088/1361-648X/aaf4df

Original content from this work may be used under the terms of the Creative Commons Attribution 3.0 licence (<http://creativecommons.org/licenses/by/3.0>). Any further distribution of this work must maintain attribution to the author(s) and the title of the work, journal citation and DOI.

The role of self-trapped excitons in polaronic recombination processes in lithium niobate

S Messerschmidt¹, A Krampf¹, F Freytag¹, M Imlau¹, L Vittadello², M Bazzan² and G Corradi³

¹ School of Physics, Osnabrueck University, Barbarastraße 7, 49076 Osnabrueck, Germany

² Dipartimento di Fisica e Astronomia, Università di Padova, Via Marzolo 8, 35131 Padova, Italy

³ Wigner Research Centre for Physics, Institute for Solid State Physics and Optics, Hungarian Academy of Sciences, Konkoly-Thege u. 29-33, 1121 Budapest, Hungary

E-mail: mirco.imlau@uni-osnabrueck.de

Received 29 June 2018, revised 21 November 2018

Accepted for publication 29 November 2018

Published 21 December 2018



CrossMark

Abstract

Transient absorption and photoluminescence are experimentally investigated in the polaronic reference system lithium niobate, LiNbO_3 (LN), with the aim to refine the microscopic model of small polaron dynamics in materials with strong electron–phonon coupling. As a unique feature, our study is performed by using two different spectroscopic methods, in crystals with dopants enhancing photorefraction or damage resistance, and over a broad temperature range from 15–400 K. Although being self-consistent for particular experimental conditions, the hitherto used microscopic polaronic models reveal inconsistencies when applied to this larger data set. We show that comprehensive modeling is unlocked by the inclusion of an additional type of polaronic state with the following characteristics: (i) strongly temperature- and dopant-dependent relaxation times, (ii) an absorption feature in the blue-green spectral range, and (iii) a Kohlrausch–Williams–Watts decay shape with a temperature-dependent stretching factor $\beta(T)$ showing a behavior contrary to that of small, strong-coupling polarons. The hypothesis of self-trapped excitons (STEs, i.e. bound electron–hole pairs strongly coupled to Nb^{5+} and O^{2-} within a niobium-oxygen octahedron) and their pinning on defects as the microscopic origin of these characteristics is supported by a spectroscopic linkage of photoluminescence at low (15 K) and elevated (300 K) temperatures and explains the long-lifetime components in transient absorption as due to pinned STEs.

Keywords: lithium niobate, transient absorption, photoluminescence, self-trapped exciton, small polaron hopping, light-induced charge transport, iron and magnesium doping

(Some figures may appear in colour only in the online journal)

1. Introduction

The study of charge carrier dynamics with strong-coupling to the lattice, e.g. small polarons and self-trapped excitons (STEs) in lithium niobate, LiNbO_3 (LN), triggered

widespread attention even in nanosciences since the verification of their decisive role in the microscopic mechanisms of ferroelectric photovoltaics [1, 2], of THz wave damping [3] and laser-induced bulk damage mechanisms [4, 5], but also of photocatalysis in other oxide dielectrics like TiO_2 , MgO , or ZnO [6–10]. LN is a ferroelectric oxide with excellent photoelectrical and (nonlinear) optical features, exhibits pronounced electron-/hole-phonon coupling, and hosts four different kinds of intrinsic small polarons [1, 4, 11, 12]:



Original content from this work may be used under the terms of the [Creative Commons Attribution 3.0 licence](https://creativecommons.org/licenses/by/3.0/). Any further distribution of this work must maintain attribution to the author(s) and the title of the work, journal citation and DOI.

the free polaron $\text{Nb}_{\text{Nb}}^{4+}$, the bound polaron $\text{Nb}_{\text{Li}}^{4+}$, the bipolaron $\text{Nb}_{\text{Li}}^{4+}:\text{Nb}_{\text{Nb}}^{4+}$, and the hole polaron $\text{O}^- - \text{V}_{\text{Li}}$. It should be noted that electrons bound to $\text{Fe}_{\text{Li}}^{3+}$ [1, 13] or $\text{T}_{\text{Li}/\text{Nb}}^{4+}$ [14, 15] may also be described in the framework of the strong-coupling-polaron picture. Luminescent STEs in LN are bound electron-hole pairs with strong coupling to Nb^{5+} and O^{2-} within a single niobium-oxygen octahedron and reveal different optical properties depending whether the STEs form in stoichiometric materials or in niobium-oxygen octahedra near defect sites [16, 17]. Small polarons can be accessed by transient absorption spectroscopy (TAS) due to their characteristic, broad-band absorption features (for a rough overview of the absorption cross sections of the different polaron species see [18]), whereas time-resolved photoluminescence (TRPL) is applied for STEs, showing broad-band luminescence in the blue-green spectral range (see [11, 16, 19–23]).

To this date, carrier self-trapping and recombination in LN, i.e. polaron formation and decay, is described by microscopic models restricted to certain temperature ranges, stoichiometries and dopings of the particular study [16, 24–27], and appear consistent on their own, i.e. within the framework of given experimental boundary conditions and/or within the focus of a specific physical question. The restrictions of these models naturally contradict to the demand of a comprehensive microscopic model for pulse-induced transient absorption (TA) and luminescence in LN as reflected in detail by the following striking examples of our previous studies: (i) room temperature (RT) TA measurements of Conradi *et al* [24] in LN doped with Mg above the optical damage resistance threshold (ODRT) showed that neither a slow decay component at $\lambda = 488$ nm nor the spectral form of the TA-signal can be explained by absorption features of hole and free polarons alone. (ii) Comparing the results of Herth *et al* [25] and Berben *et al* [26] who investigated the TA in Fe:LN in the blue-green spectral range and at $\lambda = 785$ nm, respectively, several inconsistencies regarding the stretching-factor β obtained by fitting a Kohlrausch–Williams–Watts function (KWW) to the data can be found. For $\text{Fe}_{\text{Li}}^{2+}$ polarons absorbing in the blue-green, Herth *et al* reveal β values between 0.55 – 1, depending on the wavelength whereas Berben *et al* published $\beta \approx 0.35$ at 785 nm for the decay of bound polarons under similar experimental conditions. This is in contrast with the claim of Herth *et al*, according to which the decrease of the near-infrared signal is due to a direct transition from $\text{Nb}_{\text{Li}}^{4+}$ bound polarons to $\text{Fe}_{\text{Li}}^{3+}$. In this case, the increasing numbers of $\text{Fe}_{\text{Li}}^{2+}$ polarons should be described by the same τ and β values as obtained from the bound polaron decay function.

Studies of STEs in LN, generated also by band-to-band excitation, refer to (TR)PL measurements [19, 21, 22], usually carried out at temperatures below 100 K. At elevated temperatures, in particular at RT, the luminescence signal becomes weak so that STEs have been disregarded in small polaron dynamics, so far. Using intense laser pulses and considering the complex formation paths in the temporal regime from electron-hole-pair generation up to small polaron formation [4], a considerable number density of STEs and their contribution to the transients can per se not be neglected. Only

recently, Reichenbach *et al* showed that photoluminescence (PL) of unknown microscopic origin can be raised in LN by femtosecond pulse illumination at RT [28, 29].

Thus—despite the presence of a sound knowledge on the formation, transport and recombination of small polarons as well as on the luminescence properties of STEs—we need to accept that nearly nothing is known about the possible interplay of STEs with small polarons in LN in different temperature ranges. This interplay may occur at different stages during the various lifetimes of the individual quasi-particles. For instance small polaron and STE formation may be highly competitive in the ultrafast time range upon hot carrier excitation. On longer timescales, transformations of small polaron pairs to STEs may be discussed and may be decisive to explain the variety of optical phenomena being unexplained in TA experiments, so far.

The intention of this work is to fill this gap in knowledge by inspection of the possible role of self-trapped excitons in the polaronic recombination processes in LN in its very details. This topic inherently comprises a large degree of complexity: two different experimental techniques (TAS and PL) have to be applied, and the studies need to be performed with LN crystals with different doping below and above the photorefractive concentration threshold, over a large temperature range from about 15 K up to RT and on timescales up to minutes upon an incident pump event. Furthermore, it is challenging to uncover an appropriate experimental fingerprint to identify STEs within the polaronic recombination process. We address this complex task by stepwise answering the most obvious and driving questions, at first: (i) *are STEs at the origin of PL in LN up to room temperature?*, (ii) *is there a justified need for a revision of the microscopic polaronic recombination processes?*, and (iii) *is there any experimental fingerprint pointing to a role of STEs in the polaronic recombination process?* After (positively) answering these questions, we become able to focus our discussion on the development of a comprehensive picture for polaronic recombination including STEs and, finally, to tackle the revision of the existing microscopic model.

The paper is organized according to this concept: we first present steady state PL data over a large temperature range uncovering STEs as the microscopic origin of PL at RT (see question (i)). Then, TA data of Fe- and Mg-doped lithium niobate samples, again obtained over a large temperature and an extended wavelength range, indicate, beyond experimental uncertainty, that the dynamics of TA in the red/near-infrared ($\lambda = 633$ nm or 1310 nm, $\lambda = 785$ nm), and the blue ($\lambda = 445$ nm, $\lambda = 488$ nm) spectral range cannot be correlated with each other for a number of experimental conditions in the framework of the current model proposed by Herth *et al* (see question (ii)). Finally TRPL and TA data in Mg:LN are presented and compared over a large temperature range demonstrating some distinct properties of the stretching factor β of STEs deviating from the ones of small polarons, which is used to identify STE-related phenomena in the transient blue absorption in Fe:LN (see question (iii)). Based on these results, we discuss that STEs, and mainly *pinned* STEs (STEs bound to a defect), shall be considered in polaronic recombination.

We present a revised comprehensive microscopic model, being an extension of the original Herth model [25]. It is capable to explain all inconsistencies in TA and TRPL measurements discussed, so far.

2. Experimental methods

Three experimental techniques were used in this study.

- (i) **PL:** Photoluminescence spectra under fs-exposure (regeneratively amplified Ti:Sapphire laser, $\tau_{\text{FWHM}} = 35$ fs, repetition rate 1 kHz; Coherent Inc., type *Astrella*) were obtained using a spectrograph with an air-cooled back-illuminated CCD-camera (Roper Scientific, type *Isoplane* and *PIXIS-UV*). The frequency doubled pump beam ($\lambda = 400$ nm) with an energy of 40 μJ per pulse was slightly focused into the sample and the luminescent emission was collected over the duration of a whole second (averaging over 1000 pump events).
- (ii) **TAS:** Transient absorption spectroscopy using a Q-switched, frequency doubled Nd:YAG pulse laser (Innolas, type *Spitlight 600*) at a center wavelength of $\lambda = 532$ nm (ordinary light polarization) with a pulse duration of $\tau_{\text{FWHM}} = 8$ ns and a maximum pulse energy of $E_{\text{max}} \approx 290$ mJ. Pulse-induced changes of the absorption were detected by the dynamic transmission loss of continuous-wave probe lasers at wavelengths: $\lambda = 445$ nm, 488 nm, 785 nm, and 633 nm or 1310 nm (ordinary light polarization) via Si-PIN photodiodes and a fast digital storage oscilloscope (LeCroy, type *Waverunner LT584*). The recording took place in a time range from 30 ns after excitation up to the complete recovery of the sample (up to several tens of seconds). As shown by comparisons with as-grown crystals, effects of permanent photorefractive damage can be neglected for the given pulse parameters.
- (iii) **TRPL:** Time-resolved photoluminescence measurements were performed utilizing the above mentioned ns-pulse laser, but now in the frequency tripled configuration with a center wavelength of $\lambda = 355$ nm ($E_{\text{max}} \approx 120$ mJ, extraordinary polarization). A combination of a monochromator and a photon counter with a time resolution of 250 ns was used to detect the emitted luminescence in a direction perpendicularly to the pump pulse propagation. In both setups, the measurement was triggered by a diode detecting the scattered pump light and in the case of TRPL the signal to noise ratio was improved by averaging over a total of 1000 shots.

In all setups, the sample temperature could be tuned in the range from 15 K to 400 K using a closed-cycle cryostat with optical windows.

Samples: Polished plates of thickness 1 mm of congruent lithium niobate, with the *c*-axis in the plane, with dopant concentrations of 0.1 mol% Fe or 6.5 mol% Mg in the melt were prepared by Czochralski growth at the University of Padova, and the WIGNER Research Centre for Physics Budapest by

the high-temperature top-seeded solution growth method, respectively.

3. Are STE's at the origin of photoluminescence in LN up to room temperature?

The first question to be experimentally answered is whether STEs can be identified unambiguously at the origin of PL up to RT. The anchor for addressing this question is the low temperature luminescence spectrum that already has been attributed to the radiative decay of STEs, i.e. of electron-hole-pairs localized in a Nb-O-octahedron. By temperature-dependent measurements of the steady state PL signal in the temperature range from 15–300 K, we intend to gradually track the evolution of peak position and width of emission as the temperature changes. The results then allow for a clear assignment of the emission to STEs in the entire range. We note that the measurement series is performed with over-threshold Mg:LN (6.5 mol% Mg in the melt) where luminescence can be observed also at elevated temperatures.

Figure 1(a) shows the spectral fingerprints of the PL of Mg:LN in the temperature range from 15 K to 300 K for the particular case of an exposure to a train of fs-laser pulses with a center wavelength of 400 nm. The spectra, all normalized to their respective peak maxima, feature at 15 K a spectral width of ≈ 0.6 eV (FWHM) at a peak position of 2.82 eV. For the first time, clear evidence for a red-shift of the peak maximum by a total of about 0.2 eV upon heating to RT (see figure 1(b)), together with a spectral broadening to a bandwidth of ≈ 0.95 eV (see figure 1(c)), is found. It should be noted that the total PL intensity decreases by several orders of magnitude at elevated temperatures.

The data are in good agreement with low temperature data published in the literature [16, 19–21], where the PL signal was mostly assigned to the recombination of STEs, and additionally confirm the results of Reichenbach *et al* [28, 29] about RT emission in Mg:LN. Up to $T \approx 200$ K the gradual shift of the luminescence peak maximum corresponds to the Varshni equation [30] expected for luminescence also in semiconductors [31], and can be understood, together with the observed broadening as the impact of phonon coupling on the electron-hole pairs bound in the STE [32]. At higher temperatures the flattening of the peak maximum's temperature dependence, accompanied by a decreased broadening rate, may indicate the gradual appearance of a second, weak, slightly blue-shifted luminescence signal reported by Kämpfe *et al* [19]. The authors attributed it to a recombination process similar to the one at low temperatures, only involving trapping centers at larger distances with respect to the formation area.

It is thus very reasonable to conclude, that (i) up to RT the PL signal must be assigned to the radiative decay of optically generated STEs, and (ii) STEs have to be present within the entire temperature range. The assignment of the luminescence to STEs generated at early stages of pumping is strongly supported by TAS results indicating much slower transport

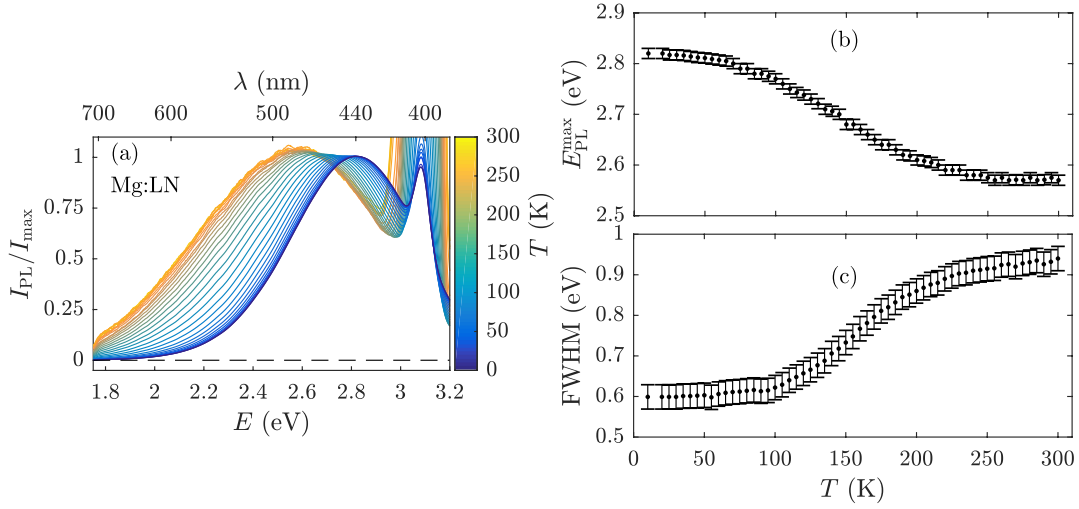


Figure 1. (a) Normalized temperature-dependent emission spectra of Mg:LN following exposure to a fs pump pulse at 400 nm. (b) Emission maximum and (c) full width at half maximum (FWHM) of the emitted luminescence as a function of temperature. A red-shift and a spectral broadening with increasing temperature can be observed.

processes for charged electron polarons (up to minutes), compared to PL dynamics, both to be presented and discussed in the forthcoming sections.

4. Is there a justified need for a revision of the microscopic polaronic recombination processes?

Previous experimental studies on polaronic recombination by means of TA already revealed a few inconsistencies in the microscopic models for polaronic recombination that could not be resolved satisfactorily, so far. In particular, inconsistencies were uncovered if the experimental boundary conditions, such as doping concentration or wavelength of inspection were changed significantly (examples are given in the introduction). We here address the question, whether it is possible to clearly demonstrate the failure of the established models under certain experimental conditions. For this purpose, we use the temperature as main tuning parameter, but also extend the spectral range of optical inspection to the ultraviolet-blue spectral range. A particular feature of the previous microscopic models, a relaxation of electrons from $\text{Nb}_{\text{Li}}^{4+}$ to $\text{Fe}_{\text{Li}}^{3+}$, can specifically be inspected in the ultraviolet spectral range. Our results are finally capable to highlight the model failure by severe differences in the relaxation and rise times of the number densities of $\text{Nb}_{\text{Li}}^{4+}$ and $\text{Fe}_{\text{Li}}^{3+}$, respectively, at temperatures below RT. The studies are performed (a) with Fe:LN (0.1 mol% Fe in the melt) in order to connect and compare our findings with the literature data, and (b) with over-threshold Mg:LN in order to foster the presence of STEs, but also to exclude that our findings may mainly be related to the presence of Fe_{Li} .

4.1. Transient absorption experiments in Fe-doped lithium niobate

In figure 2(a), measurements of the transient absorption on the Fe:LN sample are shown at $T = 293$ K at the probing wavelengths 445 nm, 488 nm, 633 nm, and 785 nm. The first two are monitoring the nearly coinciding $\text{Fe}_{\text{Li}}^{2+}$ and trapped hole absorption bands and the last one roughly corresponding to the maximum of the $\text{Nb}_{\text{Li}}^{4+}$ band, all being strongly overlapping broad asymmetric features characteristic for polarons [18]. Following the incident pump pulse at $t = 0$ s, a transient absorption appears in the near-infrared spectral range and vanishes almost completely in the microsecond range at RT. In the blue spectral range (445 nm and 488 nm), the transient absorption increases on a time scale up to several microseconds and vanishes to zero only after a few seconds.

In comparison, at $T = 198$ K (figure 2(b)), the TA signals show clearly decelerated decay dynamics affecting much stronger the blue than the red spectral range, the maximum for 445 nm and 488 nm being preceded by an almost flat stage up to the millisecond time regime. The blue absorption signal vanishes to zero only after a duration of tens of seconds. This behavior suggests a pronounced time delay between the decaying red and increasing blue transients and can, in fact, be observed for various reduction and oxidation pre-treatments, i.e. for differently adjusted $[\text{Fe}^{2+}]/[\text{Fe}^{3+}]$ ratios between 0.01 and 0.19.

Previously, Berben *et al* [26] and Herth *et al* [25] reported that a sum of stretched-exponential functions (Kohlrausch-Williams-Watts function, KWW)

$$\alpha_{\text{li}}(t, \lambda, T) = \sum_{i=1}^N \alpha_{\text{li},i}^0(\lambda, T) \cdot \exp \left[- \left(\frac{t}{\tau_i(\lambda, T)} \right)^{\beta_i(\lambda, T)} \right], \quad (1)$$

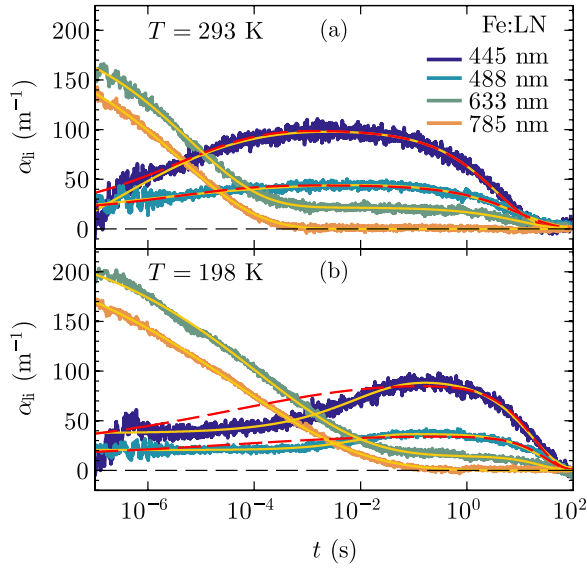


Figure 2. Temporal development of the transient absorption in Fe:LN at (a) $T = 293$ K and (b) 198 K ($I_p \approx 133$ MW cm $^{-2}$). The continuous yellow and dashed red lines represent fits of equation (1) to the data set. A two-term KWW-function ($N = 2$) was used at wavelengths 445 nm, 488 nm, and 633 nm, whereas a one-term function ($N = 1$) for $\lambda = 785$ nm. In the case of the continuous lines $\alpha_{ii}^0(\lambda, T)$, $\tau_i(\lambda, T)$, and $\beta_i(\lambda, T)$ were chosen as free parameters in the fitting procedure, whereas in the case of the dashed red lines the fixed values $\tau_1(785 \text{ nm}, T)$ and $\beta_1(785 \text{ nm}, T)$ obtained in the red region were also used in the blue spectral range. The results are summarized in table 1.

is a reasonable ansatz for the description of the temporal behavior of the transient absorption in Fe:LN. Accordingly, equation (1) has been fitted to the entire experimental data set as represented in figure 2 by the continuous yellow lines. For the absorption at 785 nm a single KWW-function is used to describe the data ($N = 1$), while $N = 2$ is chosen for all other wavelengths. The obtained values of the fitting parameters providing a fair description of the results are presented in table 1 for both temperatures and all four probe wavelengths. The mean relaxation and build-up times for the various components defined by

$$\begin{aligned} \langle \tau_i(\lambda, T) \rangle &= \int_0^\infty \exp \left[- (t/\tau_i(\lambda, T))^{\beta_i(\lambda, T)} \right] dt \\ &= \tau_i(\lambda, T) \Gamma \left(\frac{1}{\beta_i(\lambda, T)} + 1 \right) \end{aligned} \quad (2)$$

are also included in table 1. Here, Γ denotes the gamma function. It should be noted that the error intervals for $\langle \tau_i(\lambda, T) \rangle$ can be close to the order of the calculated value itself due to the combined error of β and τ . Still, the activation energies given in section 5 can be estimated very well, as we deal with different orders of magnitude of the decay time $\langle \tau_i(\lambda, T) \rangle$ at different temperatures. Furthermore, a large number of separate measurements over a broad temperature range is available.

At RT, all transients seem to be in accordance with the model proposed by Herth *et al* [25]. In the red spectral range,

the initial absorption change α_{ii}^0 is attributed to the formation of $\text{Nb}_{\text{Li}}^{4+}$ bound electron polarons excited either from the valence band or $\text{Fe}_{\text{Li}}^{2+}$ to the conduction band by a two-photon or one-photon process, respectively. The initial absorption change in the blue spectral range can be assumed to originate from various sources. There is a negative contribution, i.e. induced transparency due to the transformation of the $\text{Fe}_{\text{Li}}^{2+}$ (part or all) into non-absorbing $\text{Fe}_{\text{Li}}^{3+}$ centers [1, 18]. A positive contribution comes from valence band holes trapped next to Li vacancies as $\text{O}^- - \text{V}_{\text{Li}}$ hole polarons together with a much smaller positive contribution coming from the overlapping absorption tail of the $\text{Nb}_{\text{Li}}^{4+}$ bound electron polarons formed during the parallel electron trapping event.

According to the Herth model, the hopping motion of electron polarons may lead to the formation of stable or intermediate $\text{Fe}_{\text{Li}}^{2+}$ centers, resulting in the decrease of red absorption and to the simultaneous appearance of the rising component in the blue on the microsecond timescale, which is in agreement with the coincidence of the values τ_1 , β_1 and $\langle \tau_1 \rangle$ measured at RT for different wavelengths simultaneously. Some of the $\text{Fe}_{\text{Li}}^{2+}$ centers might be metastable (e.g. due to their specific charge compensation), whereby electron trapping and release at such iron centers could occur repeatedly while electrons recombine with all available pump-induced trapped-hole centers; this process could lead to a decrease of the blue absorption of both trapped holes and metastable $\text{Fe}_{\text{Li}}^{2+}$ centers, contributing to some (rather) long TA component. This model neglects the formation of $\text{Nb}_{\text{Li}}^{4+}$ electron polarons between possible repeated trapping events on iron which can be justified by $\text{Nb}_{\text{Li}}^{4+}$ lifetimes shorter by several orders of magnitude than those of metastable $\text{Fe}_{\text{Li}}^{2+}$ centers (a similar argument explains the neglect of $\text{Nb}_{\text{Nb}}^{4+}$ free polarons compared to $\text{Nb}_{\text{Li}}^{4+}$ bound ones at faster stages).

In contrast, cooling the sample by ≈ 100 K (figure 2(b)) results in clear changes that are no longer consistent with Herth's model assuming the same τ_1 and β_1 for all probe wavelengths. In particular significant deviations appear in the first few milliseconds in this low temperature regime (dashed red lines in figure 2). The non-zero blue absorption remains remarkably constant during most of the $\text{Nb}_{\text{Li}}^{4+}$ decay, prior to its rise to an interim maximum value. Adopting for $\tau_1(445/488 \text{ nm}, 198 \text{ K})$ and $\beta_1(445/488 \text{ nm}, 198 \text{ K})$ the values $\tau_1(785 \text{ nm}, 198 \text{ K})$ and $\beta_1(785 \text{ nm}, 198 \text{ K})$ obtained at 785 nm as fixed parameters, i.e. applying the Herth model, the data set cannot be reconstructed by a converging fit. The only way to reach a very good fit quality is by treating the τ_1 and β_1 parameters at various wavelengths as independent free parameters in the fitting procedures (see yellow lines in figure 2). The decay time in the near-infrared and the rise time in the blue deviate by a factor of 100 and only the mean relaxation/build-up times $\langle \tau_1(\lambda, 198 \text{ K}) \rangle$ have approximately the same values. The bound polarons thus seem to disappear without having recombined simultaneously with holes or having promptly filled $\text{Fe}_{\text{Li}}^{3+/2+}$ traps, and reappear only later as $\text{Fe}_{\text{Li}}^{2+}$

Table 1. Parameters of the KWW-function used to describe the TA of the 0.1 mol% Fe:LN sample at $T = 293$ K and 198 K exemplarily for the data set depicted in figure 2.

293 K				
	445 nm	488 nm	633 nm	785 nm
$\alpha_{ii,1}^0$ (m^{-1})	-72 ± 10	-25 ± 5	184 ± 10	191 ± 10
τ_1 (μs)	5 ± 3	2 ± 1	6 ± 2	4 ± 2
β_1	0.39 ± 0.04	0.30 ± 0.03	0.32 ± 0.03	0.29 ± 0.03
$\langle \tau_1 \rangle$ (μs)	18 ± 16	19 ± 17	42 ± 30	43 ± 42
$\alpha_{ii,2}^0$ (m^{-1})	99 ± 10	41 ± 5	21 ± 5	—
τ_2 (s)	4 ± 2	7 ± 4	9 ± 4	—
β_2	0.61 ± 0.06	0.64 ± 0.06	0.62 ± 0.06	—
$\langle \tau_2 \rangle$ (s)	5.9 ± 3.0	9.7 ± 6.0	13 ± 6.5	—
198 K				
	445 nm	488 nm	633 nm	785 nm
$\alpha_{ii,1}^0$ (m^{-1})	-41 ± 10	-16 ± 5	227 ± 10	238 ± 10
τ_1 (μs)	$(20 \pm 10) \cdot 10^3$	$(9 \pm 4) \cdot 10^3$	121 ± 30	40 ± 10
β_1	0.52 ± 0.05	0.69 ± 0.07	0.22 ± 0.02	0.18 ± 0.01
$\langle \tau_1 \rangle$ (μs)	$(37 \pm 3) \cdot 10^3$	$(12 \pm 6) \cdot 10^3$	$(68 \pm 62) \cdot 10^3$	$(13 \pm 10) \cdot 10^3$
$\alpha_{ii,2}^0$ (m^{-1})	82 ± 10	37 ± 5	14 ± 5	—
τ_2 (s)	20 ± 10	26 ± 10	25 ± 10	—
β_2	0.9 ± 0.1	0.9 ± 0.1	0.8 ± 0.08	—
$\langle \tau_2 \rangle$ (s)	21 ± 11	27 ± 11	28 ± 15	—

centers. This trend is already indicated for temperatures below ≈ 250 K.

The considerable displacement of the TA signal towards longer times and its changed shape at low temperatures have to be described by strongly increased τ_1 and β_1 values in the blue ($\lambda = 445/488$ nm) compared to a moderately rising τ_1 and decreasing β_1 in the red region. The increased stretching factor $\beta_1(488 \text{ nm}, 198 \text{ K}) = 0.69$ in the blue has to be contrasted with its decreased value $\beta_1(785 \text{ nm}, 198 \text{ K}) = 0.18$ in the red (table 1). The slow decreasing component shows an even larger β value in the blue: $\beta_2(445/488 \text{ nm}, 198 \text{ K}) = 0.9$. The weakly defined mean values $\langle \tau \rangle$ show much less variation which is also due to the fact that different combinations of τ and β can, by coincidence, lead to the same value of $\langle \tau \rangle$.

Taking into account the widely accepted interpretation of β [33–35] including the attempt of Merschjann *et al* [36] to relate τ and β directly to characteristic parameters of the hopping transport (time of a single hopping event, number of hopping events, etc), means that the blue transients have a much weaker dependence on hopping history before annihilation than the respective transients in the red. While the electron polaron decay for lower temperatures is increasingly characterized by slow hopping, the blue transients become nearly mono-exponential.

These data point to a clear failure of the Herth model and support the previous reports on inconsistencies in Fe:LN crystals under rather different conditions. In particular at low temperatures and with probing wavelengths in the blue and near-infrared spectrum, we are faced by two striking experimental observations: (i) the decay of bound polaron absorption in the near-infrared is not correlated with the increase of

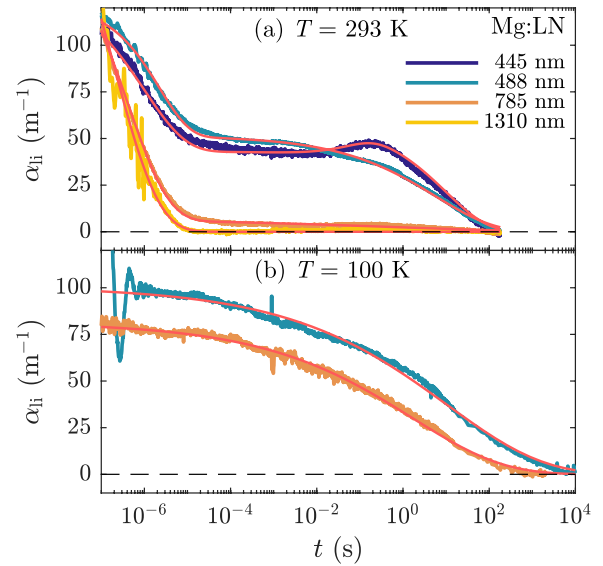


Figure 3. Temporal development of the light-induced absorption in Mg:LN at (a) $T = 293$ K and (b) $T = 100$ K for a pump pulse intensity of $I_p \approx 130 \text{ MW cm}^{-2}$. The red lines represent fits of equation (1) to the experimental data. Fitting results are summarized in table 2.

the $\text{Fe}_{\text{Li}}^{2+}$ absorption anymore, and (ii) there is a strong discrepancy of the determined β value with the state-of-the-art knowledge for small, strong-coupling polaron dynamics in LN [26, 35, 37] to be further discussed in section 5. At the same time, these data are not sufficient to conclude a general failure of the Herth model, i.e. that Herths' model also fails for

Table 2. Parameters of the KWW-function used to describe the TA of the 6.5 mol% Mg:LN sample at $T = 293$ K and $T = 100$ K (figure 3).

	293 K				100 K	
	445 nm	488 nm	785 nm	1310 nm	488 nm	785 nm
$\alpha_{ii,1a}^0$ (m^{-1})	90 ± 10	71 ± 10	177 ± 10	248 ± 20	100 ± 5	81 ± 10
τ_{1a} (μs)	1.0 ± 0.2	2.3 ± 0.5	0.4 ± 0.1	0.2 ± 0.1	$(10 \pm 5) \cdot 10^6$	$(1.7 \pm 1) \cdot 10^6$
β_{1a}	0.45 ± 0.1	0.62 ± 0.1	0.44 ± 0.1	0.45 ± 0.1	0.19 ± 0.01	0.19 ± 0.01
$\langle \tau_{1a} \rangle$ (μs)	2.5 ± 1.5	3.3 ± 1.1	1.0 ± 0.6	0.5 ± 0.3	$(1890 \pm 1200) \cdot 10^6$	$(321 \pm 200) \cdot 10^6$
$\alpha_{ii,1b}^0$ (m^{-1})	-15 ± 5	—	—	—	—	—
τ_{1b} (ms)	70 ± 20	—	—	—	—	—
β_{1b}	0.8 ± 0.2	—	—	—	—	—
$\langle \tau_{1b} \rangle$ (ms)	79 ± 40	—	—	—	—	—
$\alpha_{ii,2}^0$ (m^{-1})	58 ± 10	51 ± 5	6 ± 2	—	—	—
τ_2 (s)	10 ± 3	6 ± 2	5 ± 3	—	—	—
β_2	0.45 ± 0.05	0.32 ± 0.04	0.25 ± 0.1	—	—	—
$\langle \tau_2 \rangle$ (s)	25 ± 10	42 ± 24	120 ± 110	—	—	—

the description of TA in LN crystals of different stoichiometry and/or with/without different dopants (including non-photorefractive defect centers). In what follows, we intend to exclude that the failure is solely related to the dominating existence of $Fe_{Li}^{2+/3+}$ by means of equivalent TAS studies with over-threshold Mg:LN.

4.2. Transient absorption experiments in Mg-doped lithium niobate

The dynamics of the transient absorption in Mg:LN at 445 nm, 488 nm, 785 nm, and 1310 nm at RT (the latter approximately centered on the broad absorption band of Nb_{Nb}^{4+} free polarons) is depicted in figure 3, showing, in addition to a fast decreasing transient on the same time scale for all wavelengths, a long-lived transient blue absorption as previously reported by Conradi *et al* [24]. However, in comparison to former studies a new probe at 445 nm was applied and we were able to observe an unexpected feature, i.e. a clear increase in the absorption at surprisingly long timescales. The newly measured transient local maximum for 445 nm is observed after a significant period (few milliseconds) of constant absorption that resembles the dominant feature of the low-temperature TA dynamics of Fe:LN. This corresponds to a small rising component (denoted by the index 1b) with a time constant $\tau_{1b}(445 \text{ nm}, 293 \text{ K}) = (70 \pm 20) \text{ ms}$. The fitting parameters derived for all KWW components in Mg:LN are summarized in table 2, essentially coinciding at RT with those reported in [24]. The fast component on the microsecond timescale (denoted by the index 1a) is decreasing in the blue region at variance from the case of Fe:LN. The slow component extends to hundreds of seconds in the visible and is absent in the infrared as in Fe:LN.

The dynamics in Mg:LN at RT should be compared to scenarios in Fe:LN taking into account the changed defect structure of Mg:LN: (i) Nb_{Li} antisites and most Fe_{Li} centers are missing as indicated by the vanishing photorefractive effect

in over-threshold crystals [38], (ii) a portion of Mg^{2+} dopant ions and some of the background Fe impurities on the ppm level are incorporated on Nb sites [39, 40], where their charge state remains fixed.

The lack of Nb_{Li} antisites results in an increase of the electron polaron hopping frequency, now occurring in the regular Nb sublattice, leading to a shortening of τ_1 by nearly an order of magnitude, compared to Fe:LN, so that $\tau_1(785/1310 \text{ nm}, RT) \approx 0.3 \mu s$. Accordingly, there are even longer delays (compared to Fe:LN) between this fast decay of free polarons and the slower components in the blue. Due to the small number of Fe_{Li}^{2+} centers, a significant influence on the TA can be excluded as supported also by the monotonous decrease of the 488 nm TA signal in the entire observed temporal region. Only the small rising component τ_{1b} at 445 nm extending into the 70 ms range has to be attributed to background Fe impurities, based on the analogy with component τ_1 in Fe:LN. The fast blue TA component in Mg:LN, temporarily locked with polaron decay monitored in the near-infrared, can be attributed to a direct process of polaron recombination with trapped-hole centers. For $T < 100$ K, TA signals in Mg:LN extend to several minutes both in the near-infrared and the blue region due to the slow hopping of polarons and delays in the recombination processes. Therefore, the three KWW-components in the blue spectral range cannot be satisfactorily distinguished anymore due to similar decay times of several overlapping TA components. A single-component fit at $T = 100$ K and $\lambda = 488$ nm yields $\tau \approx 10$ s and $\beta \approx 0.19$, and therefore $\langle \tau \rangle \approx 1.9 \cdot 10^3$ s. The latter is much longer in comparison to the value determined in the near-infrared, thus indicating the presence of the RT processes at low temperatures, as well. The values obtained for 785 nm and 488 nm are summarized in table 2.

Apart from the latter process, the RT TA-data in Mg:LN thus clearly resemble the findings in Fe:LN, and further stress the failure of the original microscopic model for polaronic recombination. Similarly to the case of Fe:LN the model cannot be

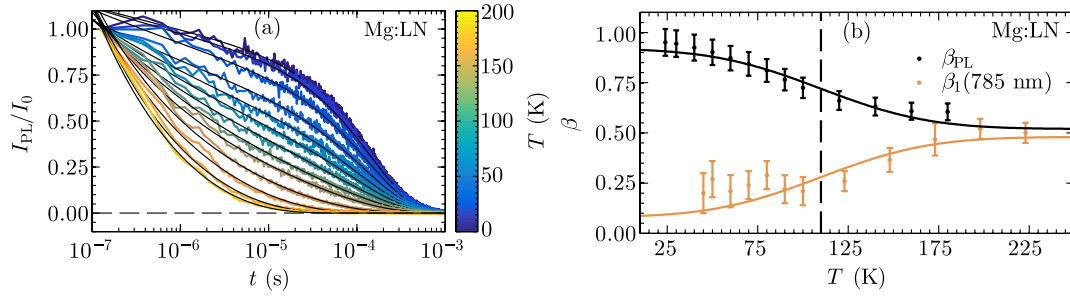


Figure 4. (a) Temporal decay of the PL intensity at 460 nm Mg:LN following exposure to a single ns laser pulse for temperatures given by the color code. The signal is normalized to the value determined at $t = 10^{-7}$ s; the black lines represent fits to the experimental data using equation (3). (b) Temperature dependence of the stretching-factors: β_{PL} (black) obtained from fitting equation (3) to the luminescence decay data and β_1 (785 nm) (orange) obtained from fitting equation (1) to TA results in Mg:LN. The solid lines are phenomenological descriptions of the $\beta(T)$ behavior with an error-function. The dashed line represents a common inflection point at $T_{\beta}^{\text{Mg}} = (110 \pm 10)$ K.

corrected by simply considering some process of more complex type but involving only single-electron transfers. Instead, a more complex electronic center, the STE, having clear fingerprints for its identification, will be discussed in more detail below.

5. Is there any experimental fingerprint pointing to a role of STE's in the polaronic recombination process?

The PL spectra presented in section 3 clearly indicate the presence of STEs over the temperature range 15–300 K suggesting that STEs should not be neglected in non-radiative recombination processes either. In order to find the various transient manifestations of STEs, in this section temperature-dependent TRPL measurements are presented and combined with corresponding TA results. The temperature dependence of the stretching coefficient $\beta(T)$ will be shown to be an unambiguous fingerprint for a clear separation between STE-related phenomena on the one hand and processes determined by the hopping of electron polarons on the other hand. This distinction is also supported by the different Arrhenius-type activation energies obtained from the respective time constants. First we use Mg:LN in order to benefit from the comparison with the characteristic blue PL feature, then turn to the peculiarities offered by Fe:LN.

5.1. Stretching-factors and activation energies in the photoluminescence and transient absorption of Mg:LN

Figure 4(a) shows the TRPL of Mg:LN upon ns-pulse exposure at 355 nm ($I_p \approx 100 \text{ GW m}^{-2}$, extraordinary polarization) for the emission wavelength of 460 nm for a series of temperatures in the broad range from 15 K to 200 K in a semi-logarithmic plot. For comparison, all data have been normalized to the maximum luminescence signal at $t = 10^{-7}$ s. With increasing temperature the luminescence decay time is found to decrease from the milli- to the microsecond time range as expected from the studies of Powell and Freed, and Fischer *et al* [21, 23]. For a quantitative analysis, and according to Zatryb *et al* [41], the evolution rate of excited emitters has to be considered, so that the first time derivative

of the stretched-exponential KWW function is used for the fitting procedure:

$$I(t, T) = I_0(T) \cdot t^{(\beta_{\text{PL}}(T)-1)} \cdot \exp \left[- \left(\frac{t}{\tau_{\text{PL}}(T)} \right)^{\beta_{\text{PL}}(T)} \right]. \quad (3)$$

As shown by the black lines in figure 4(a), very good correspondence could be achieved between equation (3) and the experimental data using only a single KWW component with two independent fitting parameters, the stretching coefficient $\beta_{\text{PL}}(T)$ and the decay time $\tau_{\text{PL}}(T)$, giving further support to the unambiguous (STE-related) origin of the PL observed. The dependence $\beta_{\text{PL}}(T)$ depicted in figure 4(b) is in full accordance with a trend recently recognized in a smaller temperature interval by Kämpfe *et al* [19]. The change of $\beta_{\text{PL}}(T)$ is very significant and represents a transition from unity for a mono-exponential function at $T \approx 25$ K to the stretched case $\beta_{\text{PL}} \approx 0.6$ at $T \approx 180$ K (see figure 4(b)). The decay time $\tau_{\text{PL}}(T)$ remains nearly constant for temperatures below 100 K with a value of $\tau \approx 10^{-4}$ s whereas an Arrhenius-like behavior with an activation energy $E_A \approx 0.09$ eV is found for $T \gg 100$ K.

We interpret both findings by assuming that at low T the decay time of the luminescence is defined by a localized process where hopping is suppressed leading to a single exponential decay ($\beta_{\text{PL}} = 1$). As the temperature is increased above 100 K, the steep decrease of both τ and the stretching exponent β suggests that a hopping process becomes dominant. To explain the extremely low activation energy for luminescence decay, we assume that hopping of the STE as a whole is involved. In comparison, for free polaron hopping a clearly larger activation energy $E_A \approx 0.26$ eV can be derived from the observed temperature dependence of the mean relaxation time $\langle \tau_1(785 \text{ nm}, T) \rangle$ which also follows an Arrhenius behavior for $T > 100$ K in our Mg:LN sample; practically the same value has been estimated earlier as one fourth of the optical excitation energy ≈ 1 eV of $\text{Nb}_{\text{Nb}}^{4+}$ [12, 42]. Accordingly the temperature dependence of β_{PL} has to be attributed to the hopping of STEs and their subsequent localized recombination.

Comparing $\beta_{\text{PL}}(T)$ with TA measurements of $\beta_1(785 \text{ nm}, T)$ on Mg:LN displaying the behavior expected for polaron hopping (see figure 4(b)), it is immediately clear

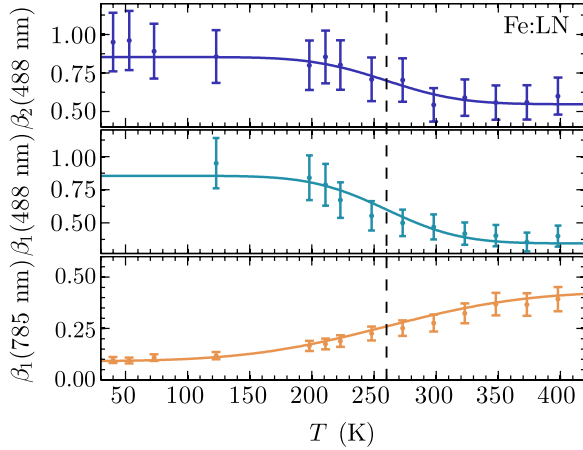


Figure 5. Temperature dependence of the stretching-factors $\beta_1(785 \text{ nm}, T)$, $\beta_1(488 \text{ nm}, T)$, and $\beta_2(488 \text{ nm}, T)$ in Fe:LN. The solid lines are qualitative descriptions of the $\beta(T)$ behavior with an error-function. The dashed line represents a common inflection point at $T_\beta^{\text{Fe}} = (260 \pm 10) \text{ K}$.

that $\beta_{\text{PL}}(T)$ exhibits a reversed temperature dependence. We chose $\lambda = 785 \text{ nm}$ as a probe wavelength where the largest contribution, in the absence of antisites, can be attributed to $\text{Nb}_{\text{Nb}}^{4+}$ free polarons. Both types (TRPL and TA) of temperature behavior in figure 4(b) can be described phenomenologically, e.g. by an error-function with a common inflection point at $T_\beta^{\text{Mg}} = (110 \pm 10) \text{ K}$ indicating the temperature where the processes due to hopping become dominant. Thus, the given reverse type of $\beta_{\text{PL}}(T)$ dependence, can be regarded as a fingerprint of STEs, in contrast to the $\beta(T)$ behavior observed for small electron polarons; this is supported by the fact that the activation energies obtained for luminescence and red/near-infrared absorption decay are different requiring a second hopping entity, STEs. Note, that even though the transients in luminescence and absorption are on different timescales, a comparison between the $\beta(T)$ behaviors may be justified as the stretching-factor is a good indicator for the type of transport and annihilation processes involved.

5.2. Stretching-factors and activation energies in the transient absorption of Fe:LN

In this section detailed temperature-dependent measurements of the red and blue TA on Fe:LN are presented with the goal to uncover similar fingerprints. The obtained behavior of the various stretching-factors $\beta_i(\lambda, T)$ is shown in figure 5. Results in the red and blue spectral range differ in two major points: (i) with decreasing temperatures $\beta_1(T)$ is observed to decrease in the red spectral range, compared to the opposite behavior of both $\beta_1(T)$ and $\beta_2(T)$ in the blue (see figure 5, but also table 1). Both types of temperature behavior in figure 5, again, can be described by an error-function (orange and blue lines in figure 5) where $T_\beta^{\text{Fe}} = (260 \pm 10) \text{ K}$ is discovered as a common inflection point. (ii) At higher temperatures, the mean decay

times $\langle \tau_i(\lambda, T) \rangle$ follow an Arrhenius behavior, however, for temperatures $T < T_\beta^{\text{Fe}}$ the mean decay times in the blue range become nearly temperature-independent. The obtained activation energy $E_A^1(785 \text{ nm}) \approx 0.37 \text{ eV}$ apparently corresponds to polaron hopping in the presence of antisites (to be compared to one fourth of the optical excitation energy $\approx 1.6 \text{ eV}$ of $\text{Nb}_{\text{Li}}^{4+}$ [12]). It should be added that the most recent value of the polaron stabilization energy was determined to $\approx 0.75 \text{ eV}$ [37]. The activation energies derived for the blue region, $E_A^1(488 \text{ nm}) \approx 0.71 \text{ eV}$ and $E_A^2(488 \text{ nm}) \approx 0.78 \text{ eV}$ are correspondingly higher and will be discussed in section 6.

The temperature dependence of the stretching exponents $\beta_1(T)$ and $\beta_2(T)$ in the blue of the TA of Fe:LN (figure 5) qualitatively shows the same fingerprint behavior as $\beta_{\text{PL}}(T)$ obtained from time-resolved luminescence measurements on Mg:LN (figure 4(b)). The similar dynamics of the considered blue transients in emission and absorption strongly suggests their common origin, namely STEs. In Mg:LN the temperature $T_\beta^{\text{Mg}} \approx 110 \text{ K}$ equally characterizes the onset of polaronic and excitonic hopping processes observed in transient absorption and luminescence decay, respectively. In Fe:LN, the $T_\beta^{\text{Fe}} \approx 260 \text{ K}$ value reflects the smaller mobility of the polarons and a parallel change in electron-phonon coupling due to the presence of antisite Nb defects, as compared to Mg:LN where antisites are absent. These findings will be used in the following section to reconsider the microscopic polaronic recombination model in LN.

6. Extension of the microscopic model by STE's and pinned STE's

So far, our analysis was able to answer the most striking questions related to the role of STEs in the polaronic recombination processes in LN. First, it is clearly demonstrated, that the observed, pulse-induced blue-green luminescence in LN can be attributed to the decay of STEs up to RT. Second, the failure of the microscopic model comprising solely small electron and hole polarons is highlighted and evident as soon as the temperature is reduced or the doping is changed. Third, the stretching factors and activation energies are recognized to yield sensitive information on the dynamics of both PL and TA indicating the presence of STEs.

As a result, it becomes necessary to extend the microscopic picture by including the additional electronic states of STEs and STEs pinned on defects, as schematically depicted in figure 6. As a matter of fact, such pinned STEs (i) may be long-lived, (ii) should absorb in the blue spectral range, and (iii) decay preferably non-radiatively and, thus, considerably contribute to the blue TA in LN crystals. We like to note that the alternative consideration of an interim formation of bipolarons, that are strongly absorbing in the blue region (see e.g. [11, 18]), would not explain the delayed appearance of the blue component in Fe:LN. The same holds for Mg:LN due to the lack of antisites. We will thus disregard the presence of bipolarons in our model approach, though it may be included if thermally reduced LN is considered.

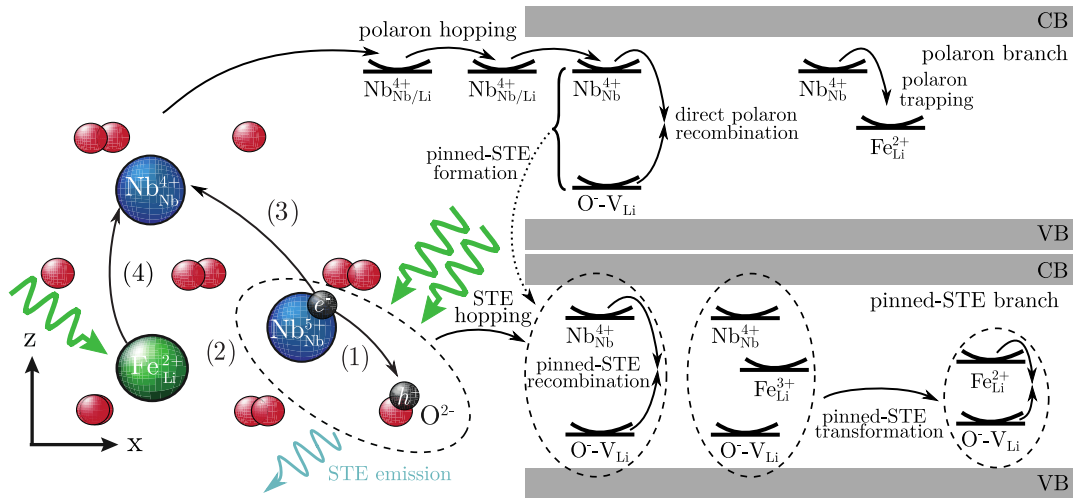


Figure 6. Excitation and recombination model after pulse exposure (green thick arrows) in LN. Hot electron–hole pairs created by the pump pulse in a two-photon process either recombine directly (1), form STEs within NbO_6 octahedra (2), or dissociate to form separate oppositely charged small polarons (3), as a further option, electrons from $\text{Fe}_{\text{Li}}^{2+}$ may be excited to form additional small polarons leaving back $\text{Fe}_{\text{Li}}^{3+}$ (4). The recombination paths are divided into a polaron and an exciton branch, for more detail see text.

As seen on the left-hand side of figure 6, the starting situation can be summarized as follows: immediately (on the ps scale) after the pump pulse, a given concentration of free or bound electron polarons and holes is created, together with a certain amount of emptied $\text{Fe}_{\text{Li}}^{3+}$ traps [4, 42]. Small electron polarons forming the polaron branch (upper right-hand part of figure 6) move through the lattice by thermally activated hopping [43, 44] which terminates in deep traps like $\text{Fe}_{\text{Li}}^{3+}$ converting to $\text{Fe}_{\text{Li}}^{2+}$ or they annihilate with trapped holes. However, depending on conditions of temperature and composition, a considerable concentration of STEs, disregarded in earlier TA studies, may be present as well, as indicated by luminescence. Since this radiative recombination is observed to be orders of magnitude faster than the small polaron decay time measured by TA (see our measurements), we can assume that it stems from STEs formed directly after light exposure forming a second relaxation channel parallel to the polaron recombination. Besides the possibility to recombine radiatively, the STE is the starting point of a pinned-STE branch (lower right-hand part of figure 6) which will be described in more detail in the following.

6.1. (Pinned) STEs in LN

STEs may be assumed to have a significant hopping mobility as confirmed by the presence of a thermally activated process ($E_A \approx 0.09$ eV) of the luminescence decay. At higher temperatures and in defective materials, STEs formed at early stages of pumping are expected to get pinned on defects, similarly to the formation and trapping of single-site small polarons. Resonant excitonic/energy transfer can be discarded due to the large Stokes shifts. In particular, STEs may be captured, among others, by the same defects as free holes (e.g. by lithium vacancies or $\text{Mg}_{\text{Nb}}^{2+}$ defects). The final recombination site should

play a decisive role, especially at lower temperatures, when localization sets in and τ gets nearly temperature-independent. The exact optical properties depend on the presence and type of defects adjacent to the niobium-oxygen octahedron containing the STE as shown by luminescence studies in LN with various stoichiometric compositions [16] including also crystals with ilmenite type cationic stacking order [17]. While the presence of Mg up to the ≈ 5 mol% threshold, i.e. the elimination of antisites, leads to increased emission [21], Fe doping seems to lead to luminescence quenching comparable to the case of Cr doping [23], indicating that both intrinsic defects and Fe form pinning centers for STEs where luminescence is suppressed. Non-radiative decay should be strongly preferred for STEs pinned on defects with high pinning/stabilizing energies leading to the longer absorption decay times and higher activation energies as observed for TA in the blue. In this case, the decreasing $\beta_{\text{PL}}(T)$ function characterizes the temperature dependent pinning history of the STE influencing its decay. The existence of a second, slow component, with activation energies slightly larger than in our case (0.14 eV and 0.11 eV) valid above somewhat higher temperatures 140 K and 160 K for the respective luminescence components, obtained in 7.5 mol% Mg-doped samples by Kämpfe *et al* [19], may then be attributed to minor deviations from the crystal structure optimal for luminescence. It should be noted that pinned STEs might also be formed as interim states during the recombination of electron polarons with trapped-hole centers.

6.2. Absorption properties of (pinned) STEs

STEs, which have been established in various materials, e.g. alkali halides, beside their capability to decay radiatively, have absorption bands similar to those of small polarons as demonstrated by Williams *et al* [5, 45]. As pointed out by these authors, the hole and electron, which a STE consists

of, can be excited optically and show a near ultraviolet and a near-infrared absorption, respectively, corresponding to optically triggered jumps of the respective constituent to equivalent neighboring sites. In LN, due to the transfer of the hole constituent to an equivalent or non-equivalent neighboring oxygen site, STEs are also expected to have an absorption in the blue/near-ultraviolet region. However, a separate contribution of the radiatively decaying STEs to the TA at the measured wavelengths was not observed even in Mg:LN at low temperatures although the luminescence and TA decay times deviate by a factor of at least 1000 from each other and a TA of such STEs—if present—should have been clearly visible. Furthermore, to the best of our knowledge, evidence for the presence of excitonic infrared/ultraviolet absorption in LN is not reported in literature, so far.

Concerning the absorption properties of pinned STEs, we have no experimental indication for the presence of a near-infrared absorption. The ‘quenching’ of infrared-absorption may be understood by taking into account proposed dynamic or static models of trapped hole O^- centers containing a unique Nb neighbor in a strongly preferred position for electron trapping [46, 47]. In such cases electron hopping may be hampered or requires much higher energy. The blue/ultraviolet absorption of pinned STEs, though present, might be nearly indistinguishable from the absorption of an O^- trapped hole.

6.3. Two-step recombination model of STEs pinned on Fe^{3+} centers

STEs should also be capable to get pinned on iron centers. Most Fe_{Li}^{3+} centers in LN may be assumed to have a nearest neighbor charge-compensating lithium vacancy (V_{Li}) suggesting the following scenario: the constituents of a nearby STE are attracted by the constituents of the $Fe_{Li}^{3+} - V_{Li}$ dipole leading to an STE pinned on $Fe_{Li}^{3+} - V_{Li}$ with the Nb^{4+} and O^- sites at nearest neighbor positions of the Fe_{Li}^{3+} and V_{Li} sites, respectively. A single jump of the electron from Nb_{Nb}^{4+} to the Fe site (along the c axis) transfers the complex into a new state, which is a coupled $Fe_{Li}^{2+} - O(V_{Li})^-$ defect. Both Fe_{Li}^{2+} and the hole constituent absorb in the blue, their aggregate causing a net increase of the total blue TA with respect to the pinned STE absorption, thus providing a rising TA component. However, this new defect state again has a metastable excitonic character and tends to recombine, restoring the original $Fe_{Li}^{3+} - V_{Li}$ defect having no absorption at all. Thus we consider a strongly localized two-step STE recombination process where the electron constituent, starting from a Nb_{Nb}^{4+} state, proceeds to a lower Fe_{Li}^{2+} level before rejoining its O^- partner. Since both the pinned STE and the intermediary $Fe_{Li}^{2+} - O(V_{Li})^-$ complex can be assumed to have metastable ground states with differently relaxed lattice environments, both jumps have to be phonon-induced/assisted, and may involve significant, separate temperature dependent time delays. This two-step STE recombination path, leading to an interim TA maximum with a subsequent steep decay clearly

explains the most conspicuous features of the TA at 445 nm, while it seems to be much less pronounced at 488 nm. As the second jump seems to take significantly longer than the first, a description in terms of two separate KWW-functions has to be a good approximation.

The derived activation energies support the two-step relaxation model of the STE pinned on $Fe_{Li}^{3+} - V_{Li}$ yielding $E_A^1 \approx 0.71$ eV for the first and a larger $E_A^2 \approx 0.78$ eV for the second step, the latter corresponding to the decay of the strongly distorted $Fe_{Li}^{2+} - O(V_{Li})^-$ state, and roughly equaling one fourth of the strong absorption measured at 445 nm (2.79 eV). A similar ratio may hold for the STE pinned on $Fe_{Li}^{3+} - V_{Li}$ in the first step as well, confirming $\propto E_{opt}/4$ as the activation energy characterizing the hopping of a polaron from a given site to an adjacent one [12]. Negligible differences between 488 nm and 445 nm data (τ , β) in Fe:LN indicate small superpositions from other recombination centers not containing Fe.

At low temperatures the proposed two-step relaxation of the STE pinned on $Fe_{Li}^{3+} - V_{Li}$ clearly dominates the 445 nm TA spectrum in Fe:LN for $t > 10$ ms (see figure 2(b)). While these two steps seem to explain both the rising and decreasing 445 nm components in Fe:LN, an important contribution to the long decreasing component in Mg:LN may come from STEs pinned on hole-trap defects like (V_{Li})-pinned STEs. Contributions from such pinned STEs correspond to centers with observed lifetimes in the minute range and have been attributed to O^- -type centers in 5 mol% Mg-doped LN by Xin *et al* [40]. In fact, our probe wavelengths are in the central part of the O^- and on the very wing of a TA band attributed to $O^- (Mg_{Nb}^{2+})$ centers in [40].

Accordingly the first-step lifetime of the ($Fe_{Li}^{3+} - V_{Li}$)-pinned STE state recombination may correspond to the lifetimes of the rising components τ_1 and τ_{1b} observed at 445 nm in Fe:LN at low temperatures and in Mg:LN at RT, respectively. In contrast, much longer second-step lifetime may correspond to τ_2 of the long decreasing component at 445 nm in Fe:LN. The separation of time domains of polaron and pinned-STE decay is rather large in Mg:LN (figure 3). However, there may be a considerable overlap in Fe:LN at RT which resulted in the earlier misinterpretation of the blue TA components discussed above.

7. Summary and conclusion

In this paper the question is answered whether STEs play a role in polaronic recombination processes in LN. In a first step it was shown that STEs can be optically generated in Mg:LN in the whole temperature range from 15–300 K. In particular, our data, collected for the first time continuously up to 300 K, demonstrate that the PL signal can clearly be assigned to similar STEs in the entire temperature range.

In the next step shortcomings of earlier microscopic polaronic recombination models were demonstrated. Transient absorption measurements in an extended temperature and spectral range on Fe:LN and Mg:LN reveal

inconsistencies when Herth's model is applied on these new data sets: (i) the decay of bound polarons absorbing in the near-infrared is not correlated with the increase of blue absorption, (ii) the fact that the β coefficient in the blue spectral range is larger for lower temperatures is in contrast to the state-of-the-art knowledge for small, strong-coupling polaron dynamics in LN.



Third, the temperature-dependent TA was compared with the corresponding TRPL data to check whether features in TA could also be attributed to STEs. The striking increase of the stretching factor β with decreasing temperature attributed to STEs in TRPL, but present also in TA in the blue spectral range, was found to be such a fingerprint. In fact, this is in contrast to the usual $\beta(T)$ behavior which is expected for small polarons in LN.

Based on these results, we propose and discuss for the first time an excitation and recombination model by including a STE branch in addition to the established polaron recombination branch. Both together are capable to describe in a comprehensive model TA and PL over a broad temperature-range. Here, STEs and pinned STEs formed during or immediately after pumping were found to be important transporters of negative charges towards deep Fe^{3+} traps. The presence of long-lived perturbed O^- centers containing an adjacent lithium vacancy in their clusters have to be assumed in both LN systems, while a second distinct group of STE hosts can be attributed to doping (Mg_{Nb} or Fe_{Li}). The varying accessibility of these centers and/or the different stability of the corresponding pinned STEs can be ascribed to different clustering with intrinsic and extrinsic defects, taking into account that clustering not only results in various levels of charge compensation but may also result in different restrictions for polaron and exciton hopping. However, further investigations are required regarding the absorption of the emitting STEs on even shorter timescales and the type of centers at which pinned STEs are formed. We further assume that the concept of both the polaron and (pinned) STE branch in LN could also be transferred to other materials with perovskite structure such as KNbO_3 , LiTaO_3 , etc, since all these materials may host similar kinds of defects. Furthermore, we expect that our approach may also serve as a basis for new models and insights to describe related phenomena such as photocatalysis in TiO_2 , MgO and/or ZnO .

Acknowledgments

The authors are indebted to O F Schirmer and T Nörenberg for fruitful discussions as well as L Kovács and coworkers at the Wigner Research Centre for Physics, Budapest, for crystals and crystal preparation. Financial support from the Deutsche Forschungsgemeinschaft (DFG) via projects IM37/5-2, IM37/11-1, INST 190/137-1 FUGG and INST 190/165-1 FUGG is kindly acknowledged.

ORCID iDs

S Messerschmidt  <https://orcid.org/0000-0001-6193-7487>
M Bazzan  <https://orcid.org/0000-0002-1451-1368>

References

- [1] Schirmer O F, Imlau M and Merschjann C 2011 *Phys. Rev. B* **83** 165106
- [2] He J, Franchini C and Rondinelli J M 2016 *Chem. Mater.* **28** 25
- [3] Lengyel K et al 2015 *Appl. Phys. Rev.* **2** 040601
- [4] Imlau M, Badorreck H and Merschjann C 2015 *Appl. Phys. Rev.* **2** 040606
- [5] Williams R T and Song K S 1990 *J. Phys. Chem. Solids* **51** 679
- [6] Nolan M 2012 *ACS Appl. Mater. Interfaces* **4** 5863
- [7] Migani A and Blancafort L 2016 *J. Am. Chem. Soc.* **138** 16165
- [8] Sezen H et al 2015 *Nat. Commun.* **6** 6901
- [9] Liu Z, Yin Z, Cox C, Bosman M, Qian X, Li N, Zhao H, Du Y, Li J and Nocera D G 2016 *Sci. Adv.* **2** e1501425
- [10] Hamid S B A, Teh S J and Lai C W 2017 *Catalysts* **7** 93
- [11] Schirmer O F, Thiemann O and Wöhlecke M 1991 *J. Phys. Chem. Solids* **52** 185
- [12] Schirmer O F, Imlau M, Merschjann C and Schoke B 2009 *J. Phys.: Condens. Matter* **21** 123201
- [13] Sanson A, Zaltron A, Argiolas N, Sada C, Bazzan M, Schmidt W G and Sanna S 2015 *Phys. Rev. B* **91** 094109
- [14] Juppe S and Schirmer O F 1986 *Phys. Lett. A* **117** 150
- [15] Corradi G, Zaritskii I M, Hofstaetter A, Polgár K and Rakitina L G 1998 *Phys. Rev. B* **58** 8329
- [16] Krol D M, Blasse G and Powell R C 1980 *J. Chem. Phys.* **73** 163
- [17] Wiegel M, Blasse G, Navrotsky A, Mehta A, Kumada N and Kinomura N 1994 *J. Solid State Chem.* **109** 413
- [18] Merschjann C, Schoke B, Conradi D, Imlau M, Corradi G and Polgár K 2008 *J. Phys.: Condens. Matter* **21** 015906
- [19] Kämpfe T, Haußmann A, Eng L M, Reichenbach P, Thiessen A, Woike T and Stuedtner R 2016 *Phys. Rev. B* **93** 174116
- [20] Blasse G 1968 *J. Chem. Phys.* **48** 3108
- [21] Fischer C, Wöhlecke M, Volk T and Rubini N 1993 *Phys. Status Solidi a* **137** 247
- [22] Klose F, Wöhlecke M and Kapphan S 1989 *Ferroelectrics* **92** 181
- [23] Powell R C and Freed E E 1979 *J. Chem. Phys.* **70** 4681
- [24] Conradi D, Merschjann C, Schoke B, Imlau M, Corradi G and Polgár K 2008 *Phys. Status Solidi RRL* **2** 284
- [25] Herth P, Granzow T, Schaniel D, Woike T, Imlau M and Krätzig E 2005 *Phys. Rev. Lett.* **95** 067404
- [26] Berben D, Buse K, Wevering S, Herth P, Imlau M and Woike T 2000 *J. Appl. Phys.* **87** 1034
- [27] Herth P, Schaniel D, Woike T, Granzow T, Imlau M and Krätzig E 2005 *Phys. Rev. B* **71** 125128
- [28] Reichenbach P, Kämpfe T, Thiessen A, Haußmann A, Woike T and Eng L M 2014 *Appl. Phys. Lett.* **105** 122906
- [29] Reichenbach P, Kämpfe T, Thiessen A, Schröder M, Haußmann A, Woike T and Eng L M 2014 *J. Appl. Phys.* **115** 213509
- [30] Varshni Y 1967 *Physica* **34** 149
- [31] Botha J and Leitch A W R 2000 *J. Electron. Mater.* **29** 1362
- [32] Toyozawa Y 2003 *Optical Processes in Solids* (Cambridge: Cambridge University Press)

A Publications

- [33] Klafter J and Shlesinger M F 1986 *Proc. Natl Acad. Sci.* **83** 848
- [34] Sturman B, Podivilov E and Gorkunov M 2003 *Phys. Rev. Lett.* **91** 176602
- [35] Mhaouech I and Guilbert L 2016 *Solid State Sci.* **60** 28
- [36] Merschjann C, Imlau M, Brüning H, Schoke B and Torbrügge S 2011 *Phys. Rev. B* **84** 052302
- [37] Guilbert L, Vittadello L, Bazzan M, Mhaouech I, Messerschmidt S and Imlau M 2018 *J. Phys.: Condens. Matter* **30** 125701
- [38] Volk T and Wöhlecke M 2010 *Lithium Niobate* (New York: Springer)
- [39] Malovichko G I, Grachov V G and Kokanyan E P 1992 *Ferroelectrics* **125** 289
- [40] Xin F, Zhai Z, Wang X, Kong Y, Xu J and Zhang G 2012 *Phys. Rev. B* **86** 165132
- [41] Zatoryb G, Podhorodecki A, Misiewicz J, Cardin J and Gourbilleau F 2011 *Nanoscale Res. Lett.* **6** 106
- [42] Freytag F, Booker P, Corradi G, Messerschmidt S, Krampf A and Imlau M 2018 *Opt. Mater. Express* **8** 1505
- [43] Emin D 1975 *Adv. Phys.* **24** 305
- [44] Emin D 2012 *Polarons* (Cambridge: Cambridge University Press)
- [45] Song K S and Williams R T 1993 *Self-Trapped Excitons* (Berlin: Springer)
- [46] Miki T, Hantehzadeh M R and Halliburton L E 1989 *J. Phys. Chem. Solids* **50** 1003
- [47] Zaritskii I M, Rakitina L G, Corradi G, Polgar K and Bugai A A 1991 *J. Phys.: Condens. Matter* **3** 8457

A.5 Pulse-induced transient blue absorption related with long-lived excitonic states in iron-doped lithium niobate

- Simon Messerschmidt, Bjoern Bourdon, David Brinkmann, Andreas Krampf, Laura Vittadello, and Mirco Imlau

Pulse-induced transient blue absorption related with long-lived excitonic states in iron-doped lithium niobate

Opt. Mater. Express 9, 2748-2760 (2019); doi: 10.1364/OME.9.002748

©2019 Optical Society of America. Users may use, reuse, and build upon the article, or use the article for text or data mining, so long as such uses are for non-commercial purposes and appropriate attribution is maintained. All other rights are reserved.



Pulse-induced transient blue absorption related with long-lived excitonic states in iron-doped lithium niobate

SIMON MESSERSCHMIDT, BJOERN BOURDON, DAVID BRINKMANN, ANDREAS KRAMPF, LAURA VITTADELLO, AND MIRCO IMLAU*

School of Physics, Osnabrueck University, BarbarasträÙe 7, 49076 Osnabrueck, Germany

*mirco.imlau@uni-osnabrueck.de

Abstract: Transient absorption is studied in Fe-doped lithium niobate single crystals with the goal to control and probe a blue absorption feature related with excitonic states bound to Fe_{Li} defect centers. The exciton absorption is deduced from the comparison of ns-pump, supercontinuum-probe spectra obtained in crystals with different Fe-concentration and $\text{Fe}_{\text{Li}}^{2+/3+}$ -ratio, at different pulse peak and photon energies as well as by signal separation taking well-known small polaron absorption bands into account. As a result, a broad-band absorption feature is deduced being characterized by an absorption cross-section of up to $\sigma^{\text{max}}(2.85 \text{ eV}) = (4 \pm 2) \cdot 10^{-22} \text{ m}^2$. The band peaks at about 2.85 eV and can be reconstructed by the sum of two Gaussians centered at 2.2 eV (width $\approx 0.5 \text{ eV}$) and 2.9 eV (width $\approx 0.4 \text{ eV}$), respectively. The appropriate build-up and decay properties strongly depend on the crystals' composition as well as the incident pulse parameters. All findings are comprehensively analyzed and discussed within the model of $\text{Fe}_{\text{Li}}^{2+} - \text{O}^- - \text{V}_{\text{Li}}$ excitonic states.

© 2019 Optical Society of America under the terms of the [OSA Open Access Publishing Agreement](#)

1. Introduction

The microscopic understanding of pulse-induced transient absorption phenomena, such as green-induced infrared absorption (GRIIRA) [1] or blue-induced infrared absorption (BLIIRA) [2], is mandatory for the control of laser-induced damage mechanisms in lithium niobate (LiNbO_3 , LN) and, thus, for applications of LN in nonlinear photonics [3]. From the beginning, the appearance of transient infrared absorption was successfully explained by the coupling of optically generated electrons with phonons, i.e., by the formation of $\text{Nb}_{\text{Nb/Li}}^{4+}$ small, strong-coupling electron polarons [4]. In contrast, the microscopic origin of transient blue-absorption remains fairly unexplained since advanced information about its respective features is still unsettled. In detail, neither the involved localized carrier states, nor their exact peak position, the shape, the band-width, and the absorption cross-section are known for the most of them. Furthermore, important knowledge to control the appearance of blue absorption by adjustment of, e.g., Fe-concentration, of the $\text{Fe}_{\text{Li}}^{2+/3+}$ -ratio, and/or by means of pulse peak energy and/or photon energies is missing in literature completely, so far.

The presence of transient absorption in the blue-green spectral range in LN was discovered in 2005 by Herth *et al.* in Fe-doped LN using single probe-laser lines [5] and – as a first attempt – has been attributed to the coupling of optically generated holes with the lattice in direct vicinity of V_{Li} lithium vacancies. The formation of O^- -hole polarons with strong coupling is in full accordance with the original expectations formulated by Schirmer *et al.* for nearly all polar oxide crystals [6]. Later on, investigations with continuous wave [7] and pulsed laser light [8,9], however, revealed several discrepancies to the hole polaron model. The results of Waasem *et al.* [7] demanded for the existence of further electronic states within the band-gap, being handled

as X -center of unknown microscopic nature. Quite recently, Messerschmidt *et al.* discussed excitonic states at the origin of long-lived transient blue absorption [9].

Self-trapped electron-hole-pairs at Nb-O-octahedra, commonly called *self-trapped excitons* (STEs) were widely investigated by Blasse *et al.* in nominally pure and doped LN by means of photoluminescence at temperatures below 100 K [10–12]. Similar luminescence phenomena were observed at room temperature using fs-NIR-pulse trains in Mg-doped LN [13] and have been assigned to the recombination of electron and hole polarons [14]. The goal of the work of Messerschmidt *et al.* [9] was to re-address charge-transport phenomena in LN by considering excitonic states as intermediate steps in addition. The authors succeeded to show, that the temperature dependence of transient absorption in LN crystals with Fe (and Mg) doping can be explained comprehensively by considering the presence of further (pinned) excitonic states, e.g., $\text{Fe}_{\text{Li}}^{2+} - \text{O}^- - \text{V}_{\text{Li}}$. It is noteworthy, that a main conclusion of this model approach is, that (pinned) STEs cause a pronounced long-lived blue absorption in Fe-doped LN (Fe:LN). We use the expression “pinned” in the context of this paper, if lattice defects or doping atoms hamper the movement and recombination of an STE in the regular lattice. In some cases, the pinned STE can be transformed into a self-trapped excitonic state in which at least one constituent is bound to the defect, e.g., the $\text{Fe}_{\text{Li}}^{2+} - \text{O}^- - \text{V}_{\text{Li}}$ STE.

In this paper, we address the open question about peak position, shape, bandwidth and absorption cross-section of the long-lived transient blue absorption under the assumption of self-trapped excitonic states as microscopic origin, i.e., following the general model approach of Ref. [9]. The study is performed using Fe-doped LN crystals according to previously reported pronounced transient blue absorption observed in these crystals. For the first time, ns-pump, supercontinuum-probe spectroscopy is applied in order to get a direct experimental access to the spectral shape of the optically induced excitonic blue absorption bands. At the same time, the determination of the temporal evolution of the absorption over a broad spectral range is mandatory for our analysis since it enables the spectral separation from further bound electronic states, such as, e.g., $\text{Nb}_{\text{Li}}^{4+/5+}$ or $\text{Fe}_{\text{Li}}^{2+/3+}$. These centers additionally show individual broad-band (≈ 1.0 eV) transient absorption [15] and, therefore, strongly overlap with the expected excitonic optical fingerprints. Quite recently, Schirmer *et al.* [16] and Sanson *et al.* [17] showed that the $\text{Fe}_{\text{Li}}^{2+/3+}$ center can be described in the small polaron model as well.

The experimental study is performed with LN crystals of various doping concentrations and $\text{Fe}_{\text{Li}}^{2+/3+}$ -ratio in order to account for three of the most common optical excitation paths in Fe:LN [18–20]:

- Iron D-band excitation, $E_{\text{abs}}^{\text{max}} = 2.6$ eV: A charge transfer from iron to the conduction band:
 $\text{Fe}_{\text{Li}}^{2+} \rightarrow \text{Nb}_{\text{Nb}}^{5+}$
- Iron C-band excitation, $E_{\text{abs}} > 3.1$ eV: A charge transfer from the valence band to iron:
 $\text{O}^{2-} \rightarrow \text{Fe}_{\text{Li}}^{3+}$
- Interband excitation, $E_{\text{abs}} > (3.8 - 4.1)$ eV: A charge transfer from the valence to the conduction band: $\text{O}^{2-} \rightarrow \text{Nb}_{\text{Nb}}^{5+}$

Accordingly, photon energies at 2.33 eV (532 nm) and 3.49 eV (355 nm) are used to pump the transients.

The individual spectra reveal that any spectral and temporal feature of the $(E - t)$ -plots can be modeled straightforwardly considering the additional presence of (pinned) excitonic states at iron. This knowledge is the anchor for the assignment of the excitonic absorption fingerprint from spectra obtained under rather different conditions. Finally, it is possible to analyze the main features (peak position, width) of the absorption band and, particularly to determine the respective absorption cross-section. For this purpose, the saturation of the $\text{Fe}_{\text{Li}}^{2+} - \text{O}^- - \text{V}_{\text{Li}}$ STE population is estimated by a pump intensity dependent measurement series. An instruction

for the control of the transient blue absorption can be clearly deduced for Fe-doped LN. At the same time, the reconstruction of the excitonic absorption feature with probably two individual absorption bands demands for further investigations, in particular of the electronic transition mechanisms of excitonic states in LN.

2. Experimental methods

Our experimental series is performed by means of ns-pump, supercontinuum-probe absorption spectroscopy. Electronic detection at room temperature using continuous-wave, single line probe lasers at 2.54 eV (488 nm) and 1.58 eV (785 nm) are additionally applied as described in previous studies (cf. e.g. [9]). The combined setup is schematically depicted in Fig. 1. The supercontinuum setup obtains an accessible time range of 100 ns up to 100 s and is capable to detect carrier-lattice phenomena with strong coupling, whereas formation dynamics and intermediate trapping states, such as the intermediate trapping of small, free $\text{Nb}_{\text{Nb}}^{4+}$ electron polarons, remain hidden.

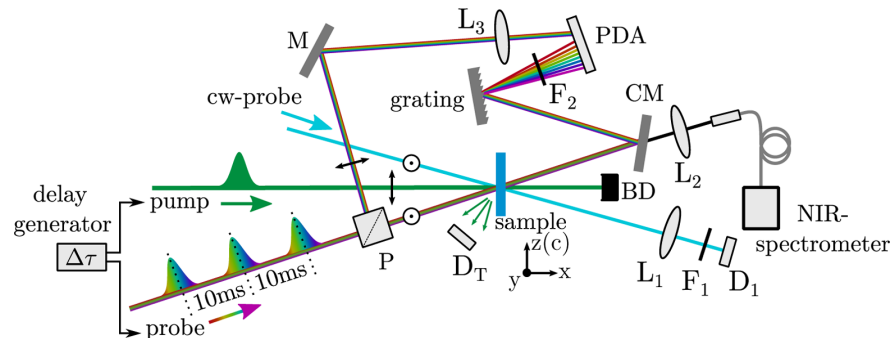


Fig. 1. Sketch of the ns-pump, supercontinuum-probe spectrometer applied in this study. The sample is pumped by a single pulse of a ns-pump pulse laser. Detection of the transient absorption is performed (i) using a diode (D_1) for the detection of the dynamic transmission change of a continuous wave probe laser transmitted through the sample (for a better visibility, only one cw-probe beam is shown) or (ii) by means of a supercontinuum. Here, the ns-pump pulse can be delayed for a certain time by a delay generator with respect to the supercontinuum probe pulse. The transmission change per wavelength is detected with two different spectrometers, one for the near-infrared part and one for the visible part of the supercontinuum pulse. $L_{1,2,3}$: lenses, $F_{1,2}$: optical filters, M: mirror, CM: cold mirror, P: polarizing beamsplitter cube, D_T : trigger diode for setup (i), BD: beam dump, PDA: photodiode array. The reader is referred to the text for further details.

A frequency-doubled and -tripled Nd:YAG pulse laser (Innolas Inc., *Spitlight*) and a broad-bandwidth light of a supercontinuum ns-pulse laser (LEUKOS, *STM-1-UV*) serve as pump ($\tau_{\text{FWHM}} = 8$ ns, extraordinarily polarized, $\lambda = 532$ nm (2.33 eV) or $\lambda = 355$ nm (3.49 eV), respectively) and probe sources ($\tau_{\text{FWHM}} < 1$ ns, unpolarized, $\lambda = (350 - 1800)$ nm $\equiv E = (3.54 - 0.69)$ eV, total average pulse energy of $35 \mu\text{J}$). The probe pulse is split by a broadband polarizing beamsplitter cube into two parts with perpendicular polarization states, i.e., ordinary (transmitted) and extraordinary (reflected) with respect to the crystal's c-axis. The latter is used as a reference signal whereas the ordinary polarized part is adjusted to an optimum overlap with the pump within the sample's volume. After the sample, the probe light is split in a near-infrared (NIR) and visible (VIS) spectral region by a longpass dichroic mirror ($\lambda_{\text{cut}} = 950$ nm). A fiber-spectrometer (OceanOptics *NIRQuest 512*) and a discrete photodiode

array (PDA, *Hamamatsu-S3902-512Q*, *TEC5*) are used simultaneously for the detection of the NIR and VIS signal fractions. A time resolution of up to 100 ns is achieved using an electronic delay of the pump. The time delay $\Delta\tau$ between pump and probe pulse is exponentially increased for $t = 100\text{ ns} - 10\text{ ms}$ so that the data points are equidistant on a logarithmic time axis. Data points for $t > 10\text{ ms}$ are obtained by measuring the subsequent pulses of the supercontinuum laser taking advantage of its repetition rate of 100 Hz. The signal-to-noise ratio is increased by signal averaging over 20 individual measurements. The transient absorption is calculated from the transmitted intensities via $\alpha_{\text{li}}(E, t) = -(1/d) \cdot \ln[I(E, t)/I(E, t \leq 0)]$, where $I(E, t)$ and $I(E, t \leq 0)$ are the transmitted probe light intensities after and before the pump pulse, respectively.

Our setup obeys minor limitations with respect to the spectral detection window, most of them being irrelevant for the purpose of our study: A lack of detection at 1.17 eV (1064 nm) and 2.33 eV (532 nm) due to a residual pump signal within the supercontinuum light and the SHG of the Nd:YAG pulse laser; one between 1.3 eV and 1.4 eV due to a low intensity of the supercontinuum laser and a weak sensitivity of the detectors; one above $\approx 3\text{ eV}$ due to a low intensity of the supercontinuum laser and a high intrinsic $\text{Fe}_{\text{Li}}^{2+}$ steady-state absorption of Fe-doped LN (particularly visible in the data of section 3.1).

Four LN crystals of the congruently melting composition [21,22] with different Fe dopant concentrations in the melt were used as depicted in Table 1. All samples were cut in a manner that the crystallographic c-axis is parallel to the polished surface and the y-axis along one edge. The $\text{Fe}_{\text{Li}}^{2+}$ -concentration ($c_{\text{Fe}_{\text{Li}}^{2+}}$) in the samples, obtained from MolTech GmbH (Fe:LN_1) and the University of Padova (Fe:LN_2, Fe:LN_3, and Fe:LN_4), was estimated by optical absorption measurements [23,24].

Table 1. Fe-doped LN crystals used in this study as obtained from MolTech GmbH (Fe:LN_1) and the University of Padova (Fe:LN_2, Fe:LN_3, and Fe:LN_4). The $\text{Fe}_{\text{Li}}^{2+}$ -concentrations were determined by optical absorption measurements [23,24]. d is denoting the thickness of the sample and $\alpha(2.6\text{ eV})$ the steady-state absorption at 2.6 eV.

Sample	d (mm)	$\alpha(2.6\text{ eV})$ (m^{-1})	$c_{\text{Fe}_{\text{Li}}}$ (mol %)	$c_{\text{Fe}_{\text{Li}}^{2+}}$ (10^{17} cm^{-3})	$c_{\text{Fe}_{\text{Li}}^{2+}}/c_{\text{Fe}_{\text{Li}}^{3+}}$
Fe:LN_1	2.0	468	0.185	10.4	0.029
Fe:LN_2	0.8	230	0.100	5.1	0.028
Fe:LN_3	2.0	45	0.020	1.0	0.027
Fe:LN_4	1.0	14	0.005	0.3	0.033

3. Experimental results

3.1. Excitation via the iron D-band

Figure 2 (left) shows the experimentally determined transient absorption for the case of optical excitation via the iron D-band, i.e., by means of a one-photon absorption process from $\text{Fe}_{\text{Li}}^{2+}$ to $\text{Nb}_{\text{Nb}}^{5+}$ (schematically sketched in Fig. 2 (right)).

The study is performed with sample Fe:LN_1 that obeys a high $\text{Fe}_{\text{Li}}^{2+}$ -concentration. Furthermore, we have chosen a photon energy of 2.33 eV for the pump pulse that is close to resonant excitation ($\text{Fe}_{\text{Li}}^{2+}$ peaks at 2.6 eV). The transients can be detected with sufficient signal-to-noise ratio in the spectral range of 0.7 eV to $\approx 3\text{ eV}$ and are exemplarily shown for a weak pulse peak intensity of $I_{\text{p}} \approx 30\text{ MW/cm}^2$. The $(E - t)$ -color plots are composed of two data sets that have been determined simultaneously with the VIS and NIR detector systems. The change of the light-induced absorption α_{li} is visualized by blue-yellow color coding as shown by the legend. Here, blue areas denote spectral regions with no change of the absorption upon the pump event, i.e., $\alpha_{\text{li}} \approx 0\text{ m}^{-1}$ and yellow regions mark noticeable changes with amplitudes up to $\alpha_{\text{li}} = 75\text{ m}^{-1}$. Black lines indicate a contour plot in steps of $\Delta\alpha_{\text{li}} = 15\text{ m}^{-1}$. Boxed white

areas refer to the regions where spectral detection is not possible due to the above mentioned experimental limitations.

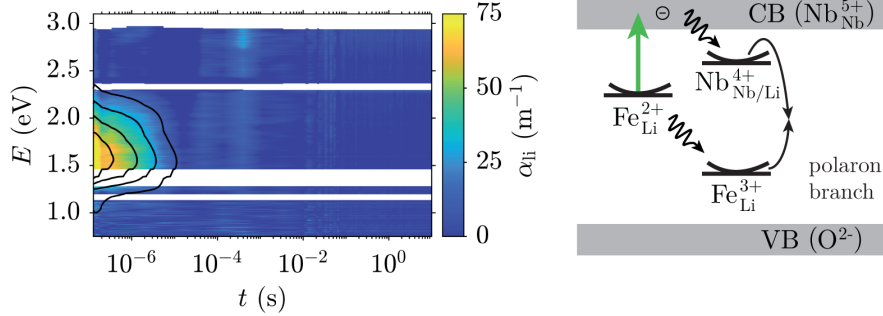


Fig. 2. Left: Transient absorption after an incident ns-pulse ($E = 2.33$ eV, $I_p \approx 30$ MW/cm²) in the sample Fe:LN_1. The color coding of the light-induced absorption change is given in the legend on the right. Black lines indicate contour lines for steps of $\Delta\alpha_{ii} = 15$ m⁻¹. Boxed white areas refer to the regions where spectral detection is not possible. **Right:** Excitation and recombination scheme for the case of optical excitation via the iron D-band. For details see text.

This plot shows that a single, broad-band light-induced absorption feature is induced in the near-infrared immediately after the incident pump pulse. In more detail, it appears in the spectral window of $E = (0.7 - 2.5)$ eV with a peak at about 1.6 eV and shows a noticeable signal on the timescale up to 10 μ s. Within the experimental errors no change of the absorption shape during the decay can be observed. Further analysis of the spectra measured at $t = 100$ ns reveals a maximum value of $\alpha_{ii}^{\max} \approx 75$ m⁻¹ with a full width at half maximum of ≈ 0.9 eV. In addition, the dynamic trace measured with a cw-laser at 1.58 eV can be reconstructed by means of a single stretched-exponential function [24] with a lifetime $\tau_{\text{KWW}}(1.58 \text{ eV}) = 10 \mu\text{s}$ and stretching factor $\beta(1.58 \text{ eV}) = 0.4$.

3.2. Excitation via the iron D-band + C-band

Figure 3 (left) shows the experimentally obtained spectrum using conditions that additionally account for optical excitation via the C-band, i.e., via one-photon absorption from the O²⁻ valence band to Fe³⁺_{Li} (cf. Fig. 3 (right)).

For this purpose, the sample Fe:LN_2 is used that was grown with a lower concentration of Fe in the melt. In addition, a photon energy of 3.49 eV of the pump pulse is used. Again, a moderate pump pulse intensity of $I_p \approx 27$ MW/cm² is chosen. The plot shows a considerable change of the transient absorption in comparison with the data of Fig. 2: a broad-band absorption feature appears immediately upon the incident pulse; it covers the total spectral range from the near-infrared to the blue, i.e., from 1.0 eV to 3.1 eV. A maximum of the light-induced absorption with values up to $\alpha_{ii}^{\max} \approx 350$ m⁻¹ is determined. Along the time axis, a disappearance of the NIR signal within a few microseconds is obvious ($\tau_{\text{KWW}}(1.58 \text{ eV}) = 2 \mu\text{s}$ and stretching factor $\beta(1.58 \text{ eV}) = 0.3$). In contrast, the long-lived blue absorption is nearly constant over tenth of milliseconds and develops a significant peak around 2.85 eV. It follows as well a single stretched-exponential function with $\tau_{\text{KWW}}(2.54 \text{ eV}) = 2$ s and $\beta(2.54 \text{ eV}) = 0.7$.

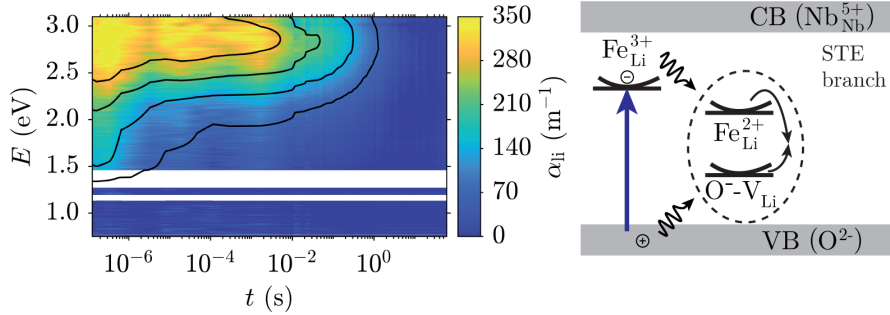


Fig. 3. Left: Transient absorption after an incident ns-pump pulse ($E = 3.49$ eV, $I_p \approx 27$ MW/cm²) in the sample Fe:LN_2. Color coding according to the legend on the right. The contour plot marks steps of $\Delta\alpha_{ij} = 70$ m⁻¹. Boxed white areas refer to the regions where spectral detection is not possible. **Right:** Excitation and recombination scheme for optical excitation via the iron C-band. For details see text.

3.3. Excitation via the iron D-band + C-band + TPA

Figure 4 (left) shows the results of our study using the sample Fe:LN_3, that features again a lower iron concentration in order to foster optical interband excitation, i.e., from the O²⁻ valence band to the Nb_{Nb}⁵⁺ conduction band (cf. Fig. 4 (right)).

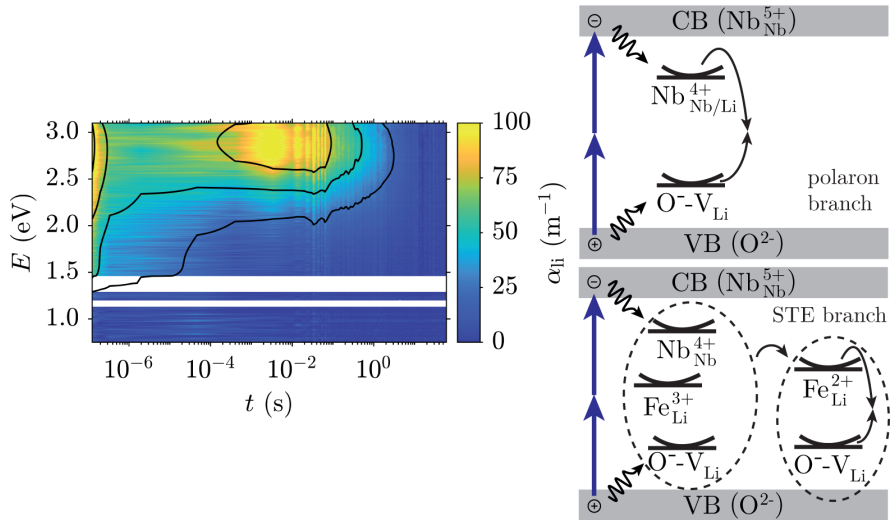


Fig. 4. Left: Supercontinuum transient absorption after 3.49 eV pulse exposure ($I_p \approx 12$ MW/cm²) in the sample Fe:LN_3 for the case of optical excitation via the D-band, C-Band and two-photon absorption. See legend on the right for color coding. The contour lines indicate steps of $\Delta\alpha_{ij} = 25$ m⁻¹. Boxed white areas refer to the regions where spectral detection is not possible. **Right:** Excitation and recombination scheme after excitation via a two-photon-absorption. For details see text.

Again, a photon energy of 3.49 eV is chosen for the pump pulse with a comparably weak pulse peak intensity of $I_p \approx 12 \text{ MW/cm}^2$. These experimental conditions result in the most complex dynamics of the transient absorption in Fe-doped LN: immediately upon the pump pulse, a broad-band absorption feature is detected with characteristics very similar to the situation in section 3.2, but with reduced maximum amplitude of the light-induced absorption with values up to $\alpha_{li}^{\text{max}} \approx 100 \text{ m}^{-1}$. It is very remarkable that this initial absorption shows a fast decay all over the blue and NIR spectral range with nearly the same temporal behavior. It results in a complete decay of the signal in the NIR with $\tau_{KWW}(1.58 \text{ eV}) = 10 \mu\text{s}$ and $\beta(1.58 \text{ eV}) = 0.3$. In contrast, a temporally constant transient absorption value ($\alpha_{li} > 0 \text{ m}^{-1}$) can be detected in the blue that remains over a duration of hundreds of microseconds. Subsequently, in the time range of milliseconds, the appearance of a delayed maximum with values up to $\alpha_{li}^{\text{max}} \approx 100 \text{ m}^{-1}$ is detected. Similar to the findings in section 3.2, it peaks around 2.85 eV and the long decay can be described with the parameters $\tau_{KWW}(2.54 \text{ eV}) = 2 \text{ s}$ and $\beta(2.54 \text{ eV}) = 0.6$.

3.4. Absorption spectra and saturation of the long-lived blue absorption

Figure 5 shows the direct comparison of the long-lived transient blue absorption features as obtained from a more detailed analysis of the spectra depicted in Figs. 3 and 4.

The spectra were deduced by normalizing the data points at every delay position to the respective spectral maximum of the light-induced absorption and subsequently averaging the data set over the time interval from $t > 1 \cdot 10^{-3} \text{ s}$ to 10 s. Obviously, both spectra reveal a comparable shape with respect to the peak position of $E_{\text{peak}} = (2.85 \pm 0.05) \text{ eV}$ and full width at half maximum of $\text{FWHM} = (1.00 \pm 0.25) \text{ eV}$.

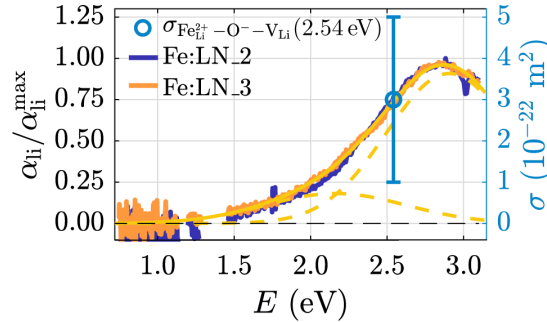


Fig. 5. Spectra of the long-lived blue absorption as deduced from the data in Fig. 3 and Fig. 4 by normalizing the data points at every delay position to the spectral maximum of the light-induced absorption and averaging the data set over the time interval from $t > 1 \cdot 10^{-3} \text{ s}$ to 10 s. The yellow line represents a converging result of fitting Eq. (1) to the data. The dashed yellow lines refer to the individual Gaussians as given in Table 2. The blue data point is an experimentally determined value of the absorption cross-section at 2.54 eV and serves as scaling factor for the y-axis on the right.

Table 2. Parameters obtained from fitting the sum of two Gaussian functions (Eq. (1)) to the experimental data set for the case of two distinct absorption bands as sketched in Fig. 5. The fitting procedure reveals two solutions with a root mean square error of $\text{RMSE} = 0.0387$.

fit	a_1	a_2	$b_1 \text{ (eV)}$	$b_2 \text{ (eV)}$	$c_1 \text{ (eV)}$	$c_2 \text{ (eV)}$
1	0.91 ± 0.18	0.18 ± 0.17	2.91 ± 0.07	2.16 ± 0.50	0.41 ± 0.06	0.46 ± 0.17
2	0.37 ± 0.08	0.60 ± 0.40	2.88 ± 0.15	2.88 ± 0.34	0.31 ± 0.04	0.64 ± 0.03

It is possible to reconstruct the absorption shape by the sum of two Gaussians via:

$$\frac{\alpha_{ii}(E)}{\alpha_{ii}^{\max}} = a_1 \cdot \exp\left[-\frac{(E-b_1)^2}{2c_1^2}\right] + a_2 \cdot \exp\left[-\frac{(E-b_2)^2}{2c_2^2}\right], \quad (1)$$

where $a_{1,2}$, $b_{1,2}$ and $c_{1,2}$ represent the amplitude, peak position and standard deviation of the individual Gaussian functions. As a result of the fitting procedure, two converging solutions are found. One, with two distinct absorption bands, is shown in Fig. 5. The associated fitting parameters are given in Table 2. A second converging solution of the fitting procedure results in two absorption bands peaking at the same photon energy of $E_{\text{peak}} \approx 2.88$ eV, but with rather different amplitudes and FWHM values.

In order to check whether the long-lived blue absorption shows a saturation value at high intensities, we have performed appropriate measurements using our standard pump-probe experiment due to the higher signal-to-noise ratio and signal stability along with the use of a 2.54 eV continuous-wave laser system. Figure 6 shows the maximum amplitude $\alpha_{ii}^{\max}(2.54 \text{ eV})$ measured for various pump intensities at $E_p = 3.49$ eV in the sample Fe:LN_4 which contains the lowest iron concentration in this study. The maximum amplitude follows at low pump intensities a quadratic behavior with increasing intensities. However, above $I_p \approx 50 \text{ MW/cm}^2$ the amplitudes start to saturate. The data can be described with the following function:

$$\alpha_{ii}^{\max}(E, I) = \alpha_{ii}^{\max}(E, I \rightarrow \infty) \cdot \left[1 - \exp\left(-\frac{I^2}{I_\alpha^2}\right)\right], \quad (2)$$

where $\alpha_{ii}^{\max}(E, I \rightarrow \infty)$ is the saturation value and I_α is the characteristic intensity. A fit of Eq. (2) to the data reveals $\alpha_{ii}^{\max}(2.54 \text{ eV}, I \rightarrow \infty) = (276 \pm 25) \text{ m}^{-1}$ and $I_\alpha = (50 \pm 5) \text{ MW/cm}^2$.

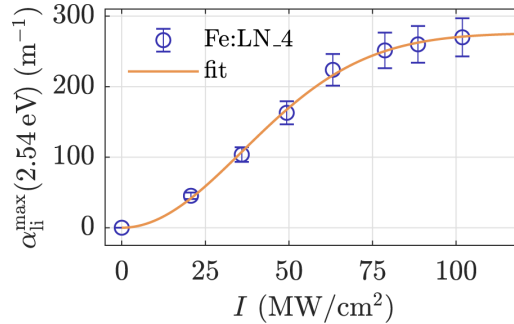


Fig. 6. Maximum amplitude of the long-lived blue absorption probed at 2.54 eV after pulse exposure at 3.49 eV for various intensities in the sample Fe:LN_4. The orange line is a fit of Eq. (2) to the data.

4. Discussion

Our experimental study reveals that ns-pump, supercontinuum-probe spectroscopy is successfully applied for the detection of transient absorption in Fe-doped lithium niobate. New insight to the temporal and, particularly, spectral evolution of pulse-induced absorption phenomena is obtained in the time interval from nanoseconds up to a few seconds and (nearly) without a gap from the blue to the near infrared spectral range. At a glance, the obtained $(E-t)$ -plots demonstrate (i) the variety of transient absorption phenomena that appear in Fe-doped LN upon a single laser pulse, (ii) their complexity with respect to the spectral overlap of different absorption

features as well as to a time-delayed build-up and (iii) their dependence on the experimental boundary conditions. The signal-to-noise-ratio is sufficient to resolve intensity changes in the order of $\delta I/I_0 \approx 0.5\%$. In this respect, the experimental detection by means of single-line continuous-wave laser beams remains as a mandatory tool for the detection of very weak signals and/or for the detailed inspection of the temporal shapes of the absorption features. The presented experimental combination brings together the advantage of both techniques and enables the comprehensive analysis of transient absorption in LN without any constraint.

In what follows, we will first discuss the individual data sets in more detail according to the state-of-the-art knowledge of small polarons with strong coupling and considering the model of (pinned) excitonic states, i.e., according to the previously reported model approach by Messerschmidt *et al.* [9]. Then, we focus on the absorption features of the $\text{Fe}_{\text{Li}}^{2+} - \text{O}^- - \text{V}_{\text{Li}}$ excitonic state and will deduce the respective absorption cross-section, peak position and bandwidth. It should be noted that we neglect the inclusion of the intrinsic luminescent $\text{Nb}_{\text{Nb}}^{4+} - \text{O}^-$ STE in all excitation/recombination schemes. It is because such centers are expected to appear predominantly in stoichiometric or Mg-doped LN in a time range much shorter than the used pulse duration, i.e., not accessible with our experimental setup (at room temperature) [9,25].

4.1. Excitation via the iron D-band

The experimental conditions resulting in the data presented in Fig. 2 (left) were prepared in a manner that a one-photon excitation via the iron D-band is highly preferred (high $\text{Fe}_{\text{Li}}^{2+}$ -concentration, pump wavelength near the maximum of the $\text{Fe}_{\text{Li}}^{2+}$ absorption band). We therefore analyze the transients by considering optical excitation/subsequent relaxation from/back to $\text{Fe}_{\text{Li}}^{2+/3+}$ and the interim formation of small $\text{Nb}_{\text{Li/Nb}}^{4+}$ polarons (c.f. Fig. 2 (right)). In particular, we expect that the pulse-induced absorption over the entire spectral range results from the interplay of a light-induced transparency due to less $\text{Fe}_{\text{Li}}^{2+}$ (ground-state bleach) and an increased absorption due to the formation of small bound polarons, i.e., $\alpha_{\text{li}}(E) = \Delta N_{\text{Nb}_{\text{Li}}^{4+}} \cdot \sigma_{\text{Nb}_{\text{Li}}^{4+}}(E) + \Delta N_{\text{Fe}_{\text{Li}}^{2+}} \cdot \sigma_{\text{Fe}_{\text{Li}}^{2+}}(E)$. Here, $\Delta N_{\text{Nb}_{\text{Li}}^{4+}} = -\Delta N_{\text{Fe}_{\text{Li}}^{2+}}$ where ΔN is the change of concentration induced by the pump pulse. Considering the dispersion features of the two absorption species with well separated peak positions (1.6 eV and 2.6 eV) [15], a pronounced NIR absorption change shall remain that is mainly attributed to $\text{Nb}_{\text{Li}}^{4+}$. At the same time, no changes are expected for the blue-green spectral range since the absorption cross sections of $\text{Nb}_{\text{Li}}^{4+}$ and $\text{Fe}_{\text{Li}}^{2+}$ strongly overlap in this region and are nearly identical: $\sigma_{\text{Fe}_{\text{Li}}^{2+}}(\text{blue}) \approx \sigma_{\text{Nb}_{\text{Li}}^{4+}}(\text{blue})$ [15]. Our experimental findings in Fig. 2 are in full agreement with both expectations: a broad-band NIR absorption is clearly visible with nearly no absorption change in the blue-green spectral range (within the noise of our experiment). Moreover, three significant polaron fingerprints can be verified, particularly considering $\text{Nb}_{\text{Li}}^{4+}$: a lifetime in the sub-ms-time range, a NIR absorption feature with a peak at about 1.6 eV and a stretched-exponential decay behavior with a β -value below 1/2. We need to note, that in this discussion, we neglect the interim formation of $\text{Nb}_{\text{Nb}}^{4+}$ free polarons due to experimental constraints: the free polaron lifetime is much shorter than the temporal resolution of our experiment [8]. A transient signal at the the peak maximum of small free polarons of about 1.0 eV [15] was therefore not observed. All these findings and interpretations are in full agreement with the state-of-the-art knowledge of the interaction of continuous-wave and pulsed laser light with Fe-doped LN at moderate average power [24,26].

4.2. Excitation via the iron D-band + C-band

The second measurement was performed with an iron-doped LN sample containing a lower Fe-concentration and with a pump wavelength in the UV. This fosters the optical excitation via the iron C-band, though an excitation via the D-band cannot be excluded. We additionally need to consider that the cross-sections of these two excitation paths are very similar at 355 nm [27],

i.e., a contribution of both paths to the transient spectrum is to be expected. In this sense, and in direct comparison with the discussion of the previous section, it is likely to assume that the observed NIR absorption feature with fast decay in the spectra of Fig. 3 originates from the mechanisms associated with the D-band excitation (see section 4.1). All deduced experimental features (peak position, lifetime, stretching factor) support this assumption. Accordingly, the UV-induced long-lived blue absorption in Fig. 3 is assigned to the second excitation path via the iron C-band. To the best of our knowledge, the latter has not been investigated in the context of either small polarons or STEs in lithium niobate, so far. At a first glance, a relation to the formation of small $O^- - V_{Li}$ hole and Fe_{Li}^{2+} polarons may be assumed considering the charge-transfer from O^{2-} to Fe_{Li}^{3+} [18] (c.f. Fig. 3 (right)). However, in this case, the blue absorption must feature a broad-band absorption centered in the range of 2.5 – 2.6 eV [6,15], that does not correspond with the experimentally determined peak position of about 2.85 eV in our spectra (see Fig. 5 and discussion below). An alternative microscopic approach is to consider $Fe_{Li}^{2+} - O^- - V_{Li}$ STEs as proposed by Messerschmidt *et al.* [9]. Such states are reported to form after pinning and subsequent transformation of an intrinsic STE at an iron center within a few hundred microseconds. They show absorption in the blue-green spectral range and their decay dynamics feature a stretching factor $\beta > 2/3$. According to the characteristics of the induced blue absorption deduced from the data in Fig. 2 (absorption feature with a peak at about 2.85 eV, an increased stretching factor of $\beta \approx 0.7$), it is reasonable to assume the presence of such states in our case, as well. A remarkable consequence of this approach is that the direct STE formation via the C-band is discovered for the first time. This finding is of particular importance of applications with doped LN and ultraviolet laser pulses, e.g., UV photorefractive.

4.3. Excitation via the iron D-band + C-band + TPA

The third measurement in this study was performed with a sample containing a lower Fe_{Li}^{2+} - and Fe_{Li}^{3+} -concentration and, thus, also obeys the one-photon excitation and the subsequent recombination paths via the iron C- and D-band as discussed in the two previous sections 4.1 and 4.2. In addition, the low Fe-concentration increases the probability for excitation via two-photon absorption (TPA). It is because the negligible fundamental absorption conserves the peak intensity of the incident laser pulse. The influence of the electron-hole-pairs generated via TPA on the decay dynamics can be deduced by comparing the results in the two previous sections 4.1 and 4.2 with the data in section 3.3 (c.f. Fig. 4). The main differences are (i) an additional fast decay and (ii) a delayed increase in the blue spectral range. Both phenomena can be explained as follows: the generation of electron-hole pairs in the LN-host lattice results in the formation of $O^- - V_{Li}$ hole and Nb_{Li}^{4+} bound polarons as well as STEs which can be pinned next to Fe_{Li}^{3+} (c.f. Fig. 4 (right)). The formed polarons/STEs contribute to the transient spectra with absorption features in the blue and near-infrared spectral range. The decay of the initial transient signals in the blue and NIR spectral range is a characteristic fingerprint for the recombination of hole polarons with bound polarons known from undoped lithium niobate samples [3,15]. However, in contrast to an undoped sample, the initial temporal decay in the blue spectral range is superimposed by the transformation of pinned STEs at Fe_{Li}^{3+} into $Fe_{Li}^{2+} - O^- - V_{Li}$ inducing a strong blue absorption in the time range of milliseconds [9]. The observed complex behavior in the blue spectral range then is due to the different decay dynamics of the hole/bound polaron recombination on the one hand and the transformation of pinned STEs on the other hand.

4.4. Determination of the shape and absorption cross-section of the long-lived blue absorption

The discussion of the previous sections points to a dominant role of $Fe_{Li}^{2+} - O^- - V_{Li}$ STEs at the origin of the long-lived blue absorption in Fe-doped LN which is in accordance with Ref. [9]. Following this microscopic approach, the spectra of Fig. 3 and Fig. 4 will both be related with

this excitonic state. Figure 5 compares the spectral shapes of the long-lived blue absorption as obtained from a further analysis of these data sets. Obviously, both spectra are characterized by a comparable shape, peak position and bandwidth and are nearly indistinguishable from each other. This result is very remarkable since the data sets were obtained in two completely different Fe-doped LN crystals and by using different pulse intensities for excitation. Moreover, it supports the finding that $\text{Fe}_{\text{Li}}^{2+} - \text{O}^- - \text{V}_{\text{Li}}$ STEs can be formed directly after the pump pulse via the iron C-band.

Let us now further analyze the absorption spectrum depicted in Fig. 5 in the microscopic model of $\text{Fe}_{\text{Li}}^{2+} - \text{O}^- - \text{V}_{\text{Li}}$ STEs. First, we discuss the shape of the STE absorption feature. Figure 5 shows that the pulse-induced absorption appears with a large amplitude over the entire VIS-NIR spectral region that is experimentally accessible with our setup. It can be expected that the band extends even far into the ultraviolet region and, that it overlaps with the interband absorption (starting at about 3.8 eV). Fitting the spectrum in the accessible region reveals that at least the sum of two Gaussian functions (c.f. Eq. (1)) with six free fitting parameters is required for its description. Exemplarily, one of the converging solutions is depicted in Fig. 5 with different peak positions (2.2 eV and 2.8 eV, respectively) but comparable FWHMs of the constituents (c.f. Table 2). We note that it is alternatively possible to perform the fitting procedure with two Gaussians at the same peak position (of about 2.9 eV), but with different FWHM values.

Taking these findings into account, we refer to the state-of-the-art knowledge of STE absorption bands and find that they typically resemble the interplay of at least two spectrally separated single bands in a first approximation [28–30]: a straightforward explanation is that the two bands originate from an optical excitation of both the electron and the hole to higher states, respectively. Or, the two bands refer to the photo-ionization process of STEs. Against this background, it is reasonable to expect two absorption bands for STEs in LN as well, one associated with the electron excitation from $\text{Fe}_{\text{Li}}^{2+}$ and the other one from the $\text{O}^- - \text{V}_{\text{Li}}$ -center. Peak position, bandwidth and the relative fraction of the total absorption amplitude (c.f. Table 2) then reflect the individual absorption features and absorption cross-sections of the two constituents involved. In particular, the effective absorption coefficient of the STE then is given by $\alpha_{\text{eff}}(E) = \alpha_1(E) + \alpha_2(E)$ in this case.

Second, we intend to estimate the effective absorption cross-section of the $\text{Fe}_{\text{Li}}^{2+} - \text{O}^- - \text{V}_{\text{Li}}$ STE. For this purpose, following the discussion of the previous paragraph, it is assumed that the absorption feature originates from a single absorption center of number density N , i.e., $\alpha_{\text{eff}}(E) = \sigma_{\text{eff}}(E) \cdot N$. In our case, the number density N can be determined experimentally by intensity dependent measurements of $\alpha_{\text{ii}}(I)$ as depicted in Fig. 6. It is because $N(I)$ saturates due to a limited $\text{Fe}_{\text{Li}}^{3+}$ -concentration such that $\alpha_{\text{ii}}(I)$ saturates, too. The experimentally determined saturation value $\alpha_{\text{ii}}^{\text{max}}(E, I \rightarrow \infty)$ then enables the calculation of the effective cross-section via $\sigma_{\text{eff}}(E) = \alpha_{\text{ii}}^{\text{max}}(E, I \rightarrow \infty) / c_{\text{Fe}_{\text{Li}}^{3+}}$. This study has been performed at a minimum total iron concentration to (i) ensure that a saturation value can be achieved with our experimental conditions and (ii) enable the utilization of low pump intensities to avoid laser induced damages. With the data deduced from Fig. 6 we obtain $\sigma_{\text{eff}}(2.54 \text{ eV}) = (3 \pm 2) \cdot 10^{-22} \text{ m}^2$. This value serves for scaling the right y-axis in Fig. 5 which leads to a maximum effective cross-section of $\sigma_{\text{eff}}^{\text{max}}(2.85 \text{ eV}) = (4 \pm 2) \cdot 10^{-22} \text{ m}^2$. The large error of these values is a combination of both, the precision of our measurement and the determination of the iron concentration. We would also like to mention that the estimated values are only a lower bound because the calculation is based on the assumption that all $\text{Fe}_{\text{Li}}^{3+}$ -centers are occupied in the saturation state. If this assumption is inapplicable, the number density of STEs is reduced which will result in a larger value of the absorption cross-section. In comparison to small polarons in lithium niobate [15], the absorption cross-section of the STE is in the same order of magnitude. Assuming that (pinned) STEs formed under similar conditions, e.g., in Mg-doped LN, exhibit similar absorption bands and

cross-sections, they have to play an important role in the blue absorption and might be responsible for a damping of frequency conversion and laser induced damages in this spectral range.

5. Conclusion

This study reveals the striking impact of ns-pump, supercontinuum-probe spectroscopy for the microscopic understanding of strongly localized electronic states in oxide crystals with lithium niobate as an example. The spectra allow to distinguish the temporal and spectral action of individual optically generated species under rather different experimental conditions and their formation/transport/recombination/relaxation description within a quite complex band model scheme. As a result it is possible to discover new properties of the interaction of light pulses with a strong polar crystal, e.g., the possibility to optically generate $\text{Fe}_{\text{Li}}^{2+} - \text{O}^- - \text{V}_{\text{Li}}$ STEs directly by a charge transfer via the iron C-band. Furthermore, the STE absorption cross-section obeys similar values as reported for small polarons. Another impressive result of this study is that the combination of transient spectroscopy and the polaron/exciton model in LN enables the precise prediction of the complex dynamics of transient absorption over a large spectral and temporal range. At the same time, it supports the validity of the model of (pinned) STEs for lithium niobate, which have been disregarded in the mechanisms of light-induced transport, so far. Our findings are of particular importance for the field of photorefractive since the formation of STEs will not result in the optically induced separation of charges that is mandatory for the photorefractive effect. The possibility to solely generate excitonic states by means of optical adjustment of pulse parameters (photon energy, pulse peak energy) and/or material adjustment ($\text{Fe}^{2+/3+}$ -ratio) enables, e.g., the efficient suppression of optical damage in LN-based frequency converters. In the same manner, it is possible to determine temporal regimes that allow for photorefractive recording at elevated efficiencies, such as, e.g., the sub-millisecond time range for recording with a single, intense laser pulse.

Funding

Deutscher Akademischer Austauschdienst (DAAD) (57390412); Deutsche Forschungsgemeinschaft (DFG) (IM37/11-1, INST 190/165-1 FUGG); Osnabrueck University (Open Access Fund).

Acknowledgements

The authors are indebted to thank Marco Bazzan and coworkers for crystals and crystal preparation as well as Christoph Merschjann for fruitful discussion.

References

1. R. Batchko, G. Miller, A. Alexandrovski, M. Fejer, and R. Byer, "Limitations of high-power visible wavelength periodically poled lithium niobate devices due to green-induced infrared absorption and thermal lensing," *Tech. Dig. Summ. Pap. Present. at Conf. on Lasers Electro-Optics. Conf. Ed. 1998 Tech. Dig. Series, Vol. 6 (IEEE Cat. No.98CH36178)* (1998).
2. H. M. Yochum, K. B. Üçer, R. T. Williams, L. Grigorjeva, D. Millers, and G. Corradi, "Subpicosecond Laser Spectroscopy of Blue-Light-Induced Absorption in KNbO_3 and LiNbO_3 ," *Defects Surface-Induced Eff. Adv. Perovskites* pp. 125–138 (2000).
3. M. Imlau, H. Badorreck, and C. Merschjann, "Optical nonlinearities of small polarons in lithium niobate," *Appl. Phys. Rev.* **2**(4), 040606 (2015).
4. Y. Furukawa, K. Kitamura, A. Alexandrovski, R. K. Route, M. M. Fejer, and G. Foulon, "Green-induced infrared absorption in MgO doped LiNbO_3 ," *Appl. Phys. Lett.* **78**(14), 1970–1972 (2001).
5. P. Herth, T. Granzow, D. Schaniel, T. Woike, M. Imlau, and E. Krätzig, "Evidence for Light-Induced Hole Polarons in LiNbO_3 ," *Phys. Rev. Lett.* **95**(6), 067404 (2005).
6. O. F. Schirmer, " O^- bound small polarons in oxide materials," *J. Phys.: Condens. Matter* **18**(43), R667–R704 (2006).
7. N. Waasem, A. Markosyan, M. M. Fejer, and K. Buse, "Green-induced blue absorption in MgO-doped lithium niobate crystals," *Opt. Lett.* **38**(16), 2953 (2013).

8. D. Conradi, C. Merschjann, B. Schoke, M. Imlau, G. Corradi, and K. Polgár, "Influence of Mg doping on the behaviour of polaronic light-induced absorption in LiNbO₃," *Phys. Status Solidi RRL* **2**(6), 284–286 (2008).
9. S. Messerschmidt, A. Krampf, F. Freytag, M. Imlau, L. Vittadello, M. Bazzan, and G. Corradi, "The role of self-trapped excitons in polaronic recombination processes in lithium niobate," *J. Phys.: Condens. Matter* **31**(6), 065701 (2019).
10. D. M. Krol, G. Blasse, and R. C. Powell, "The influence of the Li/Nb ratio on the luminescence properties of LiNbO₃," *J. Chem. Phys.* **73**(1), 163–166 (1980).
11. M. Wiegel, M. Emond, E. Stobbe, and G. Blasse, "Luminescence of alkali tantalates and niobates," *J. Phys. Chem. Solids* **55**(8), 773–778 (1994).
12. M. Wiegel, G. Blasse, A. Navrotsky, A. Mehta, N. Kumada, and N. Kinomura, "Luminescence of the Ilmenite Phase of LiNbO₃," *J. Solid State Chem.* **109**(2), 413–415 (1994).
13. P. Reichenbach, T. Kämpfe, A. Haußmann, A. Thiessen, T. Woike, R. Steudtner, L. Kocsor, Z. Szaller, L. Kovács, and L. Eng, "Polaron-Mediated Luminescence in Lithium Niobate and Lithium Tantalate and Its Domain Contrast," *Crystals* **8**(5), 214 (2018).
14. T. Kämpfe, A. Haußmann, L. M. Eng, P. Reichenbach, A. Thiessen, T. Woike, and R. Steudtner, "Time-resolved photoluminescence spectroscopy of Nb_{Nb}⁴⁺ and O⁻ polarons in LiNbO₃ single crystals," *Phys. Rev. B* **93**(17), 174116 (2016).
15. C. Merschjann, B. Schoke, D. Conradi, M. Imlau, G. Corradi, and K. Polgár, "Absorption cross sections and number densities of electron and hole polarons in congruently melting LiNbO₃," *J. Phys.: Condens. Matter* **21**(1), 015906 (2009).
16. O. F. Schirmer, M. Imlau, and C. Merschjann, "Bulk photovoltaic effect of LiNbO₃:Fe and its small-polaron-based microscopic interpretation," *Phys. Rev. B* **83**(16), 165106 (2011).
17. A. Sanson, A. Zaltron, N. Argiolas, C. Sada, M. Bazzan, W. G. Schmidt, and S. Sanna, "Polaronic deformation at the Fe^{2+/3+} impurity site in Fe:LiNbO₃ crystals," *Phys. Rev. B* **91**(9), 094109 (2015).
18. M. G. Clark, F. J. DiSalvo, A. M. Glass, and G. E. Peterson, "Electronic structure and optical index damage of iron-doped lithium niobate," *J. Chem. Phys.* **59**(12), 6209–6219 (1973).
19. B. Dischler, J. Herrington, A. Räufer, and H. Kurz, "Correlation of the photorefractive sensitivity in doped LiNbO₃ with chemically induced changes in the optical absorption spectra," *Solid State Commun.* **14**(11), 1233–1236 (1974).
20. L. Kovács, G. Ruschhaupt, K. Polgár, G. Corradi, and M. Wöhlecke, "Composition dependence of the ultraviolet absorption edge in lithium niobate," *Appl. Phys. Lett.* **70**(21), 2801–2803 (1997).
21. J. R. Carruthers, G. E. Peterson, M. Grasso, and P. M. Bridenbaugh, "Nonstoichiometry and Crystal Growth of Lithium Niobate," *J. Appl. Phys.* **42**(5), 1846–1851 (1971).
22. T. Volk and M. Wöhlecke, *Lithium Niobate: Defects, Photorefraction and Ferroelectric Switching*, Springer Series in Materials Science (Springer Berlin Heidelberg, 2008).
23. H. Kurz, E. Krätzig, W. Keune, H. Engelmann, U. Gonser, B. Dischler, and A. Räufer, "Photorefractive centers in LiNbO₃, studied by optical-, Mössbauer- and EPR-methods," *Appl. Phys.* **12**(4), 355–368 (1977).
24. D. Berben, K. Buse, S. Wevering, P. Herth, M. Imlau, and T. Woike, "Lifetime of small polarons in iron-doped lithium-niobate crystals," *J. Appl. Phys.* **87**(3), 1034–1041 (2000).
25. F. Klöse, M. Wöhlecke, and S. Kapphan, "UV-excited luminescence of LiNbO₃ and LiNbO₃:Mg," *Ferroelectrics* **92**(1), 181–187 (1989).
26. P. Herth, D. Schaniel, T. Woike, T. Granzow, M. Imlau, and E. Krätzig, "Polarons generated by laser pulses in doped LiNbO₃," *Phys. Rev. B* **71**(12), 125128 (2005).
27. M. V. Ciampolillo, A. Zaltron, M. Bazzan, N. Argiolas, and C. Sada, "Quantification of Iron (Fe) in Lithium Niobate by Optical Absorption," *Appl. Spectrosc.* **65**(2), 216–220 (2011).
28. R. T. Williams and M. N. Kabler, "Excited-state absorption spectroscopy of self-trapped excitons in alkali halides," *Phys. Rev. B* **9**(4), 1897–1907 (1974).
29. R. Williams and K. Song, "The self-trapped exciton," *J. Phys. Chem. Solids* **51**(7), 679–716 (1990).
30. P. Li, S. Gridin, K. B. Ucer, R. T. Williams, and P. R. Menge, "Picosecond absorption spectroscopy of self-trapped excitons and transient Ce states in LaBr₃ and LaBr₃:Ce," *Phys. Rev. B* **97**(14), 144303 (2018).

Danksagung

Zunächst geht an erster Stelle mein Dank an Herrn Prof. Dr. Mirco Imlau für die Aufnahme in die Forschergruppe *Ultrakurzzeitphysik* sowie für die ausgezeichnete Betreuung und den konstruktiven Diskussionen während der gesamten Studien- und Promotionszeit.

Weiterhin bedanke ich mich bei Herrn Prof. Dr. Simone Sanna von der Universität Gießen für die Begutachtung dieser Arbeit.

Ein großer Dank geht auch an alle Autoren, mit denen im Rahmen dieser Arbeit gemeinsame wissenschaftliche Publikationen entstanden sind, für die sehr gute Zusammenarbeit. Besonders bedanken möchte ich mich bei Herrn Msc. Andreas Krampf, Herrn Msc. Björn Bourdon, Herrn Dr. Christian Kijatkin, Herrn Dr. Gabór Corradi, Frau Dr. Laura Vittadello und Herrn Dr. Marco Bazzan, die mich immer bei offenen Fragestellungen sowie Problemen mit langen Diskussionen und neuen Ideen unterstützt haben.

Den Mitarbeitern der elektronischen und feinmechanischen Werkstatt danke ich für die Anfertigung und Reparatur verschiedenster Bauteile ohne die viele Messungen nicht möglich gewesen wären.

Mein Dank gilt außerdem allen weiteren aktuellen und ehemaligen Arbeitskollegen für das gute Arbeitsklima und die allgemeine Hilfsbereitschaft.

Abschließend möchte ich mich ganz herzlich bei meiner Familie und meiner Frau Katrin bedanken, die mich alle während meines ganzen Studiums und der Promotion begleitet und unterstützt haben.

Erklärung über die Eigenständigkeit der erbrachten wissenschaftlichen Leistung

Ich erkläre hiermit, dass ich die vorliegende Arbeit ohne unzulässige Hilfe Dritter und ohne Benutzung anderer als der angegebenen Hilfsmittel angefertigt habe. Die aus anderen Quellen direkt oder indirekt übernommenen Daten und Konzepte sind unter Angaben der Quelle gekennzeichnet.

Weitere Personen waren an der inhaltlichen materiellen Erstellung der vorliegenden Arbeit nicht beteiligt. Insbesondere habe ich hierfür nicht die entgeltliche Hilfe von Vermittlungs- bzw. Beratungsdiensten (Promotionsberater oder andere Personen) in Anspruch genommen. Niemand hat von mir unmittelbar oder mittelbar geldwerte Leistungen für Arbeiten erhalten, die im Zusammenhang mit dem Inhalt der vorgelegten Dissertation stehen. Die Arbeit wurde bisher weder im In- noch im Ausland in gleicher oder ähnlicher Form einer anderen Prüfungsbehörde vorgelegt.

Osnabrück, den 14. Mai 2019